Capillary Force Actuation for Achieving Large Deflections of an Elastomeric Membrane at Low Voltage

---

A Thesis

Presented to

the faculty of the School of Engineering and Applied Science

University of Virginia

---

in partial fulfillment

of the requirements for the degree

Master of Science

by

Christina Alexandra Barth

August

2016

APPROVAL SHEET

The thesis

is submitted in partial fulfillment of the requirements

for the degree of

Master of Science

Christina Alexandra Barth

AUTHOR

Dr. Carl Knospe

Advisor

Dr. Baoxing Xu

Dr. Eric Loth

Dr. Michael Reed

Dr. Nathan Swami

Accepted for the School of Engineering and Applied Science:

Craig H. Benson, Dean, School of Engineering and Applied Science

August

2016

Abstract

Elastomeric materials offer many benefits to MEMS (Micro Electro Mechanical Systems). These benefits include smaller device footprints, greater range of motion, and lower required actuation forces. However, a complementary actuation technology is needed, to implement the capabilities of elastomeric components. Capillary forces are a novel and promising mechanism to produce motion in the flexible components of micro devices – such as elastomeric membranes [1].

Capillary Force Actuators (CFAs) are a new type of MEMS microactuator. They are capable of delivering significantly greater forces and larger actuation strokes than current technology. In the Capillary Force Actuated Membrane, CFAM, a conducting liquid bridge extends between two electrodes, each covered by a thin dielectric layer to form an electrowetting substrate. When voltage is applied, the contact angle of the liquid changes, a process known as Electrowetting on Dielectric (EWOD). The change in contact angle results in a change in the curvature of the liquid bridge's profile. From Laplace's equation for the pressure change across an interface, this change in curvature results in a decrease in the capillary pressure of the liquid. If the liquid bridge is in contact with an elastomeric membrane the change in pressure will result in deflection of the membrane. The amount of deflection achievable thus depends on the decrease in contact angle obtained via electrowetting and the surface tension of the liquid.

This thesis focuses on the design, fabrication, and experimental demonstration of a new actuation method for the displacement of elastomeric membranes. Two CFAM prototypes are designed after a study of CFAM physics, with the development of a predictive model for membrane displacement. The two prototypes are representative of two common types of electrowetting configurations. We utilize an optimized non-photolithography microfabrication process to produce the prototypes. A side view of the capillary bridge profile is implemented - via florescent lighting – to the existing displacement test platforms. Thus, we are able to characterize the accuracy of the CFAM deflection model. The CFAM prototypes

performance is shown to match the predicted model, providing confidence for optimizing future designs. Experimental results of low actuation voltage and high displacement suggest that CFAM may be a viable technology for hybrid microdevices and actuators.

Acknowledgments

Foremost, I would like to thank my Advisor Dr. Carl Knospe for his excellent job advising and supporting me throughout my studies, and for giving me the opportunity to work on this captivating field of study. I greatly appreciate that he was always willing to offer advice and input when challenges arouse, going above and beyond to help resolve them. I am also greatly indebted to Prof. Reed for his invaluable research advice and ideas, and for presenting the herein research results at the 2016 Electrowetting meeting in Taiwan.

I would like to thank my defense advisory committee members, Dr. Baoxing Xu, Dr. Eric Loth, Dr. Michael Reed and Dr. Nathan Swami, for their invaluable time and helpful suggestions. Acknowledgment and thanks should be given to Dr. Lander's group in the Chemistry department at UVA for allowing us to use their laser cutter, and the beneficial discussions about microfluidics with Kerui Xu and Kim Jackson. I would also thank the professors and engineers in the clean room, Dr. Art Lichtenberger, Joe Beatrice, Mike Stogoski, Alex Lobo and Tim Pernell, for their advice, assistance, and support in the cleanroom, without which the device fabrication or this thesis would not be possible. I would like to thank Wade Komisar for the computer support, Dwight Dart for 3D printing support, Lewis Steva for machine shop support, Brenda Perkins, Barbara Graves, Jackie Slaughter-Scott, and Lori Pedersen for answering my administrative questions and their constant encouragement.

I would like to thank my fellow Capillary Micro Mechatronics research group members, Xiaoyu Hu, Samantha Mendis, Marcel Mibus and Nick Francis, for all their support and council throughout my time at UVA.

Finally, I would like to thank my friends and family for all their wonderful support and encouragement throughout my life. The experiences and people I have encountered in my time at UVA are irreplaceable, and I will carry them with me for the rest of my life.

Contents

List of Tables

List of Figures

Nomenclature

Arabic

A	Effective area
C	Total capacitance per unit area
$C_{\mathrm{Al_2O_3}}$	Capacitance per unit area of the aluminum oxide layer
C_{CYTOP}	Capacitance per unit area of the CYTOP layer
D	Flexural rigidity
$\widehat{D_i}$	Normalized deflection
D_i	Displacement during actuation i
D_1	Displacement during first deflection phase
E	Young's modulus
F_e	Electrostatic actuator force
h	Capillary bridge height
h_s	Height of glass slide
i	Cycle number
P_c	Capillary pressure
R_1	Waist of the capillary bridge
R_2	Radius of curvature of the bridge surface's profile
r	Radial position
r_c	Capillary bridge radius – wetted capillary bridge
r_{c_0}	Equilibrium capillary bridge radius
r_i	First radius of fustrum geometry
r_j	Second radius of fustrum geometry
r_m	Elastomeric membrane radius

$t_{Al_2O_3}$	Aluminum oxide layer thickness
t_{CYTOP}	CYTOP layer thickness
t_d	Thickness of dielectric layer
t_m	Elastomeric membrane thickness
u	Stretch
V	Applied voltage potential
V_A	Volume in glass slide A
V_B	Volume in glass slide B
V_{Bridge}	Volume in capillary bridge – in wetted configuration
V_{Bridge_0}	Volume in capillary bridge – in equilibrium configuration
V_T	Total volume of conducting drop
V_a	Anodization voltage
$V_{frustum}$	Volume of a fustrum
$V_{membrane}$	Volume in elastomeric membrane
$V_{mem._1}$	Volume in elastomeric membrane – equilibrium configuration
$V_{mem._2}$	Volume in elastomeric membrane – wetted configuration
X	Measured membrane deflection during return
X_n	Rescaled deflection
X_0	Membrane position immediately before voltage is applied
X_1	Fully deflected membrane position immediately prior to return phase
X_∞	Final position at end of the return phase
x	Distance between the electrostatic actuator plates
y	Vertical position

Greek

δ	Vertical position at center of elastomeric membrane
δ_1	Unwetted position at center of elastomeric membrane
δ_2	Wetted position at center of elastomeric membrane
ε_0	Permittivity of free space
$\varepsilon_{r_{Al_2O_3}}$	Relative permittivity of aluminum oxide
$\varepsilon_{r_{CYTOP}}$	Relative permittivity of CYTOP
ε_d	Dielectric constant
ε_i^0	Residual strain
ε_θ^0	Circumferential strain through the center thickness of the membrane
∇	Biharmonic operator
ν	Poisson's ratio
ϕ	Airy stress function
σ_{GL}	Surface Tension or Interfacial energy between liquid and vapor phases
σ_{GS}	Interfacial energy between solid and vapor phases
σ_{LS}	Interfacial energy between liquid and solid phases
σ_r^0	Radial stress through the center of the membrane
σ_θ^0	Circumferential stress through the center of the membrane
τ	Return time constant
θ	Contact angle
θ_0	Equilibrium contact angle
θ_L	Lower apparent contact angle

θ_{L_0}	Lower equilibrium contact angle
θ_v	Apparent contact angle
θ_U	Upper apparent contact angle
θ_{U_0}	Upper equilibrium contact angle
ζ	Deflection ratio

Chapter 1

Introduction

1.1 Hybrid Microdevices and Microactuators

Microelectromechanical systems (MEMS) have been traditionally been manufactured utilizing silicon micromachining techniques. However, the inherent stiffness of glass and silicon-based MEMS hinders their performance. Hybrid microdevices with soft elastomeric components are increasingly being recognized as alternatives to traditional silicon fabricated MEMS, due to their lower modulus of elasticity [2, 3]. A lower modulus means that hybrid devices achieve desired deflections utilizing less actuation force. This reduces both the on-chip space and power needed for actuators, such as actuated elastomeric membranes [1] – the focus of this thesis.

However, complementary actuation technology is needed, to implement the capabilities of elastomeric components. Traditional MEMS actuation types are electrostatic, electromagnetic, piezoelectric, and thermal. Each traditional approach has significant disadvantages with respect to one or more of the following performance metrics: force capability, actuator stroke, power required, bandwidth, and ease of integration with elastomeric components [4–7]. The most commonly used actuators in MEMS technology are electrostatically driven. In the parallel plate configuration, the force generated by electrostatic actuators (F_e)

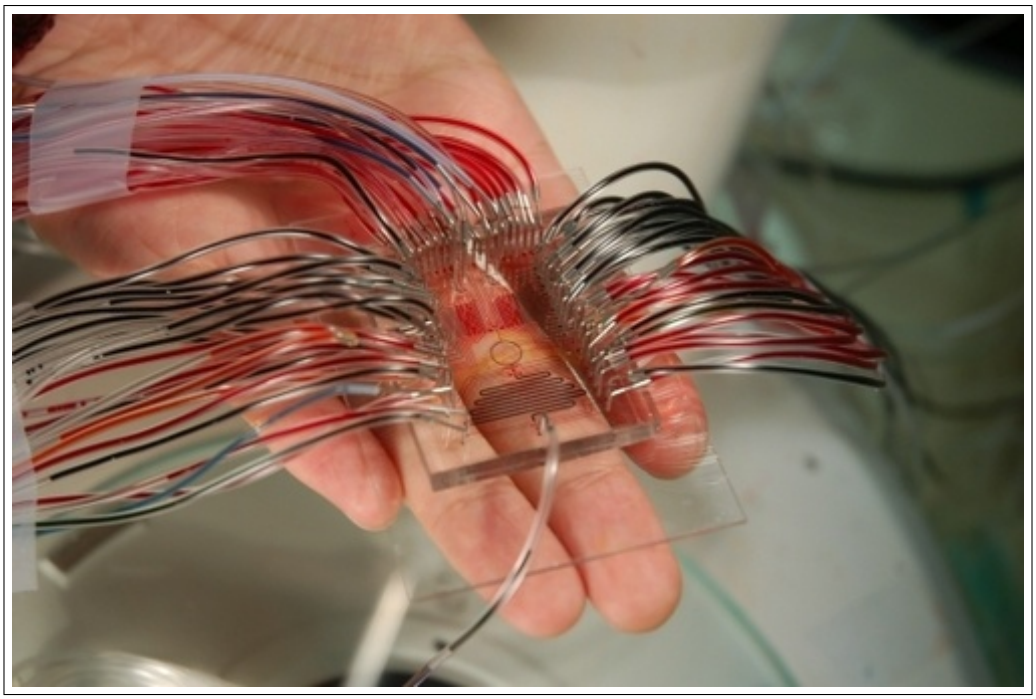

Figure 1.1: LOC able to perform 1040 chemical reactions in parallel. Red lines are associated with Pneumatic lines. Adapted from Wang et al. [17].

may be described as:

$$F_e = \frac{1}{2}\frac{\varepsilon_0 A}{x^2}V^2 \tag{1.1}$$

Where ε_0 is the permittivity of free space, A is the effective plate area, x is the distance between the plates, and V is the applied voltage between the plates. Shortcoming of electrostatic actuators are demonstrated by this equation 1.1. The deflection is limited the by the distance between the plates. The plate area and height are inversely related causing difficulties downscaling both the area and the height. Additionally, typical electrostatic actuators require voltages much higher than is desirable for MEMS, often greater than 60V. Electrostatically actuated membranes are also limited by same the parameters as traditional electrostatic actuators [8–16], where an actuation of 7 microns is achieved using 120V of applied voltage [8].

Applications of elastomeric membranes include Lab-on-a-Chip (LOC) , adaptive optics, braille displays [18], and microendoscopes [19, 20]. LOC takes chemical and biological lab-

oratory analysis and miniaturizes them into microdevices. The miniaturization allows for a faster analysis utilizing smaller samples [21]. The chip shown in Figure 1.1 is capable of handling 1024 chemical reactions in parallel [17]. This is extraordinary, the reader should note the large number of external connections that are required by current LOCs. Much of the complexity seen is related to the large number of microvalves and micropumps needed for fluid flow management [22]. The actuation of these is commonly achieved pneumatically using an external air pump, with an elastomeric membrane as the valve moving-element [23, 24]. Similar designs are common for flow generation, including peristaltic and diaphragm pumps [23, 25]. Adaptive optics systems correct image distortion through the adjustment of the surface shape of a deformable mirror to alter the light wavefront. Mirror shape change is achieved by electrical signals to arrays of actuators behind the mirror surface. Most adaptive optic systems operate using high voltages and a limited range of motion, of $\sim$1 micron. Adaptive Optic systems are now common in astronomical imaging and are making headway into diagnostic retinal imaging [26–30]. Because of this there is a necessity for larger actuation strokes [26, 29].

1.2 Capillary Force Actuators

CFAs are a fundamentally new technology for microscale actuation based upon electrowetting on dielectric (EWOD). EWOD is the spreading of a conductive liquid on a dielectric surface caused by the application of a voltage potential. The CFA is constructed by placing a conducting liquid bridge between two electrodes, each covered with a dielectric layer (see Figure 1.2). When voltage potential is applied, the liquid bridge undergoes EWOD. This causes a change in the capillary pressure (via change in the contact angle) causing an attractive force between the two electrodes. If one electrode is supported by compliant flexures it will move in response to this force. Alternatively, if the liquid bridge is in contact with an elastomeric membrane the change in pressure will result in deflection of the membrane [31].

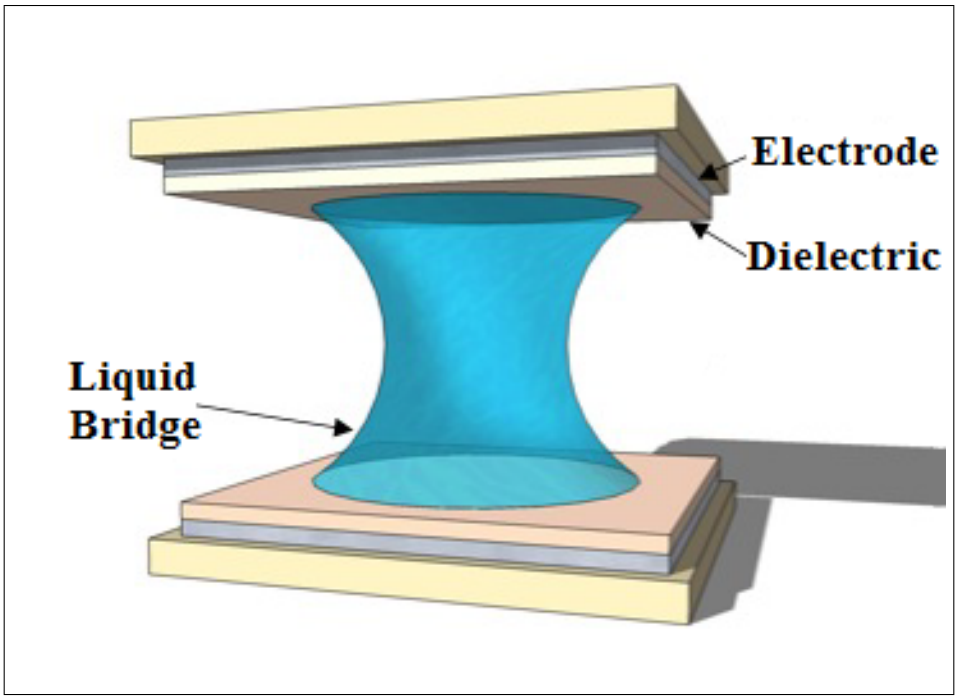

Figure 1.2: Standard CFA configuration.

Capillary pressure is an ideal mechanism for the deformation of membranes (or other soft structures) in microfluidic devices, as the electrodes do not need to be integrated into the soft elements.

CFAs are capable of producing extraordinary electrowetting forces and displacements relative to comparable actuation methods [31–35]. Wang et al. was able to demonstrate a 25 to 100 times greater force than comparable electrostatic methods. In the experiment a liquid bridge was placed between a fixed plate electrode and a plate electrode supported by micro-machined beam flexures. Both electrodes were manufactured from silicon wafers that were covered by a 30 nm oxide film and a 30 nm hydrophobic polymer. The liquid bridge was 100 µm in height and approximately 1 mm in diameter. A maximum deflection of 5 µm was achieved with 40 Volts applied. This corresponds to an actuation force of over 200 µN. For comparison, a parallel plate electrostatic actuator with the same area and electrode gap would achieve only 3 µN at this voltage [34], an increase of ∼6500%.

1.2.1 Device Physics

As with most MEMs devices, gravity may be ignored as it has negligible effect. For CFA in static equilibrium without applied electric field, the energy is that of the surfaces alone. The capillary bridge satisfies Laplace's equation (constant mean curvature) subject to the boundary condition at the contact line dictated by Young's equation,

$$\sigma_{GS} - \sigma_{LS} - \sigma_{GL}\cos(\theta_0) \tag{1.2}$$

which expresses the contact angle of the liquid θ_0 in terms of the interfacial energies (σ) between the liquid (L), solid (S), and vapor (G) phases [36]. The capillary pressure is given by Laplace's equation –

$$P_c = \sigma_{GL}\left(\frac{1}{R_1} + \frac{1}{R_2}\right) \tag{1.3}$$

whereR_1 and R_2 are the radii of curvature of the liquid's free interface, and σ_{GL} is the interfacial energy between liquid and vapor, more commonly known as surface tension. Figure 1.3, shows a schematic of the radii of curvature for an axisymmetric liquid bridge. Applied voltage results in a change in capillary bridge shape, through an increase in R_1 and change in contact angle in R_2, as this is the only effect of the electric field [31].

1.3 Electrowetting

Electrocapillary wetting was introduced by Lippmann in 1875 [37]; Berge later initiated research of EWOD principles. Electrowetting is an electromechanical phenomenon in which the applied electric field causes an electrostatic pressure on the liquid surface near the contact line [38]. A standard sessile drop EWOD setup is shown in Figure 1.4. A wetting liquid sits on top of a planar electrode covered with a thin dielectric layer and a hydrophobic layer. Applying a voltage between the liquid and the electrode changes the apparent contact angle of the wetting liquid. Two other standard configurations of EWOD are parallel plate

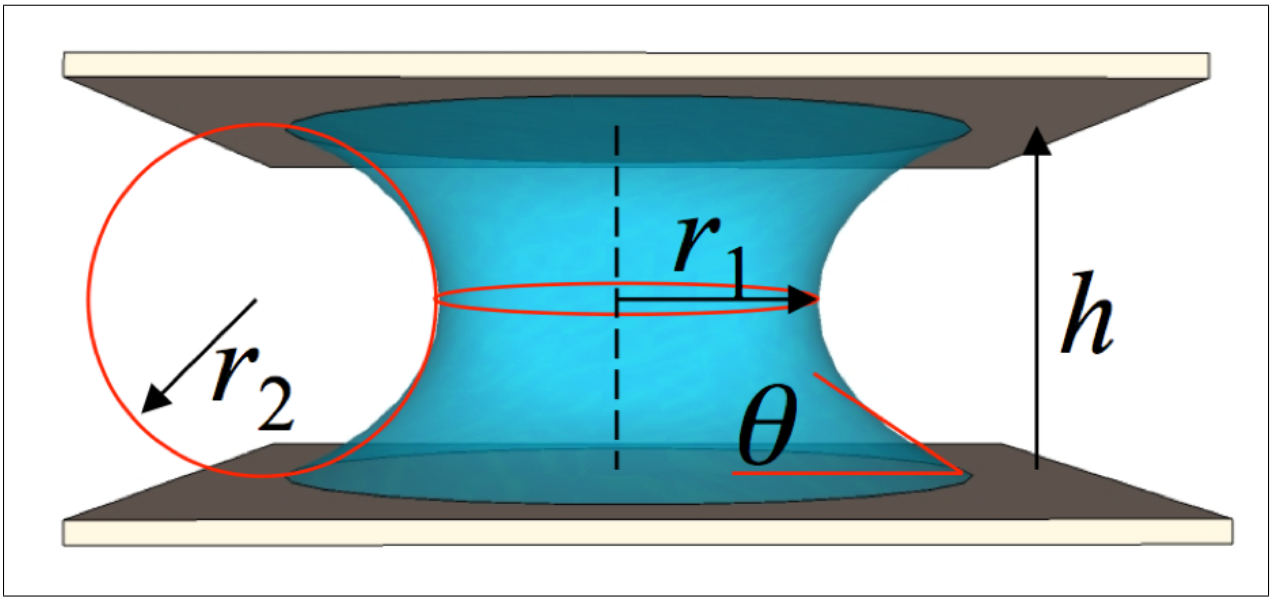

Figure 1.3: Schematic of capillary bridge, in wetted (low apparent contact angle) configuration.

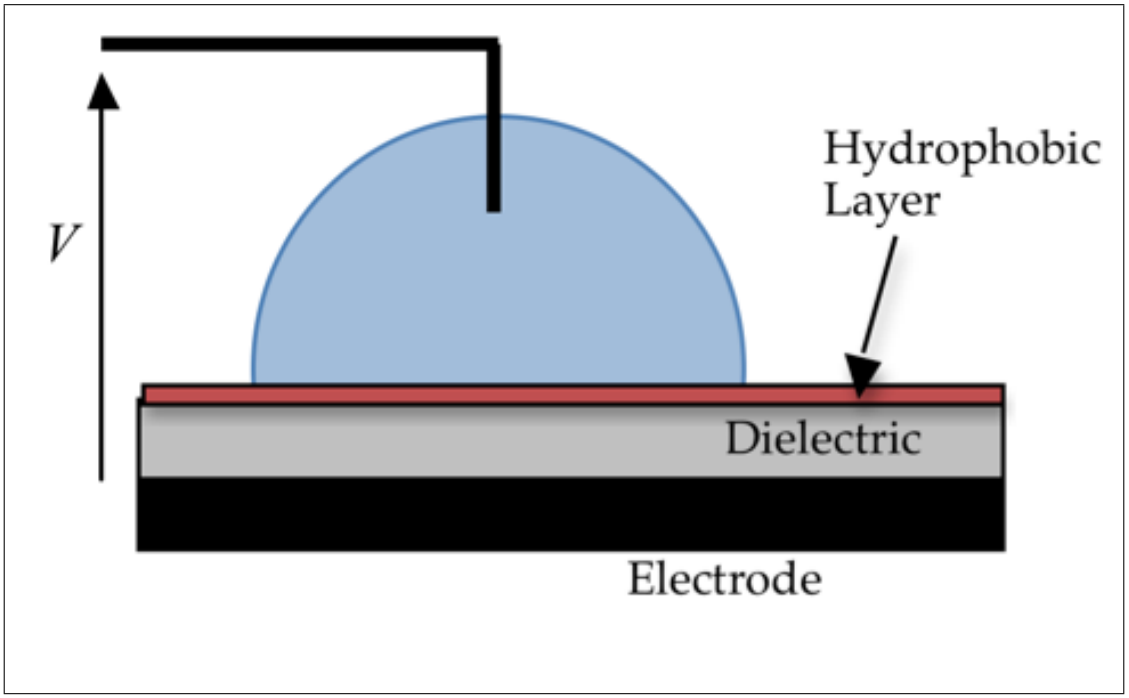

Figure 1.4: Standard sessile drop EWOD configuration.

electrode configurations with either: one bare electrode and one dielectric covered electrode, or both electrodes covered with dielectric layers [39]. The apparent contact angle is described by the Lippmann-Young equation :

$$\cos(\theta_v) = \cos(\theta_0) + \frac{\varepsilon_0}{2\sigma_{GL} t_d} V^2 \tag{1.4}$$

where ε_d is the dielectric constant, t_d is the thickness of the dielectric layer, θ_v is the apparent contact angle with an electric field, θ_0 is the equilibrium contact angle without an electric field, and V is the voltage applied to the device [37]. The Lippmann-Young equation 1.4 predicts that perfect wetting (i.e., zero contact angle) will be achieved at a finite voltage, however in practice this is unfortunately not true. The contact angle will cease to decrease beyond a certain voltage. This suspension of wetting is a phenomenon known as contact angle saturation (CAS), where the onset angle and voltage are referred to as the saturation angle and voltage respectively. Several mechanisms have been proposed for contact angle saturation, but the phenomena is still not fully understood nor resolved. The majority of CAS mechanisms are related to the leakage of charge near the contact line. These include instability of the contact line and expulsion of satellite droplets; charge trapping in the dielectric layer; and electrical breakdown of the dielectric layer [38, 40–43]. Several of the proposed CAS mechanisms may be responsible for anomalous electrowetting behavior at voltages above the contact angle. It should be noted that the maximum pressure capillary pressure change is at the saturation angle, since the angle will no longer decrease with increased voltage potential.

An overview of the physics of electrowetting will be given here, a with a greater discussion found in [38]. The liquid is assumed to be perfectly conducting, as the conducting liquids typically have a very high conductivity (5 to 15 times the order of the dielectric layer) [35]. When electric potential is applied, it causes an electric field, which results in the migration of ions in the liquid. The free charge appears at the liquid's interface and screens the electric

field from the liquid's interior, in the perfectly conducting case.

An electrostatic pressure is applied to the interface by the interaction of the ions with the electric field created by the applied voltage [44]. The conducting liquid is pulled, wetted, outward in response to this pressure. Significant electrowetting results in strong local curvature of the gas-liquid interface proximate to the contact line, which creates the effective contact angle that determines the free interface. It should be noted that since the surface energy of the solid/liquid interface is unchanged, the actual contact angle in electrowetting is not altered by the application of voltage – it remains θ_0. It is this change in apparent contact angle that is captured by the Young-Lippmann equation, 1.4, and it is typically measured via optical imaging. The transition of the liquid profile tangent from native contact angle (θ_0) to apparent contact angle (θ_v) is not easily imaged since the characteristic length scale of the transition is the dielectric thickness.

The local electric field present in the dielectric layer is dependent on both the electric potential of the liquid and the shape of the interface in this region. The applied electric potential results in a buildup of a charge double layer at the dielectric / electrode interface and the dielectric / liquid interface. The free charge is in the conducting bridge and electrode, and polarization charge is in the dielectric [45, 46]. The capacitance of this arrangement will be essentially equal to that of the dielectric layer itself. In summary, the application of electric potential results in charge migration, the alteration of the liquid bridge profile, and the redistribution and concentration of the local electric field in the dielectric layer.

Applications of electrowetting are numerous, several examples include microfluidics [47–51], autofocus lenses [52], display systems [53–56], capillary motors [57], microswitches [58], and actuators [34, 35, 59–61].

1.4 Thesis Layout

Chapter 2 – CFAM Theory and Design will provide the physical design, governing equations for CFAM, and parameter selection.

Chapter 3 – will describe the CFAM fabrication process, the prototype assembly process, and experimental set-up.

Chapter 4 – Static CFAM dual active surface results will present the static performance of the dual active surface CFAM prototypes.

Chapter 5 – Static CFAM single active surface static results will present the performance of the single active surface CFAM prototypes.

Chapter 6 – Dynamic and Dielectric Performance Results will discuss the dynamic performance of the CFAM, and the performance of its dielectric layer.

Chapter 7 – Conclusions and Future work will summarize the current research and explore future research efforts.

Chapter 2

Theory and Design of CFAM Devices

This chapter will detail the governing equations and design of CFAM devices. An overview of device configuration is provided in Section 2.1. Governing equations are presented in Section 2.2. Parameters are selected based on available fabrication processes and present micro device dimensional parameters (Section 2.3). The Saturated Lippmann-Young model is presented in Section 2.4. Additional design considerations are discussed in Section 2.5, and CFAM device deflection design plots are presented in Section 2.6.

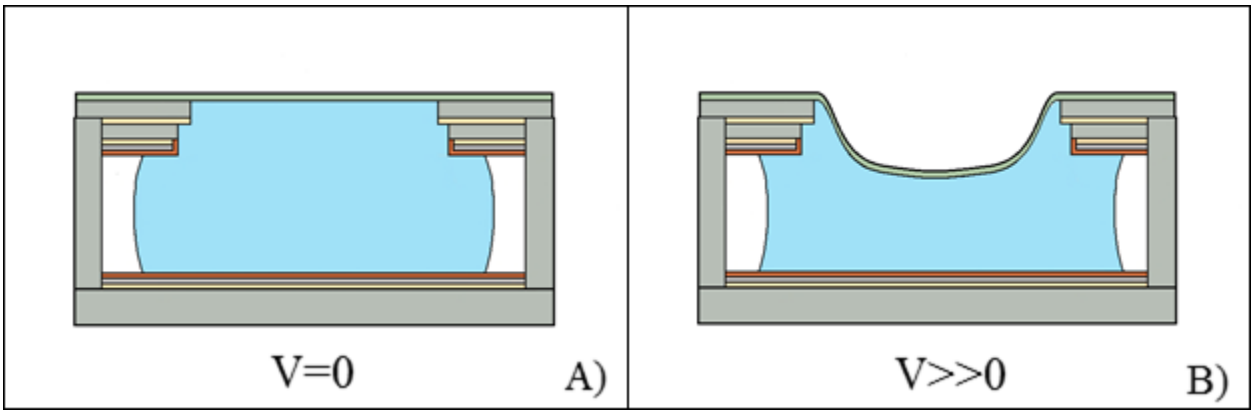

Figure 2.1: Comparison of CFAM in A) unwetted and B) wetted configuration.

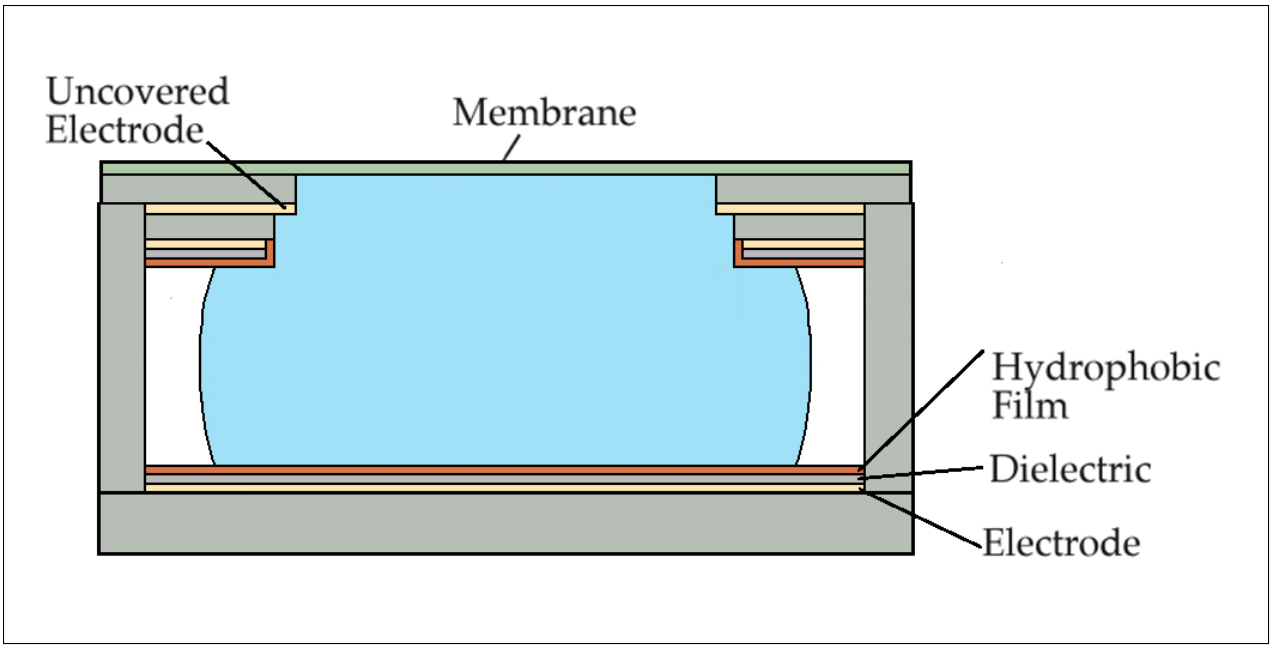

Figure 2.2: CFAM-DAS Device.

2.1 Device Overview

In the CFAM devices studied in this thesis, a conducting liquid bridge extends between the two electrodes. When voltage is applied and electrowetting occurs the change in contact angle results in a change in the curvature of the liquid bridge's profile. From Laplace's equation (1.3) for the pressure change across an interface, this change in curvature results in a decrease in the capillary pressure of the liquid. If the liquid bridge is in contact with an elastomeric membrane the resulting change in pressure will result in the deflection of the membrane – see Figure 2.1.

Two types of CFAM devices are designed herein. The first design configuration has three electrodes with two of the electrodes covered by a dielectric layer. This design is called the *Dual Active Surface* CFAM device (CFAM-DAS) since electrowetting occurs on both parallel plate surfaces that terminate the conducting liquid bridge, see Figure 2.2. The droplet is also in contact with a bare electrode and the two dielectric layers are in parallel in the resulting circuit. The reader will note that the lower surface in the figure has a single dielectric covered electrode that forms an active surface. The upper surface for this design has one electrode

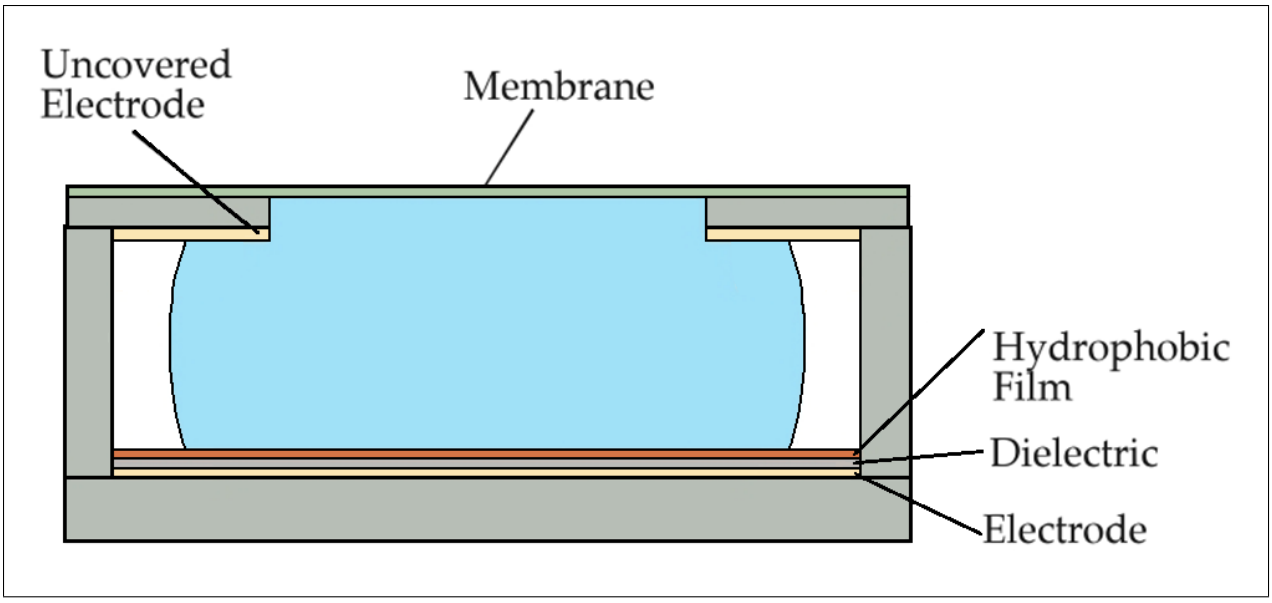

Figure 2.3: CFAM-SAS Device.

covered in a dielectric layer (the second active surface) and the other bare electrode that is connected to ground to complete the circuit.

The second design configuration has only one dielectric covered electrode. This design is called the *Single Active Surface* CFAM device (CFAM-SAS). It is composed of a conducting aqueous droplet in contact with electrodes on two parallel surfaces – see Figure 2.3. The lower surface has a single dielectric covered electrode which forms an active surface. The upper surface of this device has a single uncovered electrode. This electrode is a passive (non-electrowetting) surface.

2.2 Governing Equations

The change is capillary pressure induced by electrowetting will drive the deflection of the device membrane. The capillary pressure is given by Laplace's Equation (1.3). The CFAM is a low aspect bridge type, $R_1 >> h$, this allows for the assumption that R_1 equals the waist of the capillary bridge (r_c), also referred to as the capillary bridge radius. Low aspect bridges may also be called "pancake bridges". Furthermore, the radius of curvature of the

capillary bridges surface profile may be estimated as circular arcs –

$$R_2 = \frac{-h}{\cos(\theta_L) + \cos(\theta_U)} \tag{2.1}$$

where θ_L and θ_U are the lower and upper contact angles respectively, and h is the capillary bridge height [31]. The resulting capillary pressure is:

$$P_c = \sigma_{GL}\left(\frac{1}{r_c} - \frac{\cos(\theta_L) + \cos(\theta_U)}{h}\right). \tag{2.2}$$

Note the given formulation of R_2 is for a capillary bridge with unequal contact angles, if the upper and lower angles are symmetric, R_2 and P_c may be estimated as, respectively:

$$R_2 = \frac{-h}{2\cos(\theta)} \;\; \& \tag{2.3}$$

$$P_c = \sigma_{GL}\left(\frac{1}{r_c} - \frac{2\cos(\theta)}{h}\right). \tag{2.4}$$

However, it was discovered upon experimental implementation that the contact angles on the upper and lower surfaces are rarely equal for CFAM devices due to the fabrication and assembly. The values of the bridge height, and contact angles are determined via side view profile images of the capillary bridge.

Equation 2.4 helps demonstrate the impact of contact angle, i.e. bridge surface profile, on the capillary pressure. When the contact angle is hydrophobic (greater then 90 degrees) the cosine of the contact angle will be negative resulting in a positive of radius of curvature; if the contact angle is hydrophilic the radius of curvature for the bridge will remain negative (since the cosine of the contact angle is positive) resulting in a decrease in capillary pressure from the hydrophobic case, see Figure 2.4.

For the CFAM-DAS device both the upper and lower angles will change due to electrowetting, while the CFAM-SAS device will have electrowetting only on the active lower surface.

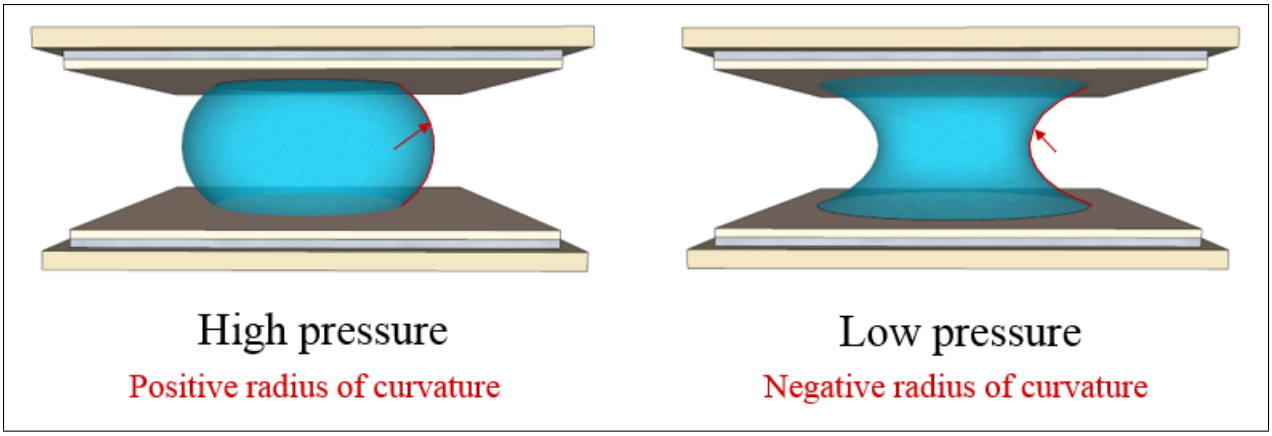

Figure 2.4: Schematic of positive and negative radii of curvature.

The passive upper surface should see no change in contact angle resulting in approximately half the pressure change achieved in an otherwise similar CFAM-DAS device.

2.2.1 Capillary Bridge Radius calculation

The capillary radius is determined via volumetric analysis, since the field of view of the side profile imaging is not great enough to image the entirety of the capillary diameter. It is assumed that capillary bridge of the CFA is perfectly cylindrical, corresponding to "pancake" bridge theory. The capillary radius is then calculated from the volume of the conducting drop in the capillary bridge. The volume in the capillary bridge is found by subtracting the additional "dead" volumes within the CFAM hole from the total dispensed volume.

The cut geometry in the upper glass surfaces are assumed to have a volume of a frustum, since the holes have tapered diameters–

$$V_{frustum} = \frac{1}{3}\pi h_s \left(r_i^2 + r_i r_j + r_j^2\right) \tag{2.5}$$

where h_s is the height of the glass slide (120 µm), r_i is the radius of smaller hole, while r_j is the radius of the second hole.

The membrane volume is calculated via method of shells integration over the curvature

of the membrane:

$$V_{membrane} = \int_0^{r_m} \delta \left[1 - \left(\frac{r}{r_m}\right)^2\right]^2 (2\pi r)\, dr = \frac{\pi \delta r_m^2}{3} \tag{2.6}$$

where r_m is the elastomeric membrane radius, and r is the radial position. δ is the membrane position, thus the value of membrane volume will sign dependent on the membrane position, positive for upwards deflection and vise-versa.

The volume of the membrane is dependent on the maximum displacement of the membrane, for which the value of capillary radius is required. To overcome this, the approximate positions of the membrane is calculated with a capillary radius that excludes the membrane volume. Then utilizing the approximate positions, the capillary radius is recalculated – including the membrane volumes. Then the resulting capillary radius is used to recalculate the final membrane positions. The difference between membrane positions calculated with and without the membrane volume is under 1% (with the initial solution underestimating the membrane displacement). The volumetric change in radius is purely affected by the change in membrane position – the smallest volume. The magnitude of the capillary radius plays a larger role in capillary pressure than the change in capillary radius.

Below is a sample calculation for capillary bridge radius for a CFAM-DAS device. To apply the calculation to a CFAM-SAS devices only the volume of the slide B must be removed, for CFAM-SAS is lacking this feature. Figure 2.5 & Figure 2.6 shows a schematic of the volumetric dimensions.

The components of the unwetted configurations are as follows – for the volume within the glass slides, for V_A and V_B respectively:

$$V_A = \frac{1}{3}\pi h_s \left(r_m^2 + r_m r_{j_A} + r_{j_A}^2\right) \quad \& \tag{2.7}$$

$$V_B = \frac{1}{3}\pi h_s \left(r_{i_B}^2 + r_{i_B} r_{j_B} + r_{j_B}^2\right) \tag{2.8}$$

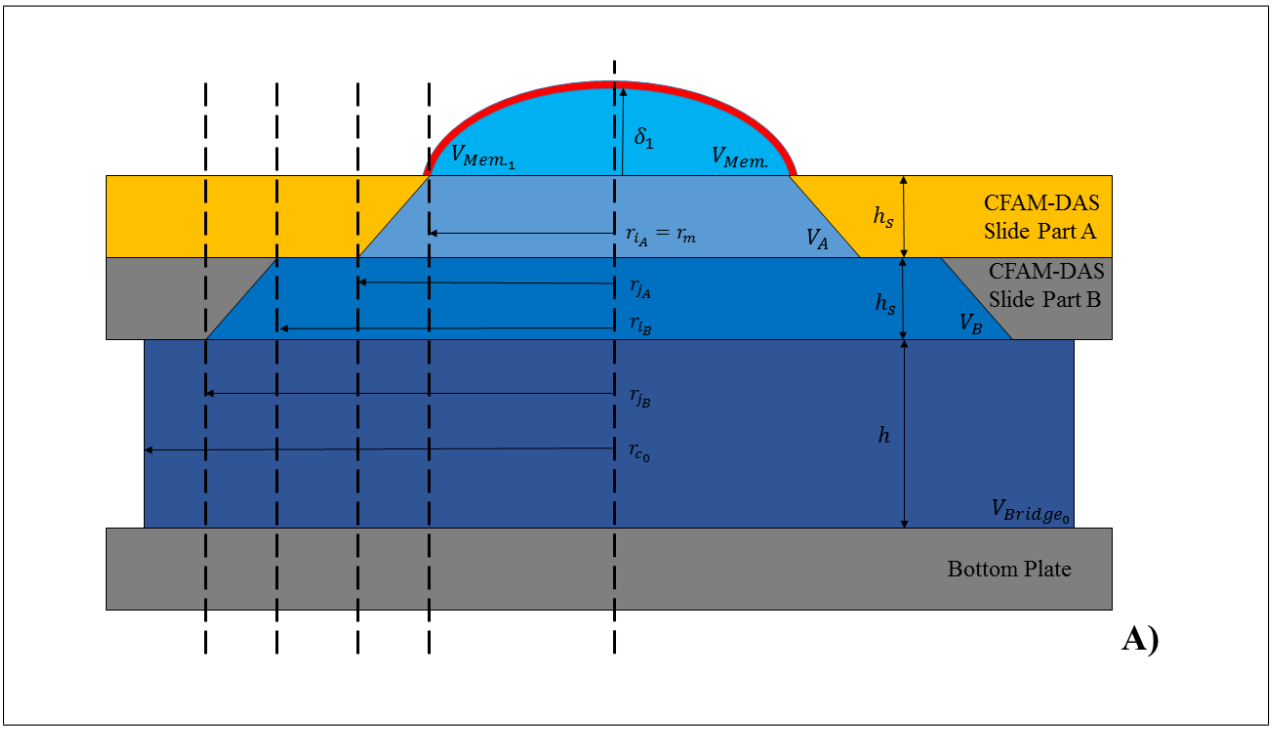

Figure 2.5: CFAM-DAS volume distribution schematic for the unwetted configuration.

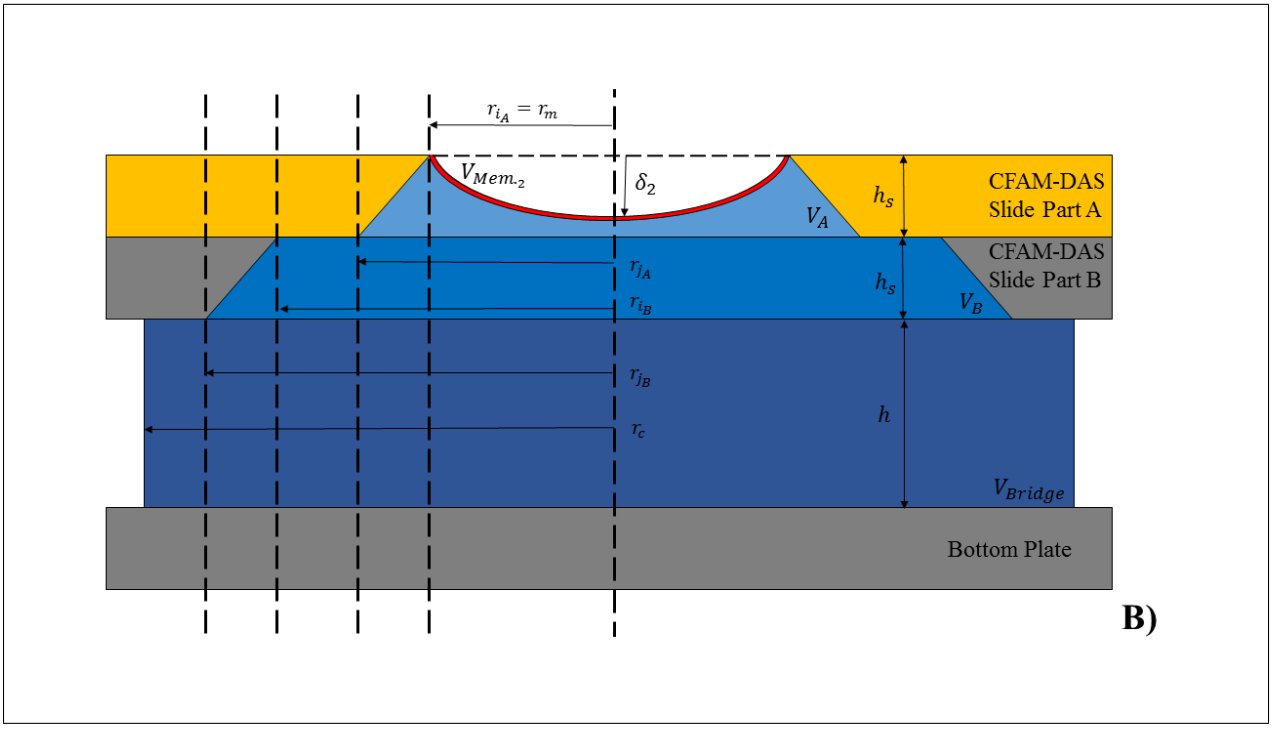

Figure 2.6: CFAM-DAS volume distribution schematic for the wetted configuration.

where r_{j_A} is the larger radii of the plate A, r_{j_B} is the larger radii of the plate B, and r_{i_B} is the smaller radii of the plate A. The initial membrane volume is calculated as:

$$V_{mem.1} = \frac{\pi \delta_1 r_m^2}{3} \tag{2.9}$$

where δ_1 is the initial membrane position. In most cases, the membrane is deflecting upwards, a positive value of δ_1, in the initial unwetted position. The initial volume in the capillary bridge (V_{Bridge_0}) is found by calculating the remaining volume not accounted for in the other CFAM geometries from the total dispensed volume.

$$V_{Bridge_0} = V_T - V_A - V_B - V_{mem.1}. \tag{2.10}$$

The capillary bridge radius is then found from the volume of cylinder:

$$r_{c_0} = \sqrt{\frac{V_{Bridge_0}}{\pi h}} = \sqrt{\frac{V_T - V_A - V_B - V_{mem.1}}{\pi h}}. \tag{2.11}$$

For the wetted configuration the volume calculations for V_A and V_B are the same as the unwetted case. The volume of the membrane is now most cases filled with air as the membrane is deflecting downward, this results in a negative absolute position (δ_2):

$$V_{mem.2} = \frac{\pi \delta_2 r_m^2}{3}. \tag{2.12}$$

The wetted bridge volume is found as

$$V_{Bridge} = V_{Bridge_0} + \left(V_{mem.1} - V_{mem.2}\right). \tag{2.13}$$

The final capillary radius is similar to the unwetted case:

$$r_c = \sqrt{\frac{V_{Bridge}}{\pi h}}. \tag{2.14}$$

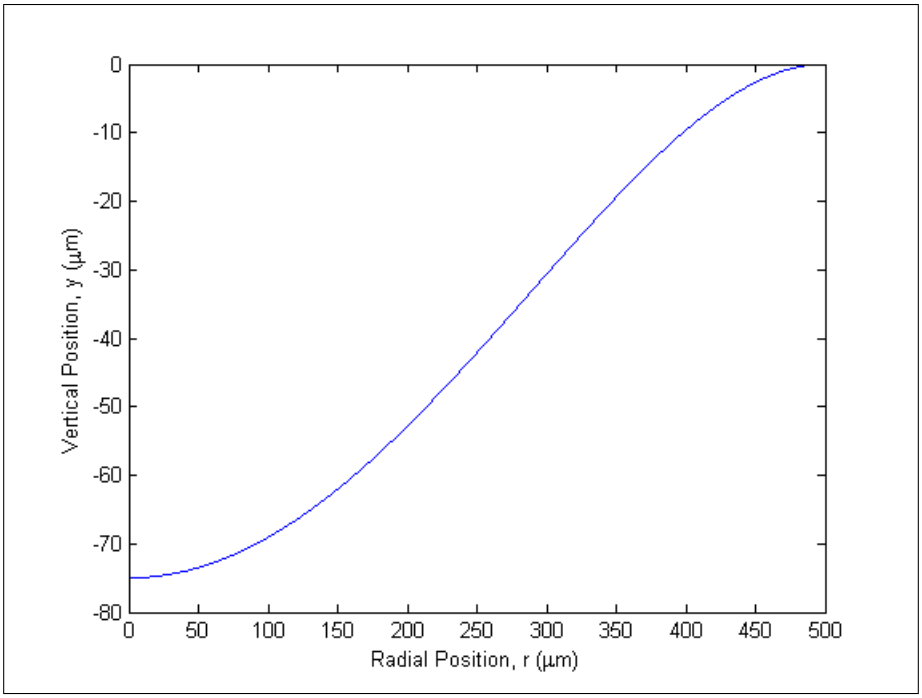

Figure 2.7: Sample membrane position curve.

2.2.2 Membrane Deflection

The solution for large deflection of a membrane or diaphragm under uniform pressure is previously solved and widely accepted [62]. The summarized solution is presented here. Large displacement of a membrane is appropriate for up to 3 times the diaphragm thickness. Some presented cases fall into the regime where they are applicable to be solved with small deflection theory, where deflection is less than 1/5 of the diaphragm thickness. However, for uniformity large deflection theory will be used in the analysis of the CFAM as it is applicable in the small deflection regime [63]. Additionally, small deflections theory over estimates membrane deflection as deflections approach large deflection regime.

The vertical position, y(r) of the membrane for small and large deflection theory over the radial position (r) is

$$y(r) = \delta \left[1 - \left(\frac{r}{r_m} \right)^2 \right]^2 . \tag{2.15}$$

where r_m is the radius of the membrane, and δ is the maximum deflection under the applied pressure. Figure 2.7 gives a sample deflection curve. To calculate the δ, we begin with the

governing differential equation for the bending of a circular plate [62]:

$$\nabla^4 y = \frac{P_c}{D} + \frac{t_m}{Dr}\frac{\partial \phi}{\partial r}\frac{\partial^2 y}{\partial r^2} \tag{2.16}$$

where P_c is the applied capillary pressure, D is the flexural rigidity, t_m is the membrane thickness, ∇^4 is the biharmonic operator, and ϕ is the Airy stress function. The flexural rigidity (D) is defined as:

$$D = \frac{E t_m^3}{12\left(1-\nu^2\right)} \tag{2.17}$$

where E and ν are the membranes Young's modulus and Poisson's ratio, respectively. The biharmonic operator is given by:

$$\nabla^4 = \left(\frac{\partial^2}{\partial r^2} + \frac{1}{r}\frac{\partial}{\partial r}\right). \tag{2.18}$$

There are 3 assumed boundary conditions. The first set are clamped boundary conditions:

$$y\left(r_m\right) = 0 \;\; \& \tag{2.19}$$

$$\left.\frac{\partial y}{\partial r}\right|_{r=r_m} = 0 \tag{2.20}$$

The final boundary condition is: that the amount of stretch at the edge is 0:

$$u|_{r=r_m} = \left. r\left(\varepsilon_\theta^0 - \varepsilon_i\right)\right|_{r=r_m} = 0 \tag{2.21}$$

where ε_θ^0 is the circumferential strain through the center thickness of the membrane, ε_i is the build-in residual strain, and u is the stretch. The boundary condition is further developed to be:

$$\left.\varepsilon_\theta^0\right|_{r=r_m} = \left.\frac{1}{E}\sigma_\theta^0 - \nu\sigma_r^0\right|_{r=r_m} = \varepsilon_i \implies \frac{\partial^2 \bar{\phi}}{\partial r^2} - \frac{\nu}{r}\frac{\partial \bar{\phi}}{\partial r} = \varepsilon_i E, \tag{2.22}$$

where σ_r^0 & σ_θ^0 are the respectively the radial and circumferential stresses through the center of the membrane. The deflection and Airy stress function have the presumed solutions, respectively:

$$y(r) = \delta(1 + C_1 r^2 + C_2 r^4) \;\; \& \tag{2.23}$$

$$\phi = \delta^2(B_1 + B_2 r^4 + B_3 r^6 + B_4 r^8) \tag{2.24}$$

where B and C are constants. Applying the boundary conditions yields the membrane position, equation 2.15, and:

$$\phi(r) = \frac{\delta^2 E}{12}\left[\left(\frac{5-3\nu}{1-\nu}\right)\left(\frac{r}{r_m}\right)^2 + \frac{\varepsilon_i}{2(1-\nu)}\left(\frac{r}{r_m}\right)^2 - \frac{1}{4}\left(\frac{r}{r_m}\right)^4 + \frac{1}{9}\left(\frac{r}{r_m}\right)^6 \frac{1}{48}\left(\frac{r}{r_m}\right)^8\right] \tag{2.25}$$

The maximum deflection is found by minimizing Equation 2.16, and assuming $y(r)$ is orthogonal with respect to all other coordinate functions:

$$\int_A y\left[D\nabla^4 y - \frac{t_m}{r}\left(\frac{\partial}{\partial r}\right)\left(\frac{\partial \phi}{\partial r}\frac{\partial y}{\partial r}\right) - P_c\right] dA = 0. \tag{2.26}$$

Integrating a collecting terms results in a cubic equation, the real root of the solution is the maximum displacement δ:

$$\delta^3 \frac{2Et_m(1+\nu)(23-9\nu)}{63r_m^2(1-\nu)^2} + \delta\frac{16Et_m^3}{9r_m^2(1-\nu^2)} - \frac{P_c r_m^2}{3} = 0 \tag{2.27}$$

Note, that δ must be solved for with absolute pressure not change in pressure.

2.3 Parameter Selection

The parameters of dispensed volume, bridge height, membrane radius, and membrane thickness, are selected based on desired membrane deflection (in some cases motivated by previous micro devices [8]), available fabrication techniques, and previous CFA research [34, 35]. The membrane parameters are chosen to be in the range of the typical electrostatic microvalve

Table 2.1: Parameters of CFAM Prototypes.

CFAM Parameter	CFAM-DAS Value	CFAM – SAS Value
Membrane Radius	338 – 480 µm	438 – 510 µm
Membrane Thickness	35 – 47 µm	24 – 50 µm
Bridge Height	45 – 122 µm	91 – 125 µm
Volume of the Conductive Liquid	1.2 – 1.5 µL	0.225 – 1.05 µL
Initial Capillary Radius	1759 – 2460 µm	685 – 1805 µm
Membrane Deflection	12.1 – 75.7 µm	3.0 – 15.5 µm

membranes, which to correspond with typical dimensions in microfluidics, as given by Desai et al. The typical membrane radii (r_m) are 50 to 500 µm. The typical membrane thicknesses (t_m) are 5 to 40 µm. Lastly the channel height is 2-20 µm, the channel height is used to give a target deflection of the CFAM device.

Table 2.1 gives a summary of tested device parameters. The membrane thickness and membrane radii are on the higher end of literature values. Thinner membranes tear easily with manipulation, and the laser cutter is not capable of making uniform holes in borosilicate below 300 µ. The height of the capillary bridge was chosen to closely match the bridge height of previous CFA work [34, 35], and to improve upon it by decreasing the height. The lower limit of the bridge height is 45 µm, for this is the limit of that side view profiling was possible. The deflections are much greater than the channel height, this is to demonstrate the incredible very large displacement possible in CFAM devices.

The dispensed volume is chosen based on the available micropipette device, 0.1-2.5 µL (Eppendorf). Smaller volumes will require more precise volume dispensation methods such as inkjet printing. The volumes are also chosen to have a capillary bridge radius large enough to sit upon the intended surface. and to minimize on-chip area, a radius approximately 1-2 mm greater than the start of the intended surface. Additionally, the CFAM-SAS device volumes were chosen to correspond with the location of the pinning ring. The volumes ranged in value from 0.225 to 1.5 µL and the corresponding capillary radii range is 685 to 2460 micron, depending on CFAM device parameters.

Table 2.2: Electrowetting Parameters.

CFAM Parameter	CFAM-DAS Value	CFAM – SAS Value
Relative permittivity of Al_2O_3	9.0	9.0
Al2O3 thickness	30.6 nm	45 nm
Relative permittivity of CYTOP	2.1	2.1
CYTOP thickness	50.8 nm	∼45 – ∼60 nm
Surface tension of the conductive liquid	68 mN/m	68 mN/m
Saturation Voltage	14 V	16 – 20 V

2.3.1 Electrowetting properties

The electrowetting design parameters are summarized in Table 2.2. The dielectric layer, aluminum oxide (Al_2O_3), is chosen for ease of fabrication and for maximum apparent contact angle change at low voltages. The hydrophobic layer on the active and passive surfaces is chosen to be CYTOP, for its high equilibrium contact angle, ∼103° with the selected electrolyte. The selected electrolyte is 0.1Mol Cs_2SO_4 with 10 µMol of Fluorescein salt. The Fluorescein salt is used to illuminate the drop for side view profile imaging. The surface tension is found to be 68 mN/m from Wilhelmy plate tensiometer testing.

2.4 Saturated Lippmann-Young Model for Apparent Contact Angle

This section provides details of the Saturated Lippmann-Young model that was developed to predict the wetted angles for cases of the CFAM-DAS devices when the contact angle is outside of the field of view. The memory-less model uses the Lippmann-Young equation to predict the apparent contact angle at the test's applied voltage potential, using the test's equilibrium contact angle and dielectric layer properties. However, the model also takes into account contact angle saturation. If a theoretical prediction uses the Saturated Lippmann-Young model this will be stated. The model functions in the following fashion: if the applied

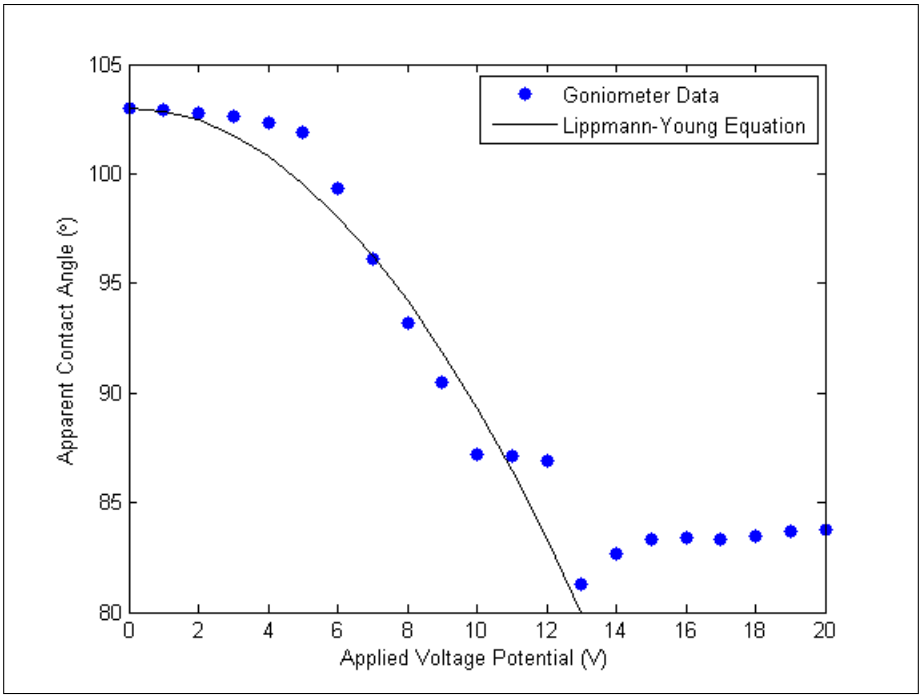

Figure 2.8: Sample goniometer sessile drop electrowetting curve.

voltage potential is below the saturation voltage the apparent angle is calculated using the (conventional) Lippmann-Young equation (1.4). If the calculated contact angle is below the specified saturation angle value, then the predicted contact angle is set to the saturation angle. If the applied voltage potential is at or above the saturation voltage the saturation angle is used. The parameters required to define this model are the saturation voltage for the dielectric layer, saturation angle, and the thickness of the CYTOP hydrophobic layer.

A goniometer tests are used to find the parameters needed for the Saturated Lippmann-Young model used in this study. Figure 2.8 shows an electrowetting curve for the dielectric layer used in the CFAM-DAS devices. The saturation voltage was an average of 14V for the tests, where the contact angle ceases to decrease, and the saturation angle was found to be an average of 83 degrees for the tests. The thickness of the CYTOP (1 spin coat application of 1%) is found to be an average of 50.8 nm from the electrowetting curves capacitance per unit of area value of the entire dielectric layer.

2.4.1 Calculation of the CYTOP thickness from the Capacitance per unit Area

The capacitance per unit of area from the curves are found by assuming that the 10V contact angle agrees with the Lippmann-Young prediction of the contact angle. Then the capacitance per unit area (C) is backed out from the Lippmann-Young equation 1.4 –

$$C = \frac{2\sigma_{GL}\left(\cos(\theta_v) - \cos(\theta_0)\right)}{V^2} \tag{2.28}$$

Then the thickness of the CYTOP is found by backing it out of the capacitance per unit area calculation of the entire layer –

$$C = \left(\frac{1}{C_{\mathrm{CYTOP}}} + \frac{1}{C_{\mathrm{Al_2O_3}}}\right)^{-1} \tag{2.29}$$

where the aluminum oxide and CYTOP layers act as capacitors in series. Their individual capacitance per unit areas may be written as:

$$C_{\mathrm{Al_2O_3}} = \frac{\varepsilon_o \varepsilon_{r_{\mathrm{Al_2O_3}}}}{t_{\mathrm{Al_2O_3}}} \;\; \& \tag{2.30}$$

$$C_{CYTOP} = \frac{\varepsilon_o \varepsilon_{r_{\mathrm{CYTOP}}}}{t_{\mathrm{CYTOP}}} \tag{2.31}$$

respectively. $\varepsilon_{r_{\mathrm{Al_2O_3}}}$ and $\varepsilon_{r_{\mathrm{CYTOP}}}$ are the respective relative permittivity's of Aluminum Oxide and CYTOP, $t_{\mathrm{Al_2O_3}}$ and t_{CYTOP} are the respective layer thicknesses, and ε_0 is the absolute permittivity. Thus, the capacitance per unit area of the CYTOP may be used to find the thickness of the CYTOP layer –

$$C_{\mathrm{CYTOP}} = \frac{C_{\mathrm{Al_2O_3}} C}{C_{\mathrm{Al_2O_3}} - C} \;\; \& \tag{2.32}$$

$$t_{\mathrm{CYTOP}} = \frac{\varepsilon_o \varepsilon_{r\mathrm{CYTOP}}}{C_{\mathrm{CYTOP}}} = \frac{\varepsilon_o \varepsilon_{r\mathrm{CYTOP}} \left(C_{\mathrm{Al_2O_3}} - C\right)}{C_{\mathrm{Al_2O_3}} C} \tag{2.33}$$

2.5 Additional Design Parameters

2.5.1 Young's Modulus of PDMS

The Young's modulus of Polydimethylsiloxane (PDMS) is generally between the values of ∼1.1 MPa and 1.5MPa [64–68], while the Poisson's ratio is 0.5. To accurately predict the maximum deflection a more accurate value of Young's modulus is required. The Young's modulus of PDMS is dependent on curing temperature and length of curing, and is membrane thickness dependent. The Young's modulus of PDMS will increase with increased curing temperatures and curing times. As most studies of the material properties PDMS are performed on bulk PDMS, we decided to use the Young's Modulus study of Liu et al. which focused on the material properties of thin film PDMS. Liu et al. found that thin film PDMS transitions from bulk PDMS at a thickness of 200 µm [64]. Fitting a polynomial curve to Liu et al.'s data allows for more accurate prediction of the CFAM's elastomeric membrane. Figure 2.9 shows Liu et al.'s data fit with the polynomial curve:

$$E = 1.201\text{x}10^{14} t_m^2 - 2.017\text{x}10^{10} t_m + 1.897\text{x}10^{6}. \tag{2.34}$$

The Young's modulus of this studies' PDMS membranes are 1.48 to 1.19 MPa, corresponding to a membrane thickness of 24 µm and 50 µm respectively. The Young's modulus increases with decrease in membrane thickness, it is proposed that the spin coating thin PDMS films allows for the organization of the typically random polymer chains in PDMS [64].

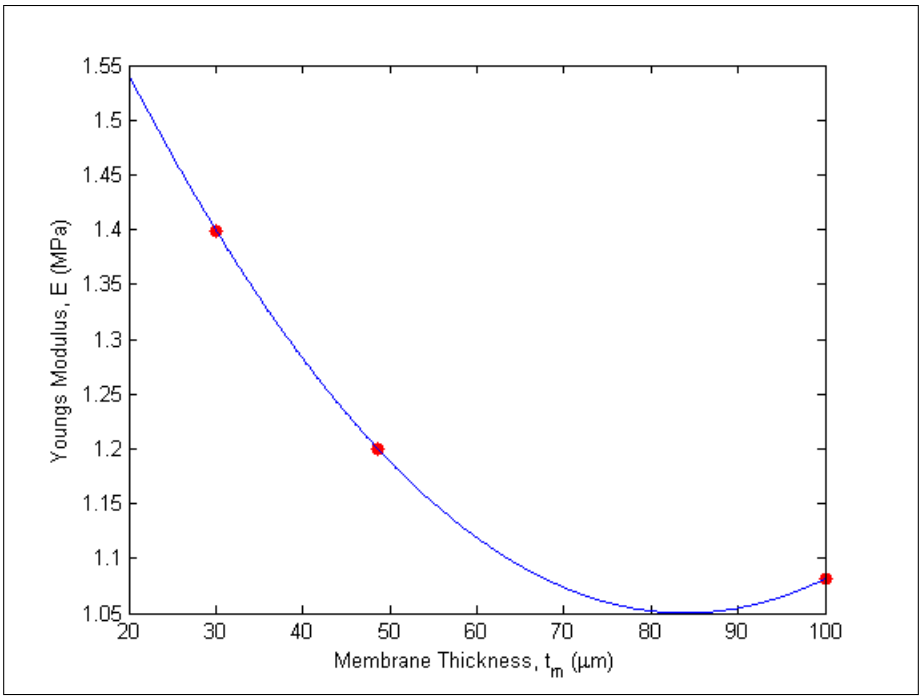

Figure 2.9: Young's Modulus Data fit with a polynomial curve. Data from Liu et al [64].

2.5.2 CFAM-SAS

The CFAM-SAS's passive surface includes a cut pinning ring. The pinning ring will prevent the drop shift of the conducting drop. The pinning rings are either 2.5 or 3.0 mm in diameter, and approximately 20 µm deep. There is a10 ° opening in the pinning ring to ensure electrical connection to the conducting drop. The CFAM-DAS device does not require pinning geometry because the third electrode effectively functions as pinning geometry.

Nezamoddini found that a capillary bridge pinned on the passive surface reduces the electrowetting force if there is an increase in volume [31]. However, the volume perturbations are so small, maximum of a 0.014 µL or 1.6% increase, that for the presented CFAM-SAS the effects are negligible. It was also found in experimental implementation that often times the drop would not fully pin on the passive surface, from minor variances in the bridge height upon assembly. It is assumed that the conducting drop is at least partially pinning in the CFAM-SAS cases, but the effects should be negligible in regards to volume perturbation

losses.

2.6 Device Design Plots

Using the governing equations 2.2 and 2.27, device parameter plots are presented to aid in future CFAM designs. Figures 2.10 and 2.11 provide the maximum displacement of the membrane given variations in membrane radius and membrane thickness at a bridge height of 50 and 100 µm. The pressure changes correspond the electrowetting surface of the CFAM-DAS device, and the angle change is from 103 to 83°. The capillary radius is fixed at 2mm. The plots show that a large range of deflections are achievable over a large range of membrane parameters. It also indicates that membrane radius has a larger effect on the membrane displacement than the membrane thickness. The design plots do not display deflection values greater than 3 times the membrane thickness – in accordance with large deflection theory.

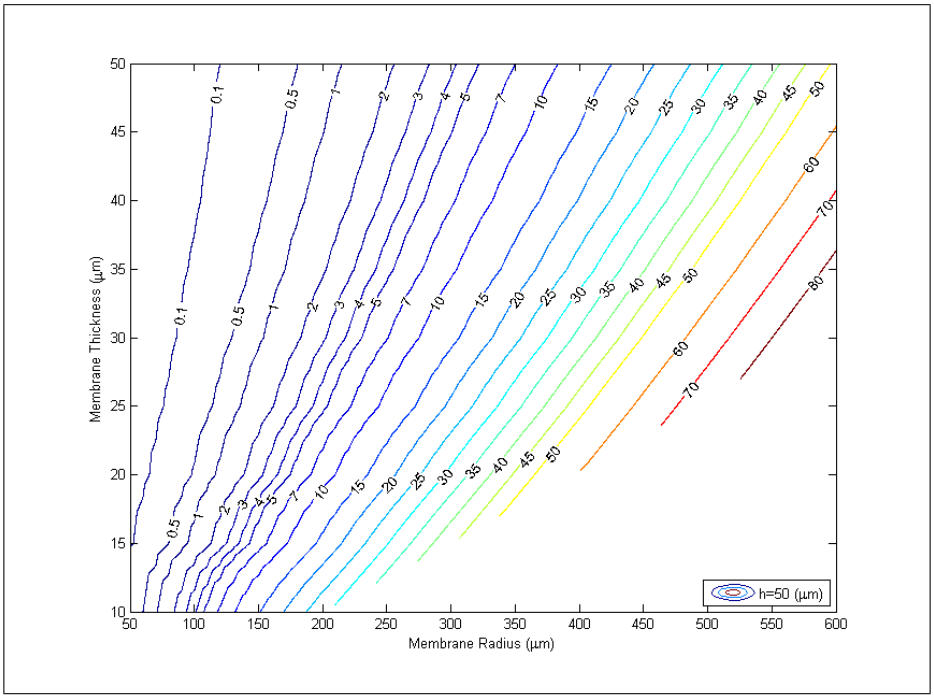

Figure 2.10: CFAM deflection design plot, predicted deflections for membrane thickness vs. membrane radius at a bridge height of 50 microns.

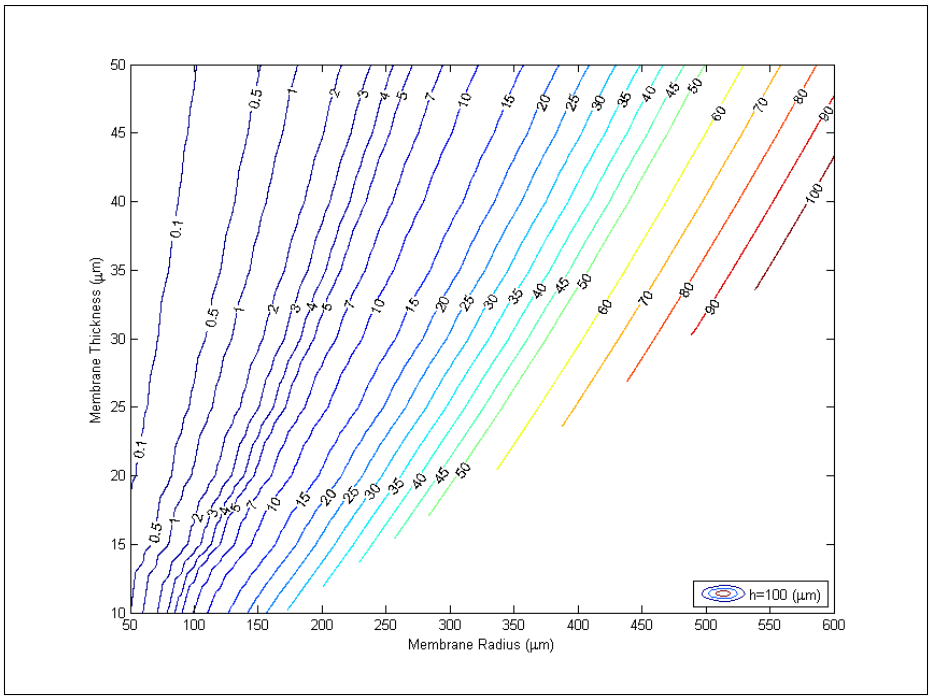

Figure 2.11: CFAM deflection design plot, predicted deflections for membrane thickness vs. membrane radius at a bridge height of 100 microns.

Figures 2.12 & 2.13 show the effect of bridge height versus membrane radius at set membrane thicknesses of 35 and 45 µm. A reduction in membrane radius reduces the membrane deflection greatly, however large deflections may be achieved at small bridge heights.

Figures 2.14 & 2.15 show the effects of bridge height versus membrane thickness on the membrane deflection at set membrane radii of 350 and 450 µm. A reduction in membrane thickness increases the membrane deflection, but the affect is not as strong as membrane radius on the membrane deflection.

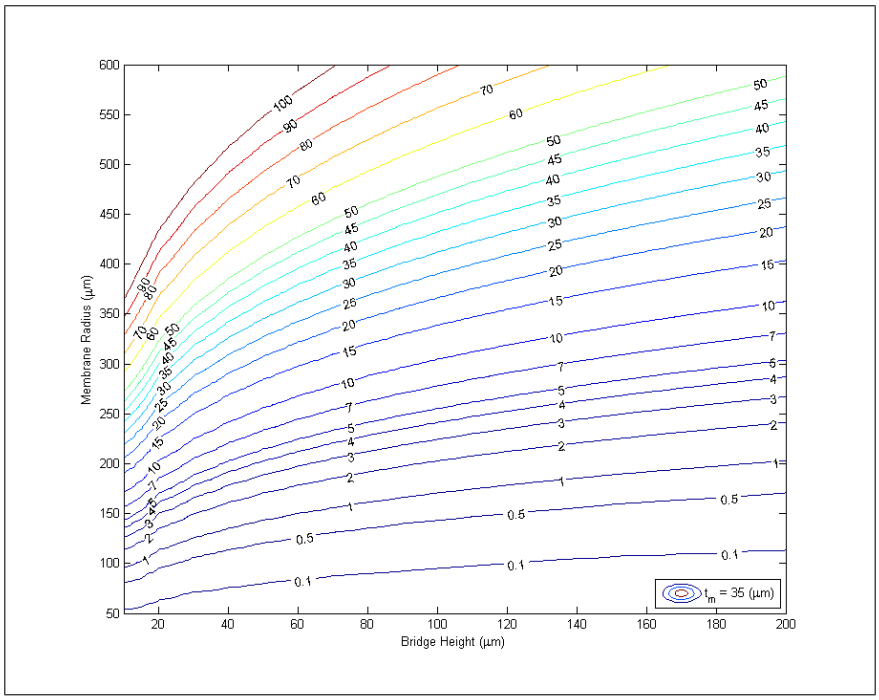

Figure 2.12: CFAM deflection design plot, predicted deflections for membrane radius vs.bridge height at a membrane thickness of 35 microns.

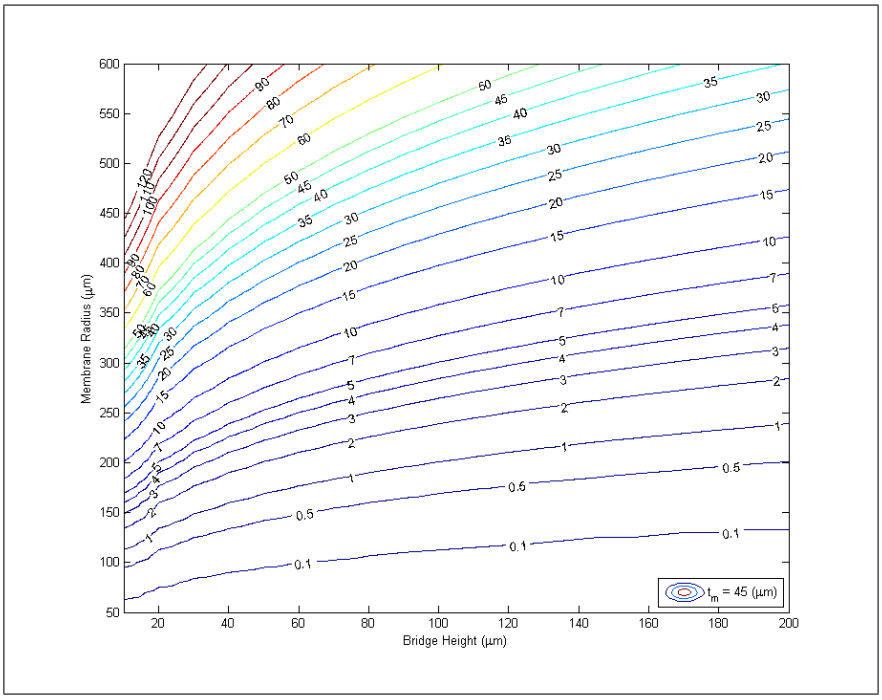

Figure 2.13: CFAM deflection design plot, predicted deflections for membrane radius vs. bridge height at a membrane thickness of 45 microns.

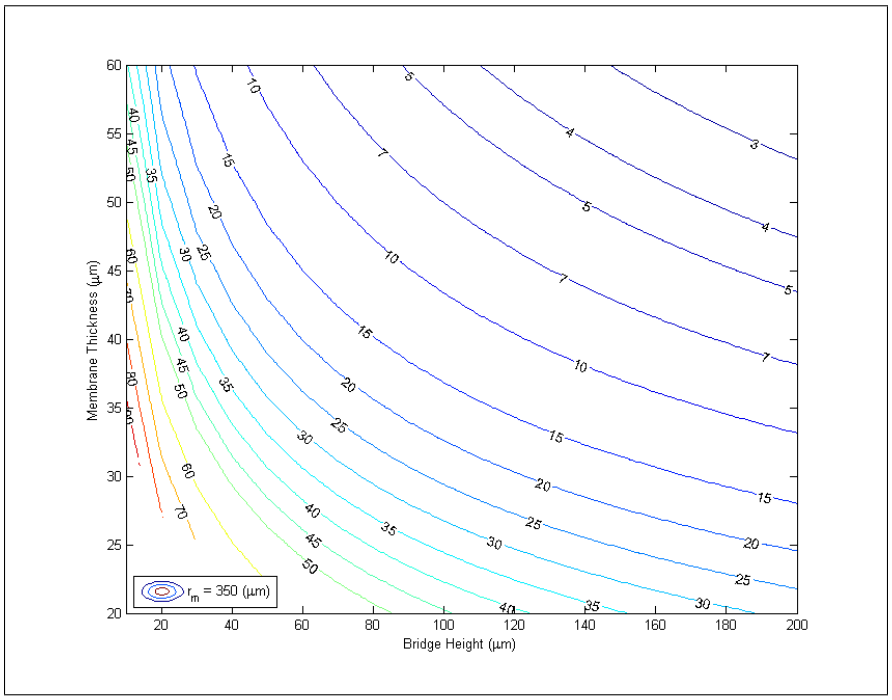

Figure 2.14: CFAM deflection design plot, predicted deflections for membrane thickness vs. bridge height at a membrane radius of 350 microns.

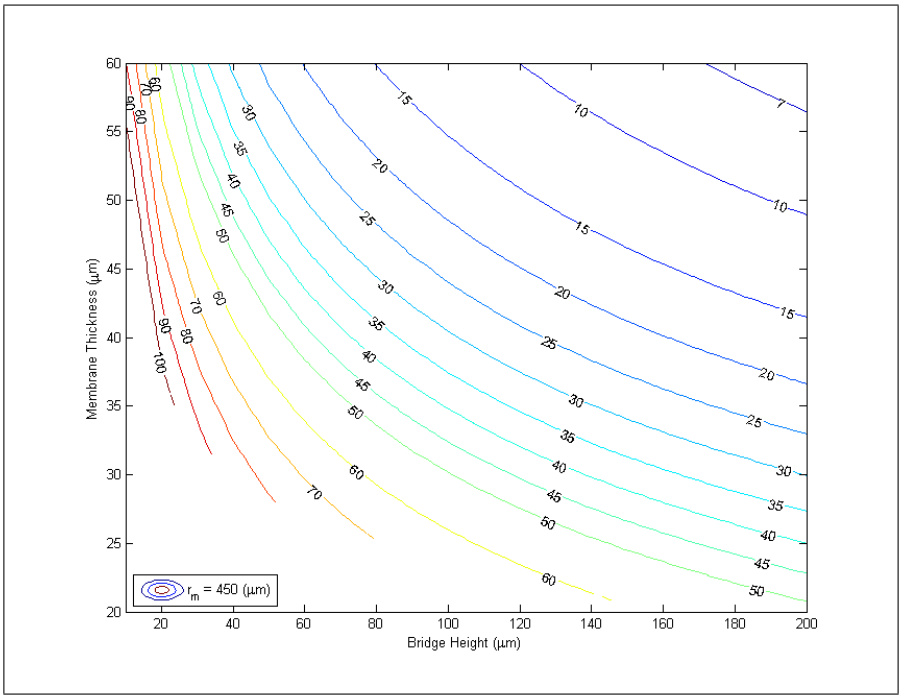

Figure 2.15: CFAM deflection design plot, predicted deflections for membrane thickness vs bridge height at a membrane radius of 450 microns.

Chapter 3

Fabrication and Testing of CFAM Devices

This chapter describes the fabrication process of the CFAM prototypes, and provides an overview of the testing equipment and experimental set up. Figure 3.1a gives a side view of the dual active surface CFAM device (CFAM-DAS), and Figure 3.1b gives a side view of the single active surface CFAM device (CFAM-SAS).

The dual active surface CFAM prototype is composed of a conducting aqueous droplet in contact with three electrodes on two surfaces. The single active surface CFAM prototype is composed of a conducting aqueous droplet in contact with two electrodes on two surfaces. In both prototypes, the lower surface has a single dielectric covered electrode which forms an active (i.e. electrowetting) surface, this will be called the bottom plate. Bottom plate fabrication will be detailed in Section 3.1. The upper surface for CFAM-DAS prototypes consist of two glass slides, each with an electrode – one electrode covered in a dielectric layer (the second active surface), the other uncovered. The two slides form the CFAM-DAS top plate; fabrication will be detailed in Section 3.2. The upper surface of the CFAM-SAS prototype consists of a single glass slide, with an uncovered electrode which forms a passive (i.e. non-electrowetting) surface. The single slide forms the CFAM-SAS top plate;

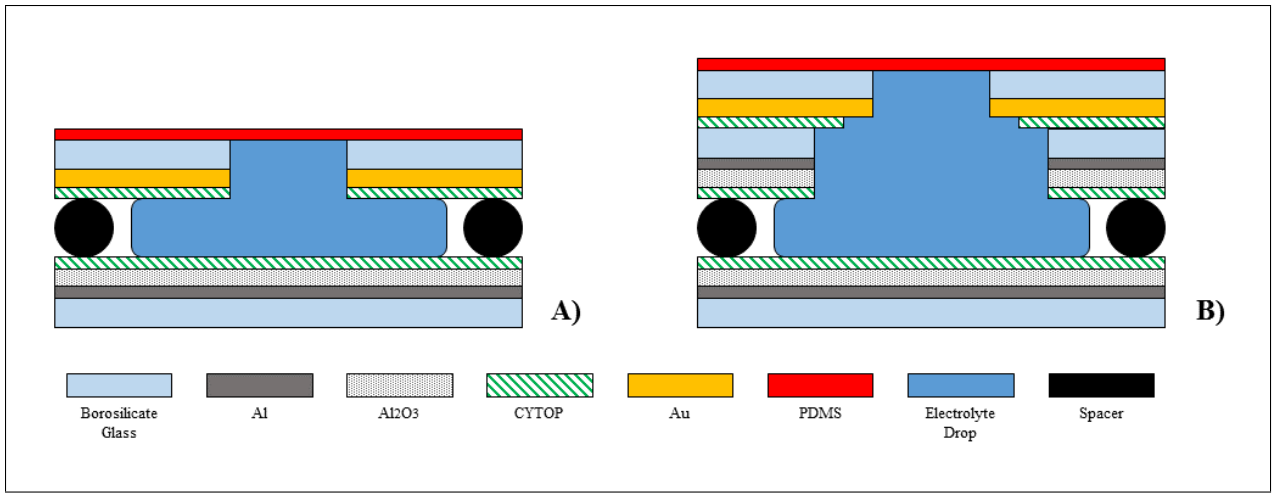

Figure 3.1: A) Side view of CFAM-SAS Device. B) Side view of CFAM-DAS Device.

fabrication will be detailed in Section 3.3. The top and bottom plates of respective prototypes are assembled to form the completed respective devices, detailed in Section 3.4. Fabrication of the polydimethylsiloxane (PDMS) elastomeric membrane is detailed in Section 3.5, and experimental set up is detailed in Section 3.6.

3.1 Fabrication of the Bottom Plate

This section provides an overview of the fabrication of the bottom plate for both CFAM-DAS and CFAM-SAS prototypes. A step-by-step fabrication sheet is located in Appendix A. Figure 3.2 gives an overview of the major fabrication steps.

A 3.81cm x 7.62cm x 0.1599cm (1.5" x 3" x 1/16") soda-lime glass slide was used as the base for the lower active surface. Some of the glass slides were cut in half prior to fabrication to increase fabrication output and minimize waste. A 100 nanometer (nm) thick Aluminum (Al) metal layer was deposited by e-beam evaporation (CHA Industries, Fremont, CA) onto the glass slide. An aluminum oxide (Al_2O_3) layer was grown via aluminum anodization using the procedure of Mibus et al [69]. The oxide forms the dielectric layer required for electrowetting. Aluminum anodization was performed using a two electrode electrochemical

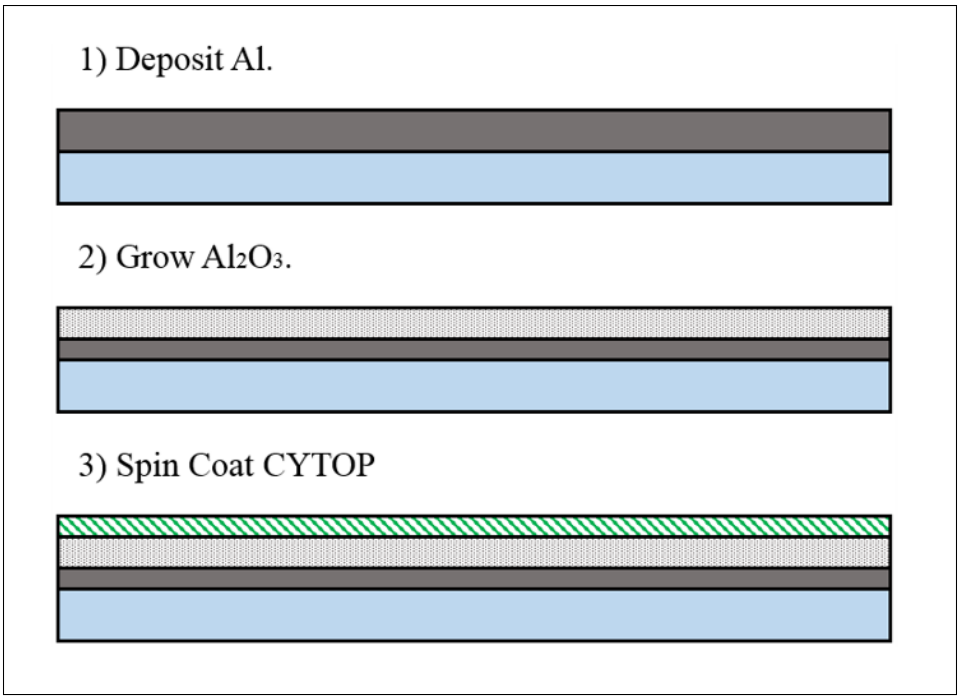

Figure 3.2: Major fabrication steps of CFAM bottom plate.

cell with the electrodes in a vertical configuration, using a platinum mesh counter electrode. The anodization solution is 30 wt. % ammonium pentaborate ($NH_4B_5O_8$) in 99.99% ethylene glycol at room temperature. Al_2O_3 thickness varies as a linear function of anodization voltage, approximately:

$$t_{Al_2O_3} = 1.2V_a + 9 \tag{3.1}$$

where $t_{Al_2O_3}$ is the resulting Al_2O_3 thickness in nm, and V_a is the anodization voltage [69]. The layer was allowed to anodize for 8 minutes. The oxide thicknesses for were 45nm (30V) and 30.6nm (18V) for CFAM-SAS and CFAM-DAS respectively.

It should be noted that one edge of the Al layer will not grow Al_2O_3 during the anodization due to the procedure employed. An electrical connection to the Al layer is require to allow the application of the anodization voltage, if this connection is exposed to the anodization solution it too will oxidize, cutting off the current and preventing complete anodization of the Al_2O_3 layer. Therefore, the connection must be protected from the anodization solution with Kaptan tape, leaving a patch of pure Al on the surface after the anodization. This

un-anodized edge of Al was used to make future electrical connections to the plate.

The Al_2O_3 was then covered, via spin coating, with an ultrathin film of hydrophobic fluoropolymer, CYTOP-809 (Bellex International Corporation). The CYTOP and its solvent were mixed by weight to vary the thickness of the CYTOP layer between approximately 50 nm and 60nm. The mixtures were 0.5% wt., 1% wt., and 2% wt.. The CYTOP was spun onto the oxide at 2000 RPM for 30 seconds, then the slides were baked at 160° for 1 hour on a hot plate.

In some configurations 2-3 spin coat applications of CYTOP were applied to create a thicker layer, such as 2 spin coat applications of 2.0% wt. CYTOP to create an approximate thickness of 60nm. Appendix A provides the multi-spin fabrication process.

The CFAM-DAS prototype samples all had the same CYTOP recipe: 1 spin coat application of 1% wt. CYTOP. The resulting thickness was 50.8nm as determined from goniometer contact angle analysis, see Section 2.4.1.

While the majority of the test articles utilized the same spin recipe, other recipes used were (I) 3 spins of 0.5% (E-SAS and P-SAS); and (II) 2 spins of 2% (C-SAS, C-SAS, F-SAS, N-SAS and O-SAS). These recipes will result in slightly thicker CYTOP layers than the standard 1 spin coat application of 1

To complete the bottom plates a mixture silicon oil (Dow Corning OS-10, OS-20, and OS-30; 1:8:1 by weight), was applied to the CYTOP then allowed to evaporate off the surface. The oil treatment lowered wetting hysteresis on the CYTOP surface [39, 43]. Contact angle hysteresis is the difference between the advancing and receding contact angles; lower values correspond to more repeatable wetting behavior. With the materials used contact angle hysteresis was typically about 10°, but contamination may increase contact angle hysteresis in a test. The electrical connection to the slide was made via copper tape (Ted Pella, INC). The tape wass applied to the edge of the slide where CYTOP has been removed by scratching with tweezers. The electrical connection was checked with a multimeter.

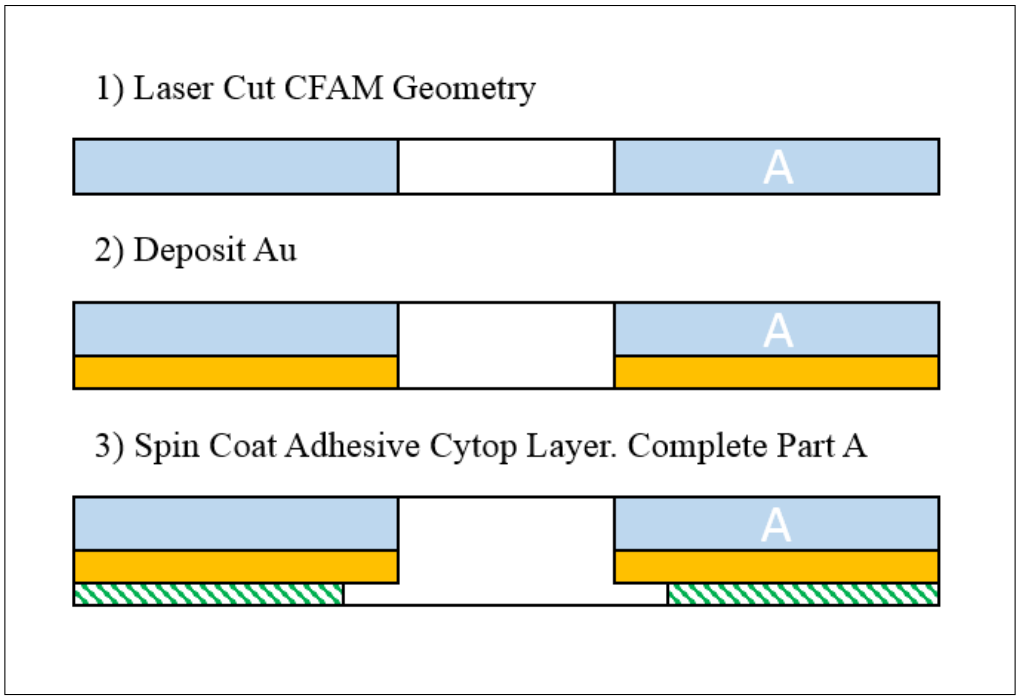

Figure 3.3: Major fabrication steps of CFAM-DAS top plate Part A.

3.2 Fabrication of the CFAM-DAS Top Plate

The top plate of the CFAM-DAS was composed of 2 glass slides, each with an electrode – one electrode covered in a dielectric layer (the second active surface), the other uncovered. The slide with the uncovered electrode is referred to as Part A, while the slide with the active surface on the electrode is referred to as Part B. This section provides an overview of the fabrication of the CFAM-DAS top plate, a step-by-step procedure is located in Appendix B.

3.2.1 Top plate Part A fabrication

Part A of the top plate was fabricated with a borosilicate glass slide, 22mm x 22mm x 0.012mm (120 µm). Figure 3.3 shows the major fabrication steps of Part A. The device geometry was cut into the glass slide via VersaLASER VLS3.50, 50W CO_2 laser cutter; informative laser cutting procedures may be found in Thompson et al. [70]. Prior to performing the cut, Scotch tape was placed on each face of the glass slide to prevent the adhesion of

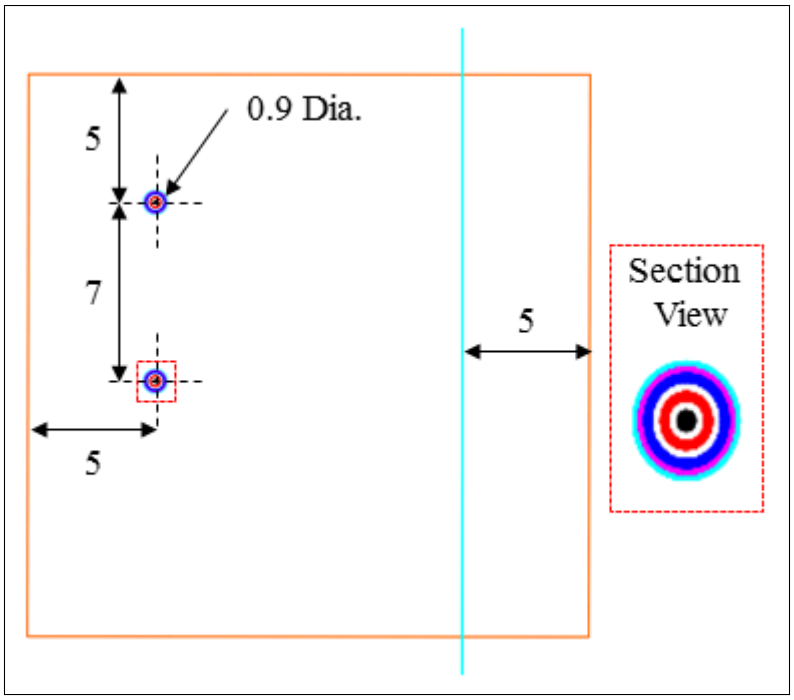

Figure 3.4: Laser cutter input for CFAM-DAS top plate Part A. Note: Dimensions are in mm, and the orange square is for laser alignment.

ejected heated material to the surface of the glass.

Figure 3.4 shows the laser cutter input with added dimensions for the Part A. Two holes were cut into the bottom of the glass slide; this allows for the fabrication of two devices on a single plate. The holes will eventually define the membrane radius of the elastomeric membrane. The laser cutting created a slightly tapered hole where the upper diameter (cut into the bottom of the slide) would be approximately 100 µm larger than the lower diameter (through cut to the top of the slide). The smaller hole must be employed as the top of the slide to prevent air pockets from forming when a drop was loaded during device assembly. The through cut holes were cut via increasing concentric circles until the maximum diameter was achieved; this procedure was found to be the optimal method for producing smooth holes without fractures. The diameters of the concentric circles are listed in Table 3.1. The through cut line shortened the plate to allow for electrical connection to Part B without a short-circuit to Part A. Note the varied colors of Figure 3.4, the laser cutter used

color definitions to set different laser powers, laser speeds, and cut orders. For example, the orange square border was assigned a power setting of 0%, i.e. no cut, since it was only used for pre-cut alignment purposes during the laser cutter procedure.

Table 3.1: Laser cutter inputs for CFAM-DAS top plate Part A with a nominal dia. of 1000 µm.

Feature	Color	Dimension. (mm)	Laser Power (%)	Laser Speed (%)	# of Passes
Circle	Black	0.1 Dia.	24	31	5
Circle	Red	0.4 Dia.	24	31	7
Circle	Blue	0.7 Dia.	24	31	8
Circle	Magenta	0.8 Dia.	24	31	7
Circle	Cyan	0.9 Dia.	24	31	7
Line	Cyan	25 x 0	24	31	5
Square	Orange	22 x 22	0	N/A	0

Note, the orange square is an alignment feature. The cyan line is over sized to ensure a through cut.

The laser power and speed were optimized to be 24% and 31%, respectively. The number of laser passes required for through cut varied by feature: a through cut line required five passes, the inner most concentric circles required five passes, and the remaining concentric circles required seven passes - with the exception 0.7mm diameter concentric circle requiring 8 passes. Table 3.1 give a summarized view of the cutting parameters. Note, the presented image and table is for the nominal membrane diameter of 1000 microns; parameters for 800 and 600 micron designs are presented in Appendix A.3. Additionally, while laser performance was largely repeatable, there was some variation in the final dimensions that resulted. Thus, the cut dimensions were measured via optical methods (Zeiss Microscope).

Due the fragile nature of the thin glass slide, the tape removal must be chemically assisted. Scotch tape has a pressure sensitive adhesive coated onto a plastic backing. The slides were soaked in D'limonene solvent to dissolve the majority of the adhesive, then the plastic backing was removed easily with tweezers. Areas directly adjacent to the laser cut geometry had residual super-heated adhesive that was not removed by the D'limonene, this was removed via a Trichloroethylene (TCE) soaked swab. The top of the glass slide was then bladed with

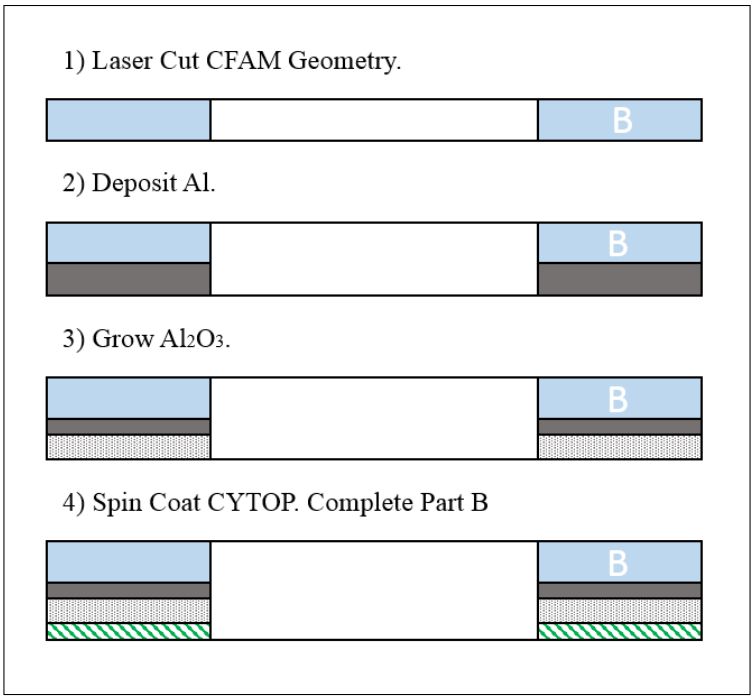

Figure 3.5: Major fabrication steps of CFAM-DAS top plate Part B.

a razor blade to remove a small build up (10-20 µm) of ejected heated glass on the rim of the cut geometry that was not prevented by the scotch tape; this was done to allow the elastomeric membrane to lie flat over the hole once it was placed. Blading was not required on the bottom of Part A. Then, a 10 nm thick layer of Gold (Au) was deposited on to the bottom of the slides by e-beam evaporation, utilizing a 2.5 nm Titanium adhesion layer, to form the uncovered electrode. Last, black wax dissolved in TCE was applied into and directly adjacent to the hole on the Au layer with a toothpick. The black wax masked the Au from the adhesive during the bonding of Parts A and B.

3.2.2 Part B fabrication

Part B of the top plate was fabricated from a borosilicate glass slide, 22mm x 22mm x 0.012mm (120 µm). Figure 3.5 shows the major fabrication steps. The device geometry was cut into the glass slide via CO_2 laser cutter, after the slide faces were protected with pressure sensitive scotch tape. Figure 3.6 shows the laser cutter input with added dimensions for Part

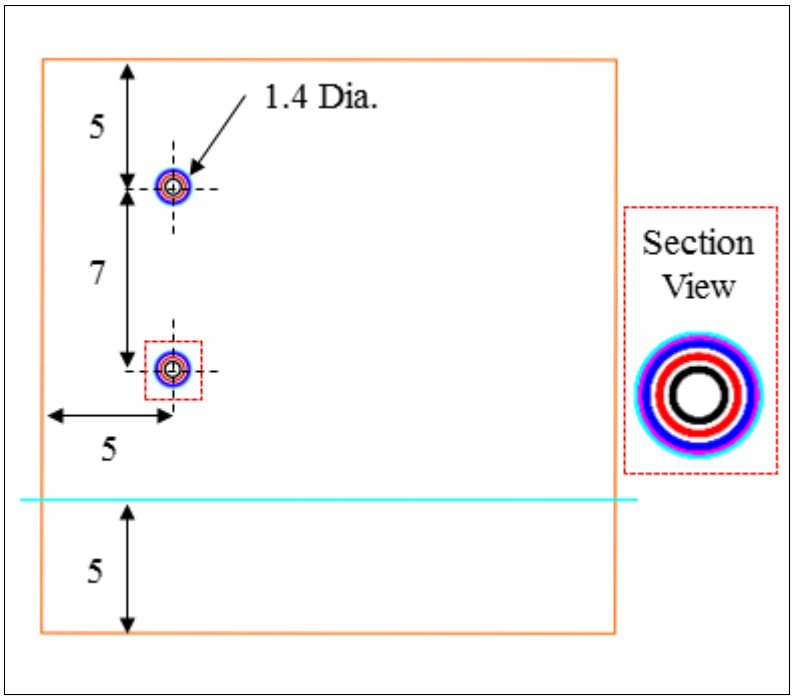

Figure 3.6: Laser cutter input for CFAM-DAS top plate Part B. Note: Dimensions are in mm, and the orange square is for laser alignment.

B. The laser settings were identical to the Part A fabrication. Table 3.2 gives a summary of the cutting parameters. Two holes were made into the bottom of the Part B glass slide, the holes were concentric with the through cut holes on Part A, and allowed the electrolyte to make contact with the uncovered electrode on Part A. The through cut line narrowed the plate to allow for electrical connection to Part A without a short-circuit to Part B.

The pressure sensitive scotch tape removal process was identical to that used for Part A. Then, the top of the glass slide was bladed with a razor blade to remove small build up (10-20 µm) of ejected heated glass on the rim of the cut geometry; this was done to allow optimal contact between Parts A and B once they were bonded. Blading was not required on the bottom of Part B.

The active surface was fabricated to be identical to the active surface on the bottom plate, presented in Section 3.1. A 100 nm thick layer of Al was deposited onto the bottom of the slide by e-beam evaporation. A 30.6 nm (18V) Al_2O_3 layer was grown via Al anodization

Table 3.2: Laser cutter input for CFAM-DAS top plate part B with a nominal dia. of 1500 µm.

Feature	Color	Dimension. (mm)	Laser Power (%)	Laser Speed (%)	# of Passes
Circle	Black	0.6 Dia.	24	31	5
Circle	Red	0.9 Dia.	24	31	7
Circle	Blue	1.2 Dia.	24	31	8
Circle	Magenta	1.3 Dia.	24	31	7
Circle	Cyan	1.4 Dia.	24	31	7
Line	Cyan	25 x 0	24	31	5
Square	Orange	22 x 22	0	N/A	0

Note, the orange square is an alignment feature. The cyan line is over sized to ensure a through cut.

using the procedure presented in section 3.1. The anodization electrical connection was made at the bottom edge of the Part B Al layer.

Then, a 100nm thick Titanium layer was deposited onto the lower portion of the bottom of Part B via e-beam evaporation (the location of the un-anodized Al). The Al_2O_3 was protected via aluminum foil shadow mask. The titanium layer was required due to the reactivity of the gallium-indium (GaI) liquid (used for top plate electrical connections) with aluminum. Last, the aluminum oxide was covered via spin-coating with an ultrathin film of hydrophobic fluoropolymer, CYTOP-809. The CYTOP on Part B was 1 spin coat application of 1% wt. CYTOP, applied at 2000 RPM for 30 seconds. The CYTOP was removed from the Ti layer via swab to allow for electrical connection. The CYTOP was then cured with a hot plate at 160° C for 1 hour. This completes Part B's fabrication.

3.2.3 Top Plate assembly process

Figure 3.7 provides a side view of the assembly process while Figure 3.8 provides a bottom view. Note that during fabrication the bottom surface would be upward facing so as not to damage the active surface on Part B. To bond completed Parts A and B together, a thick layer of CYTOP (8% wt.) was spun onto the bottom (Au side) of Part A at 2000 RPM for

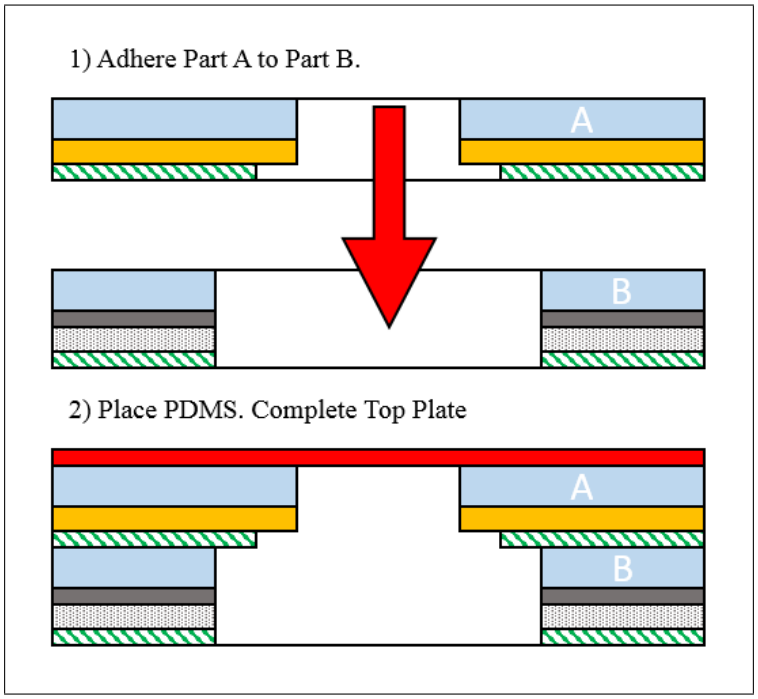

Figure 3.7: Side view of CFAM-DAS top plate part A and part B assembly process.

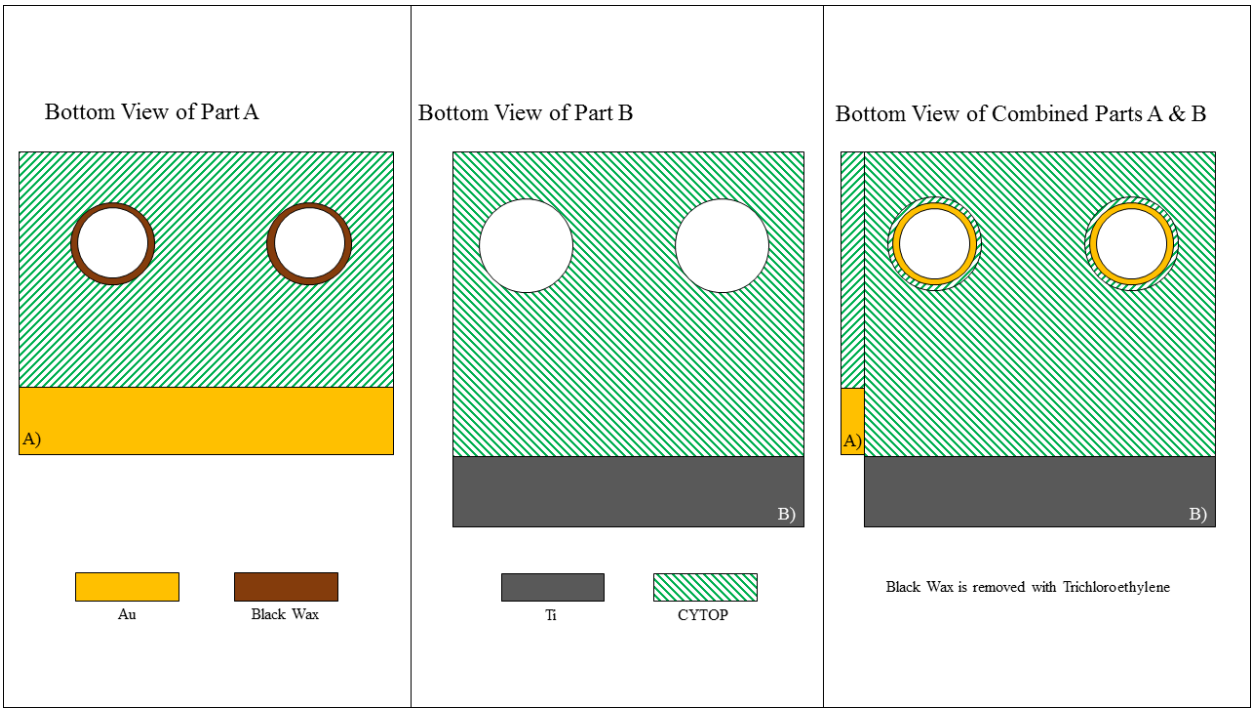

Figure 3.8: Bottom view of CFAM-DAS top plate Part A and Part B assembly process, prior to PDMS application.

30 seconds. Part B was optically aligned with Part A, with Part B's bottom (active side) facing upwards, and then Part B was pressed onto the CYTOP on Part A. This formed the combined top plate. Excess CYTOP was removed from the exposed edge of the Au on Part A via a swab, to allow for electrical connection. Then the combined plated was baked on a hot plate at 160 ° C for 1 hour to cure the CYTOP, permanently bonding the Parts A and B. Last, the protective black wax was removed on top of the Au electrode with TCE.

To complete the top plate fabrication, the CYTOP layer was treated with silicon oil to reduce the hysteresis on the passive surface. A PDMS piece of desired thickness was then selected and applied on the top of the top plate, covering the through hole and forming the elastomeric membrane. The PDMS was placed such that the reflective spot was centered within the hole. It was found that PDMS naturally adhered to the glass with suitable strength and did not require any additional treatment (e.g. oxygen plasma bonding). PDMS fabrication is discussed in Section 3.5. MetGlas, a thin amorphous ferromagnetic metal, was cut to size and secured to the top of the top plate with Scotch tape. Electrical connections were made to the bottom of the top plate from the top by carefully painting GaI over the edge of the plate, ensuring there were no breaks. Then, a piece of 25 µm diameter copper or Au wire was taped to the top plate, both methods contacted the painted GaI. The electrical connections were checked with a multimeter.

Plastic microbeads (nominally 45 or 100 µm, ± 10 µm) were applied to the bottom surface of the top plate as spacers for the final assembly. The deposited beads were inspected under a microscope to ensure that a single layer resulted. Figure 3.9 shows a top and bottom view of the completed top plate.

3.3 Fabrication of the Top Plate for CFAM-SAS

The top plate of the CFAM-SAS was composed of one glass slide, with one uncovered electrode (the passive surface). This section provides an overview of the fabrication of the

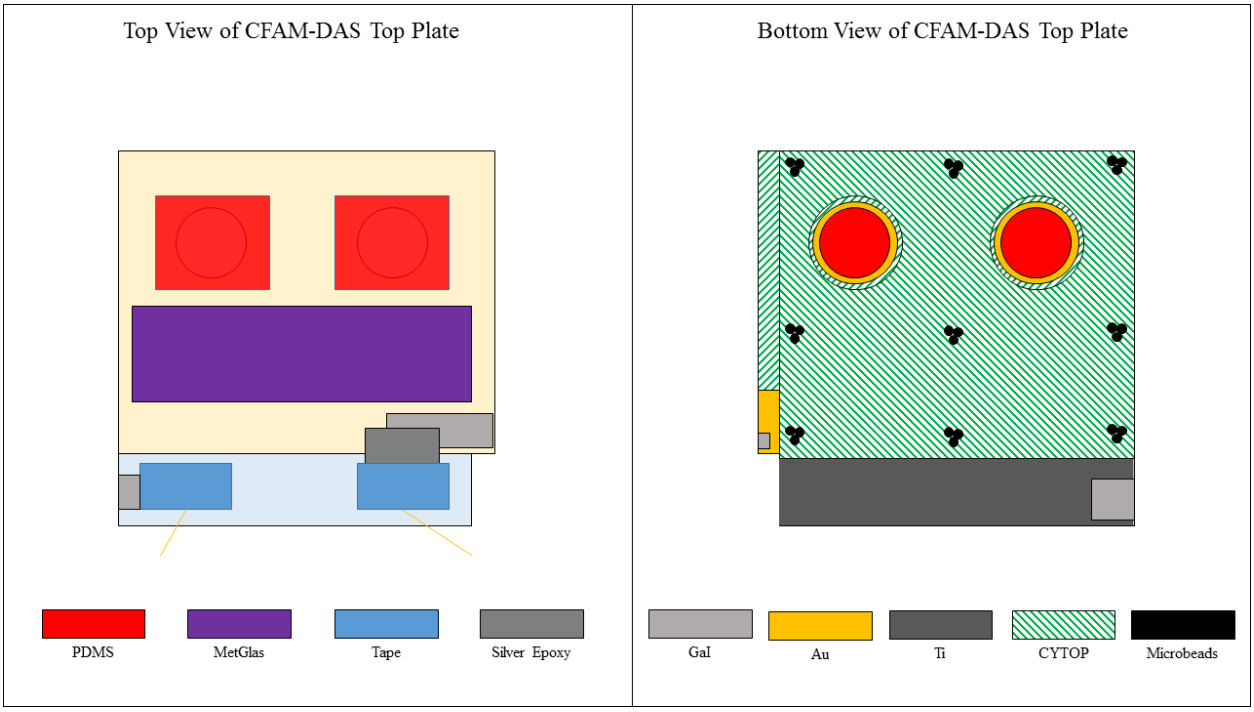

Figure 3.9: Top and Bottom view of completed CFAM-DAS top plate.

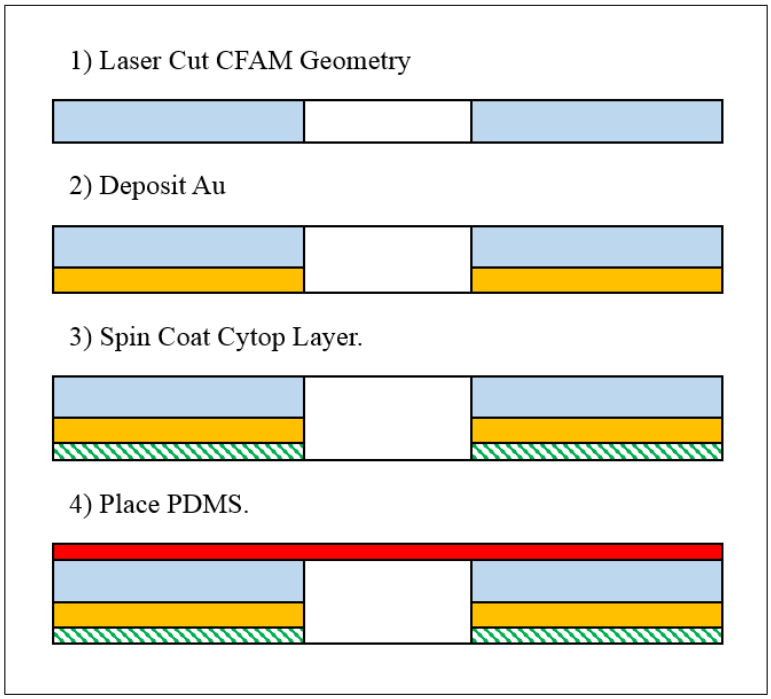

Figure 3.10: Major fabrication steps of CFAM-SAS top plate.

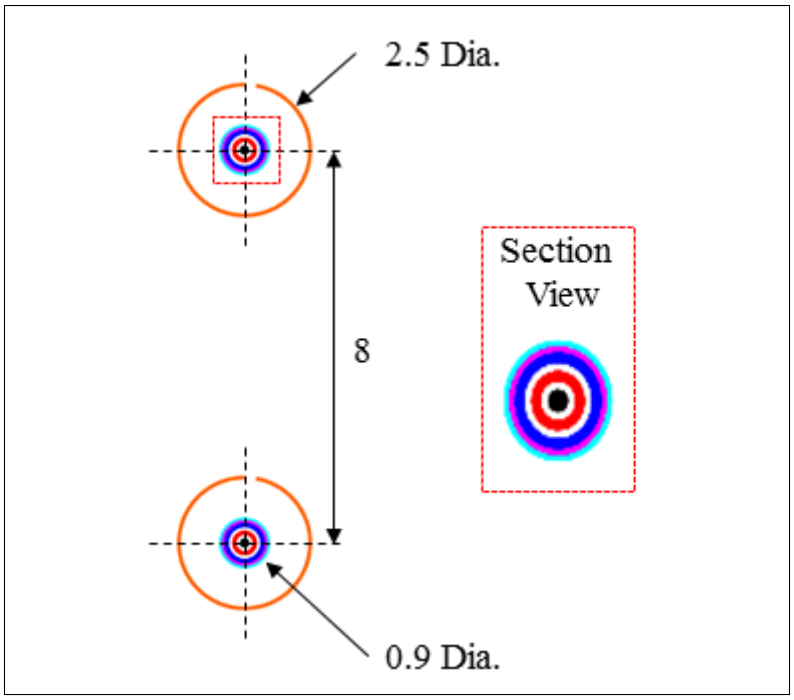

Figure 3.11: Laser cutter input for CFAM-SAS. Note: Dimensions are in mm.

CFAM-SAS top plate; a step-by-step procedure is located in Appendix D. See Figure 3.10 for major fabrication steps.

The top plate was fabricated from a borosilicate glass slide, 22mm x 22mm x 0.012mm (120 µm). The device geometry was cut into the glass slide via VersaLASER VLS3.50 50W CO_2 laser cutter. Prior to performing the cut, PDMS sheets (∼50-100 µm thick) were placed on each face of the glass slide to prevent the adhesion of ejected heated material to the surface of the glass. PDMS was not as an effective protective layer as pressure-sensitive Scotch tape, but it was found to sufficient for the passive surface where active wetting was not occurring.

The laser settings were identical to the laser cut fabrication procedure for the top plate of CFAM-DAS (Section 3.2). Figure 3.11 shows the laser cutter input with added dimensions for the top plate, and Table 3.3 provides a summary of the laser cutting parameters. Two holes were cut into the bottom of the glass slide. These holes would eventually define the membrane radius of the elastomeric membrane. A single large circular C-shape with a 10° opening was cut concentric to the hole. The cut was only repeated once to prevent

through cutting, and the opening in the C-shape was provided to ensure electrical connection from the outside region to the shape's interior so as to make contact with the conducting drop. The slide was aligned manually since hole position was not critical for CFAM-SAS, thus the alignment aid seen in Section 3.2 (Figure 3.5 & 3.6) was not needed. Note, that the presented image is the final design and laser setting, earlier designs are presented in Appendix E. Changes to the design were caused by repairs to the laser cutter, which in turn changed the cutting properties – from 50 Watts to $\sim$ 30 Watts.

Table 3.3: Laser cutter inputs for CFAM-SAS top plate with a nominal dia. of 1000 µm.

Feature	Color	Dimension. (mm)	Laser Power (%)	Laser Speed (%)	# of Passes
Circle	Black	0.1 Dia.	24	31	5
Circle	Red	0.4 Dia.	24	31	7
Circle	Blue	0.7 Dia.	24	31	8
Circle	Magenta	0.8 Dia.	24	31	7
Circle	Cyan	0.9 Dia.	24	31	7
350° Arc	Orange	2.5 Dia.	13	35	1

After the laser cutting, the placed PDMS was removed, and the slides were cleaned with acetone, isopropyl alcohol and de-ionized water (DI). Then the top of the glass slide was bladed with a razor blade to remove small build up (10-20 µm) of ejected heated glass on the rim of the cut geometry; this was done to allow the elastomeric membrane to lie flat over the hole once it was placed. Blading was not required on the bottom of the glass slide. Then a 10 nm thick layer of Au was deposited on to the bottom of the slides by e-beam evaporation, utilizing a 2.5 nm Ti adhesion layer, forming the uncovered electrode. Last, a layer of CYTOP was spin coated onto the Au layer, to allow the eased motion of the conducting drop on the passive surface. The CYTOP layer was applied with one spin coat application of either 0.5% wt. or 1% wt. CYTOP, for 30 seconds at 2000 RPM then baked for 1 hour at 160° C. The thickness was unimportant for the operation of the top plate of CFAM-SAS because the CYTOP was not acting in a dielectric capacity, and the minimal

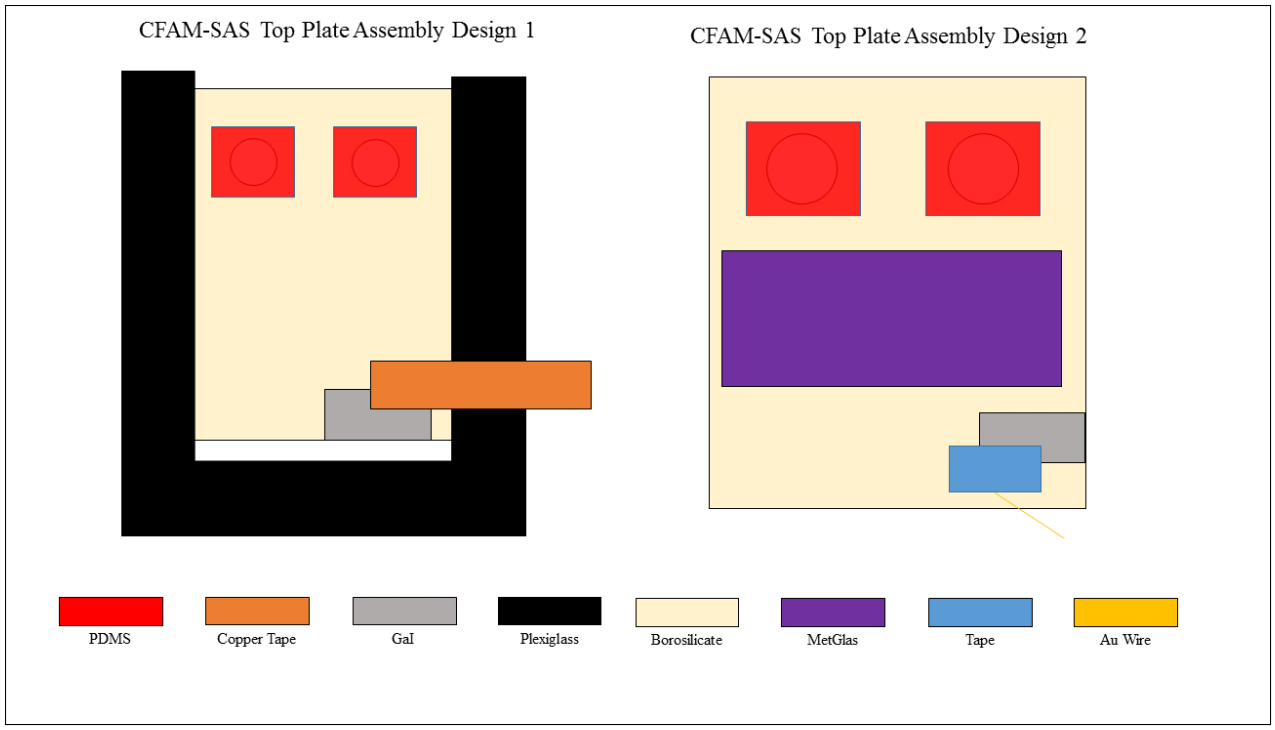

Figure 3.12: Design 1 and Design 2 of CFAM-SAS top plate assembly.

resistance did not affect the prototypes electrical performance.

To complete the top plate fabrication, the top plate's CYTOP layer was treated with silicon oil to reduce the Hysteresis on the passive surface. The desired PDMS piece was selected and applied on the top of the top plate over the hole with the reflective spot centered. This forms the elastomeric membrane. The membrane flatness was checked with a DekTAK Profilometer.

Then, based on the design iteration, either: (Version I) the top plate was secured to a Plexiglas holder via super glue; or (Version II) MetGlas was applied with Scotch tape to the top surface of the top plate. Figure 3.12 shows a schematic comparing the two design iterations.

Electrical connection was made to the bottom of the top plate from the top by carefully painting GaI over the edge of the plate, ensuring there were no breaks. Then, either a copper tape connection was made to the GaI on the top plate (Version I), or a 25 µm diameter copper

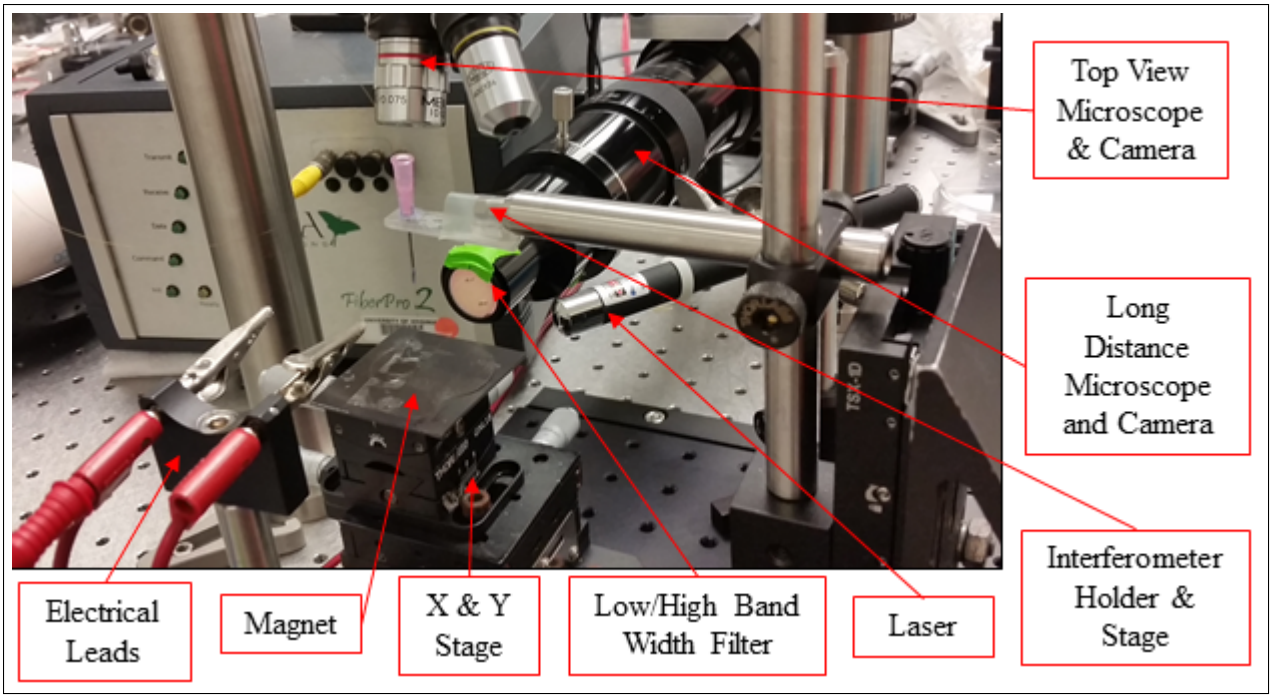

Figure 3.13: Experimental set up for testing the CFAM devices. XYZ Stage for CFAM-SAS Design 1 is not pictured, but would be in the proximity of the Electrical Leads.

or Au wire was taped to the GaI wetted surface (Version II). The electrical connection was checked with a multimeter. Plastic microbeads (45 or 100 µm) were applied to the bottom surface of the top plate as spacers for the final assembly.

3.4 CFAM-DAS and CFAM-SAS Prototype Assembly

A "flip chip" assembly process was used to assemble the top and bottom plates for both CFAM-SAS and CFAM-DAS. Figure 3.13 shows the experimental platform for CFAM prototypes. The prototype device was assembled after first depositing a droplet of an aqueous solution (0.1M Cs_2SO_4 in DI water with 10 µm Mol/L Fluorescein Salt) in the top plate hole beneath the membrane.

The top view camera was used to align the membrane in the field-of-view of the side view camera. For the CFAM-DAS and CFAM-SAS-Version II devices, the top plate was placed

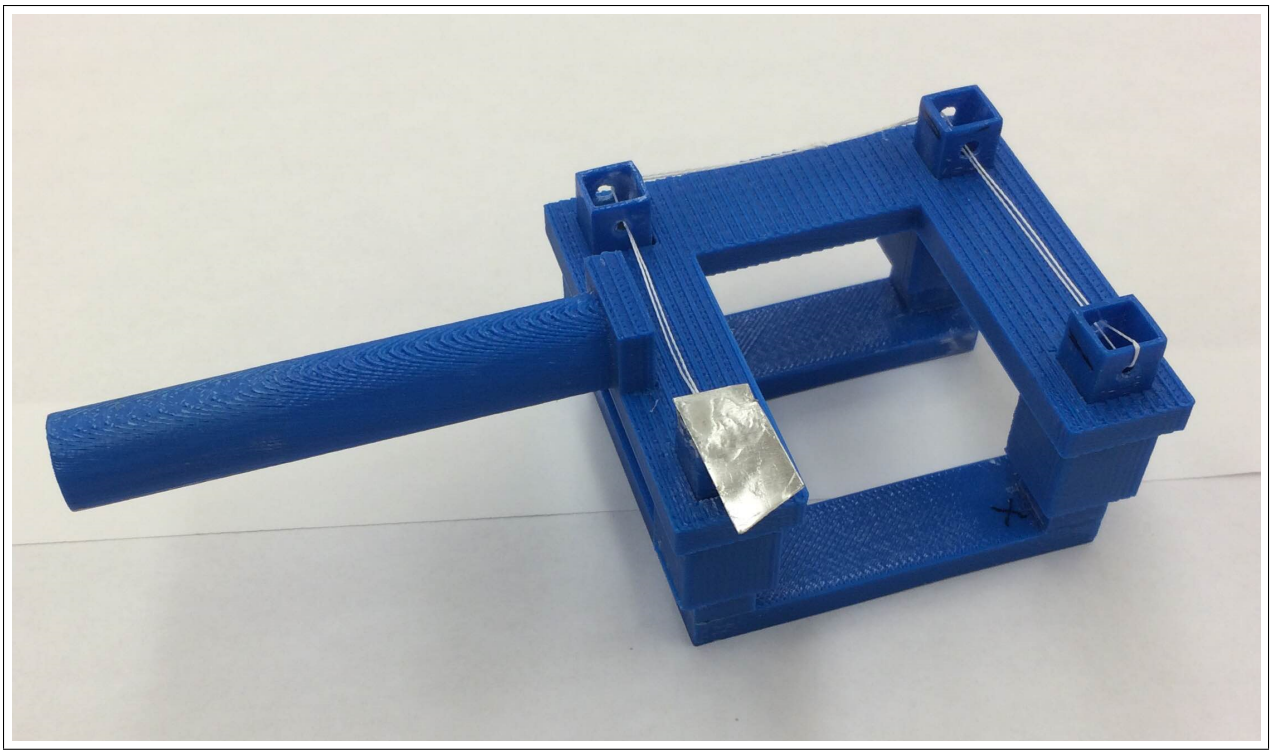

Figure 3.14: 3D printed holder that held CFAM-SAS Design 1 and connected to XYZ stage.

on to the bottom plate slowly with tweezers, then the assembly was moved into its final position via XY stage. The top plate was held in place by an attractive force applied to the MetGlas by a magnet underneath the bottom plate.

CFAM-SAS-Version I was secured to a secondary holder that was secured to the XYZ stage for final assembly (not pictured in 3.13). The secondary holder was 3D printed and incorporates two interlocking pieces, pictured in Figure 3.14. The top plate was secured to the lower piece, and the upper piece was secured to the stage. When the lower piece made contact with a surface the top piece may continue to translate downward; this ensured full contact of the bottom plate without damaging the top plate. Prior to full contact the top plate was positioned so the drop was in view of the side view camera via the XY stage, then the top plate was slowly lowered to the final position.

The interferometer fiber was positioned via XYZ stage over the reflective spot on the PDMS membrane. The illumination laser for achieving drop fluorescence was aimed at the

drop, and the side view camera was focused on the bridge profile.

3.5 PDMS Fabrication

Dow Corning (USA) PDMS was used to manufacture the elastomeric membrane. The PDMS kit contains a base polymer (part A) and a curing agent (part B). The two parts were mixed 10:1 by weight and allowed to degas in air for 90 minutes. The PDMS solution was then deposited (approximately 1.5 grams) onto a PMMA wafer and the wafer was spun for 60 seconds in a spin-coating machine. The spin speeds were chosen between 1100 – 2200 RPM to achieve the desired final thickness. The wafer was then baked in an oven for 1 hour at $\sim 70^{\circ}$ C.

The PDMS was cut into $\sim$5mm square tiles with a razor blade and transferred to a glass slide to be characterized characterization. A Dektak Profilometer system was used to measure the thickness of PDMS membrane. The Dektak Profilometer was set to the lightest force setting, 1 mG, to prevent deformation of the PDMS. A reflective Ti spot was placed on the top surface of the PDMS to allow for the displacement measurement. The PDMS is a transparent polymer, and without the reflective spot the interferometer output signal would pass through the membrane –preventing displacement measurement. The Ti was transferred from a tinfoil shadow mask similar to gold leaf. It was approximately 100nm thick.

It was found that the cured PDMS will stiffen significantly when exposed to prolonged, extreme heat, such as seen in the e-beam evaporator. For this reason, the PDMS was never exposed to temperature above that seen during curing. Also, PDMS is prone to swelling in many common solutions [71], including acetone and silicon oil. To prevent swelling, the PDMS was placed after the final cleaning of the hydrophobic surfaces and oil treatment of the CYTOP surfaces.

3.6 Experimental Set Up and Equipment

A test platform for measuring the performance of the CFAM prototypes was developed and is shown in Figure 3.13. The system builds upon the CFA displacement measurement system designed by H. Wang [35]. The system consists of linear translation stages, optics, and an HP3631A power supply. LabVIEW software is used to control the voltage level.

Displacement was monitored using a fiber optic reflectometer from Luna Innovations, Inc., operated as an extrinsic Fabry-Perot interferometer. The optical fiber was secured into a holder with nail polish to minimize thermal drift and vibration of the fiber. The holder was a fixed to a flexible multi-axis stage control and a magnified top view camera allowed the fiber to be positioned over the reflective spot at the center of the membrane.

The side profile of the liquid bridge was monitored via side view camera, Prosilica GC2450 Camera (Allied Vision Tech) paired with a K2/SC Long-Distance Microscope (Infinity-USA) and ActiveGigE SKD Vision Driver (A & B Software). It was found that external illumination of the bridge was insufficient to provide the resolution required for characterization of the liquid bridge. It was therefore decided to illuminate the liquid bridge from within by adding fluorescent dye (fluorescein salt, Sigma-Aldrich) to the solution. The fluorescein salt has a peak excitation wave length of 460nm. The fluorescent dye was excited using a 405nm laser pointer aimed at the conducting drop from a stage. The resulting fluorescence has peak wave length emission of 515nm. To remove light directly from the laser pointer from entering the camera a bandpass optical filter was placed in front of the aperture of the side view camera, the pass band extends from was 488nm to 543nm, 488-EX/543-EM.

To maximize the resolution of the side profile the exposure of camera was increased to 1E6 µs. This allowed for clearer images, but reduced the frame acquisition rate to 1 frame per second. (The camera's maximum rate is 15.4 frames per second under ideal lighting conditions.) Furthermore, since the camera is designed for high resolution ($\sim$0.71 µm/px) imaging, the depth of focus is very small. Thus, large changes in contact line position were not able to be imaged. Figure 3.15 shows a sample side view profile. The drop appears white

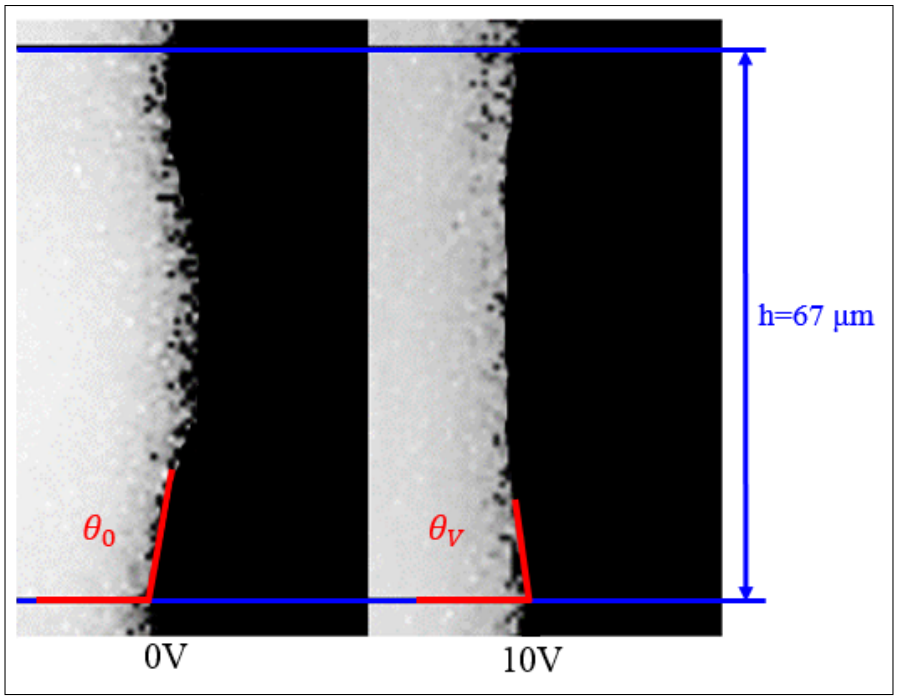

Figure 3.15: An example of a side profile view of the conducting drop. The drop is illuminated in white while the ambient is black. Note: the images are cropped for clarity.

in the figure, while the ambient is black. The images are cropped for clarity since the drop is reflected multiple times on the reflective surfaces of the plates.

The entirety of the experimental set up was housed in a clean box to minimize unwanted particulates and airflow over the experiment. To minimize the effects of evaporation, the clean box was saturated with humidity a minimum of 1 hour prior to experimentation. The humidity was added via warm wetted tex-wipe placed within the sealed clean box. Ideally in applications of CFAM the system will be closed preventing any evaporation.

The position/orientation of the optical fiber must be adjusted before each test so that the received signal is high quality at the starting position. As the membrane displaces the received signal will typically lose quality. This is seen more often in tests where the membrane displaced a great distance very quickly. Data collection is continuous; during large displacements the signal may be temporary lost, resulting in a large spike in the displacement data.

Additionally, the optical fiber is prone to thermal shift over long test periods. The drift is produced by the intensity of the light from the optical fiber and laser. The drift can be reduced during measurements by allowing a several minute cooldown between tests. Finally, vibrations may move the optical fiber and cause a loss of data quality. Vibration sources include opening/closing doors in the building's hallway and fluctuations in airflow from the building's HVAC system. The use of a vibration isolation table and a clean box helped reduce spurious responses to these sources.

Chapter 4

Static CFAM Dual Active Surface Device Results

After completing the fabrication of a prototype, each device underwent testing to examine actuator performance. In this chapter the static performance exhibited during these tests is reviewed with particular attention paid to the effects of membrane dimensions and bridge height on deflection achieved.

4.1 Summary of Static Tests Conducted

Table 4.1, presents a summary of the performed dual dielectric static prototypes. For convenience the tests have been label with Symbols A– O, and this designation is followed by the notation "-DAS" indicating Dual Active Surface whenever necessary to avoid confusion. (Note in the following chapter "-SAS" will be appended in a similar fashion to indicate a Single Active Surface test.) The displacement measurement signals recorded during each test are presented for all devices tested in Appendix G. For each prototype device the membrane radius was determined by optical measurement (Zeiss Microscope), and the membrane thickness was found via a Dektak Profilometer system. After prototype assembly, bridge height and contact angles were determined from examining video stills obtained from the profile

Table 4.1: Details of tests conducted.

Test	Bridge Height (µm)	Membrane Thickness (µm)	Membrane Radius (µm)	Max Volt (V)	Input
A-DAS	116	37	475	10	0.05 Hz square wave
B-DAS	83	46	480	10	0.05 Hz square wave
C-DAS	67	47	474	10	0.05 Hz square wave
D-DAS	68	47	474	10	0.05 Hz square wave
E-DAS	45	36	476	20	0.05 Hz square wave
F-DAS	65	35	326	20	0.05 Hz square wave
G-DAS	56	39	434	20	0.05 Hz square wave
H-DAS	67	47	474	20	0.05 Hz square wave
I-DAS	76	46	338	20	0.05 Hz square wave
J-DAS	69	47	474	20	0.05Hz square wave (R)
K-DAS	66	47	474	10	5 Hz square wave (R)
L-DAS	110	47	471	10	Staircase (5s_2V)
M-DAS	88	46	480	10	Staircase (10s_1V)
N-DAS	122	37	475	10	Staircase (5s_2V)
O-DAS	74	44	467	12	Staircase (5s_2V)

Staircase Wave inputs show step duration and increment in parenthesis, (R) indicated that the test was repeated for the assembled device. (i.e., both surfaces and electrolyte used for a second test).

(side view) imaging system. Capillary bridge radius was determined via volumetric analysis of the conducting electrolyte drop, see Section 2.2 for details of this calculation.

Figure 4.1 shows a typical membrane displacement curve for an 10V – 0.05Hz square wave CFAM-DAS device, the presented device is A-DAS. The time period used for comparison to the predicted model is 0 to 20 seconds. Before the first actuation, 0 – 10s, the displacement is a approximately 0, however the position reading decreases slightly from 0 due to thermal drift on the interferometer, a decrease of ∼0.1µm. Upon application of voltage step the majority of the displacement occurs almost instantaneous. After the large initial displacement, the membrane displacement is slightly exponential as the drop completely wets to the apparent angle. The membrane actuation displacement corresponds to the 2 times scales of electrowetting [33]. CFAM subjected to above CAS voltages do not show this exponential, but rather a decay in membrane displacement immediately following the applied voltage step – discussed in Section 4.4.1.

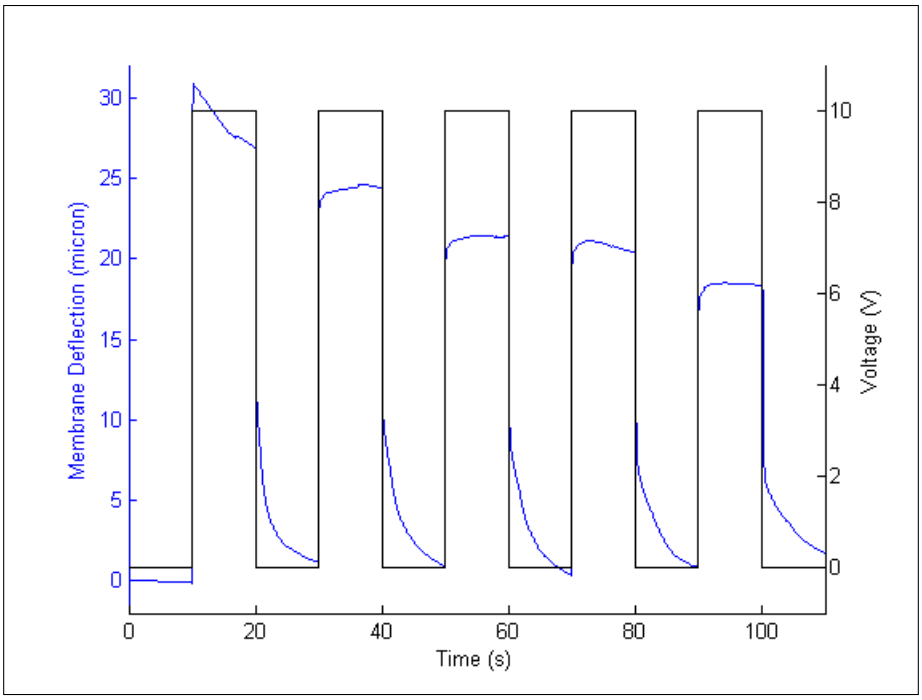

Figure 4.1: Membrane Displacement Curve for Test A-DAS with $h = 116$ µm – $t_m = 37$ µm – $r_m = 475$ µm.

The first actuation cycle has a slight decrease of deflection, this is thought to be from the loss of interferometer signal or hystersis, the subsequent cycles have more typical actuation curves as interferometer signal strength is a dynamic quality. After the removal of the voltage step, the drop retracts back to the equilibrium position and the membrane returns to nearly to the 0 position, with losses coming from hysteresis and charge injection. The return motion is slower than actuation motion and is discussed at length in Section 6.2.

4.2 Static Displacement Compared to Theoretical Model Predictions

Predicted displacements were calculated for Tests A-O using the governing equations presented in the Section 2.2. Membrane parameters used in the calculations were those measured for the prototype used. The capillary pressure was calculated from the measured bridge height and contact angles obtained from side view imaging whenever possible. In

Table 4.2: Measured values from testing and predictions from theory.

Test	R_c (µm)	ΔR_c (µm)	θ_{L_0} (°)	θ_{U_0} (°)	θ_L (°)	θ_U (°)	Measured Deflection (µm)	Theoretical Deflection (µm)	Abs. % Error
A-DAS	1738	4	99	93	85*	83**	26.3	24.7	6.1
B-DAS	2102	3	95	94	87	83	16.8	16.7	0.6
C-DAS	1973	7	102	97	85	83	29.1	29.0	0.3
D-DAS	1948	7	106	89	83*	83**	23.5	27.1	15.3
E-DAS	2369	18	106	86	83**	83**	75.7	59.3	21.7
F-DAS	1888	1	96	79	83**	83**	13.9	4.5	67.6
G-DAS	2185	6	96	94	84	86	24.1	26.0	7.9
H-DAS	1963	8	105	94	83**	83**	46.9	30.8	34.3
I-DAS	1932	1	103	103	83**	83**	12.1	9.5	21.5
J-DAS	1942	5	98	90	83**	83**	38.7	20.7	46.5
K-DAS	–	–	–	–	–	–	∼7.4	–	–
L-DAS	1785	2	102	92	88*	83**	14.2	13.3	6.3
M-DAS	1965	4	97	95	83	86	19.5	18.9	3.1
N-DAS	1694	3	101	89	87	83	19.8	19.8	0.0
O-DAS	1876	7	101	99	83**	83**	27.9	31.8	14.0

For angles marked * or ** final contact angles were not determinable from imaging and were predicted from the saturated Lippmann-Young model. * indicates that the model did not yield a saturated angle and so the Lippmann - Young angle was used; ** indicates that the model yielded the saturation angle. Note: some measured values and theoretical predictions are not available for Test K since the input frequency (5Hz), was higher than the frequency of the camera's frame acquisition rate (∼1Hz).

some cases, the final angle was unobservable due to drop movement – see Section 2.4. The measurements reported in Table 4.2 and the theory values provided for comparison are for the first actuation cycle of the device in each square wave test. For staircase inputs the values correspond to those for the maximum applied voltage. The measured deflection is calculated from the time displacement curves. To avoid transient effects, the position readings used to calculate measured deflection are taken just prior to application or removal of the applied voltage step. The position is averaged over 10 data points (156 ms) of the aforementioned measurement points.

Figure 4.2, shows a linear correlation between the predicted static displacements and the measured static displacements. A line with slope 1 is also provided in the figure. In general,

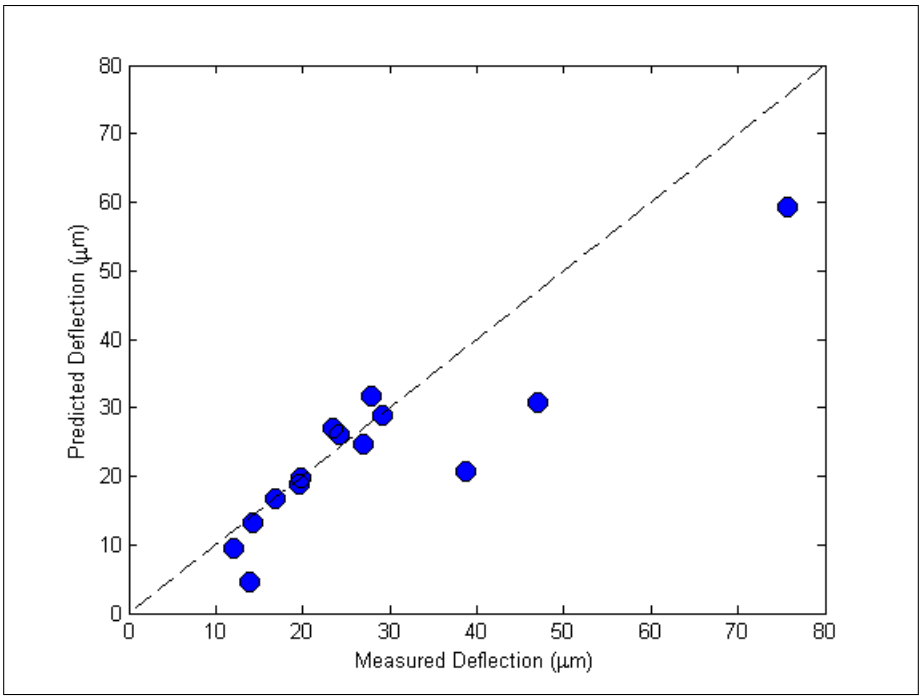

Figure 4.2: Correlation of Measured Deflection to Predicted Deflection.

the theoretical predictions largely lie in proximity to the line indicating that the devices are largely behaving as predicted. Furthermore, it can be easily seen that substantial membrane deflections are achieved with a large variety of device configurations.

The highest error is 67.6% between the predicted displacement and measured displacement. The averages and medians are much lower at 17.5% and 11.0%. The reason for the error is the inability to image the entirety of the drop contact line, and the high frequency of the contact line moving out of the depth of focus for the long distance microscope, the side profile imaging device. The possible unseen test irregularities include natural variations in the saturation angle, hysteresis, drop pinning and unequal bridge heights outside of the field of view. Support for the unseen irregularities comes from the excellent agreement to the model in the devices where final and initial angles were visually quantifiable, where the average error is 3.6% with a median of 3.1%.

The overall low error is supportive that the governing equations can be used to predict membrane displacement with high accuracy greatly simplifying future membrane parameter

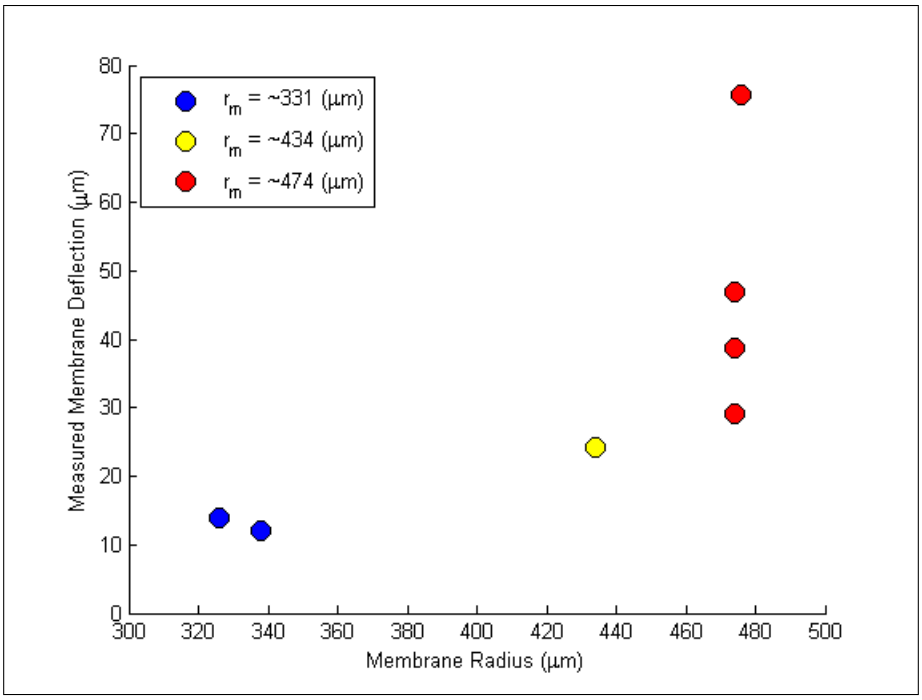

Figure 4.3: Effect of membrane radius on measured membrane deflection, at 20V applied voltage potential.

selections for device design.

4.3 Trends in Static Displacement Results

Several trends seen in the test results related to maximum deflection achieved are now examined. The most significant of these is the strong effect that membrane radius has on deflection, this is seen in Figure 4.3. This figure shows the maximum deflection achieved with 20 V for a variety of prototypes (varying bridge heights and membrane thicknesses) versus the membrane radius. (The change in contact angle occurring in these tests are similar.) While parameters such as membrane thickness still influence the displacement achieved, the impact of membrane radius is substantial: decreased membrane radius significantly lowers achievable deflection, a result that is entirely consistent with theory.

Figure 4.4 presents a similar plot, but this time it is membrane thickness that is examined. It is apparent that the membrane thickness plays a more minor role in defection compared

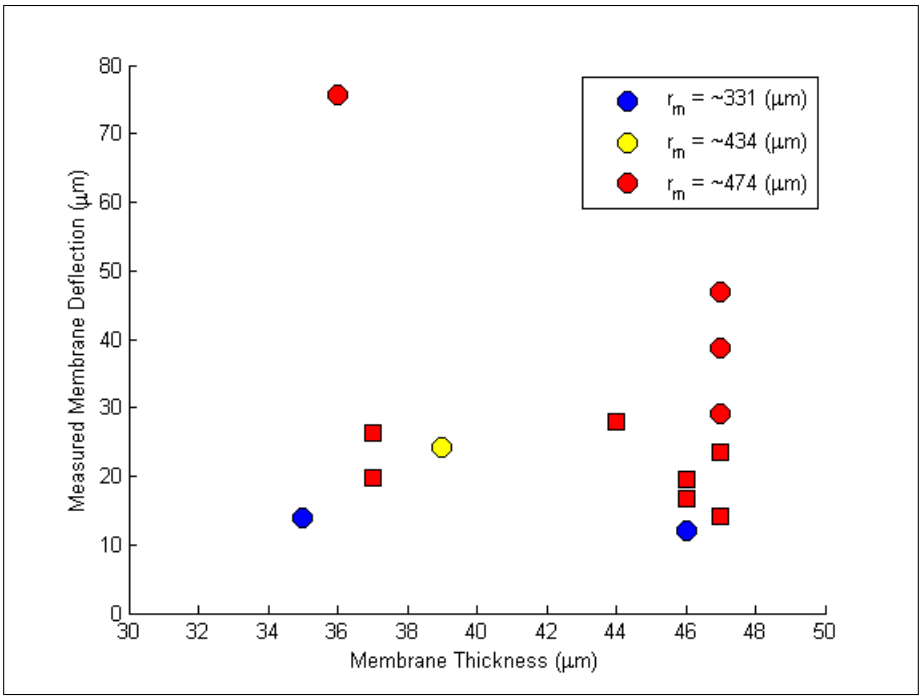

Figure 4.4: Effect of membrane thickness on measured membrane deflection, circle markers indicate a voltage below that associated with contact angle saturation; square markers indicate a potential above contact angle saturation.

to membrane radius. All other parameters equal, thinner membranes do deflect further, but the effect does not overwhelm the impact of other variations between devices.

There is a correlation between the capillary bridge height and measured deflection, as expected from the theory. Shorter bridge heights result in greater deflection as seen in Figure 4.5. However, choice of applied voltage (not pictured), membrane radius and membrane thickness may offset the deflection increases brought on by shorter capillary bridge height.

Let us now examine the correlation between capillary pressure during electrowetting and displacement achieved. As theory predicts (see Chapter 2) there is a strong correlation between these variables over multiple tests – see Figure 4.6. It can be seen that larger changes in capillary pressure result in larger deflections, but that the magnitude of deflection can be greatly hindered by small membrane radius. When the pressure change is minor, nevertheless, the membrane deflection will be as well.

Not surprisingly, as Figure 4.7 shows, higher membrane deflections are achieved at higher

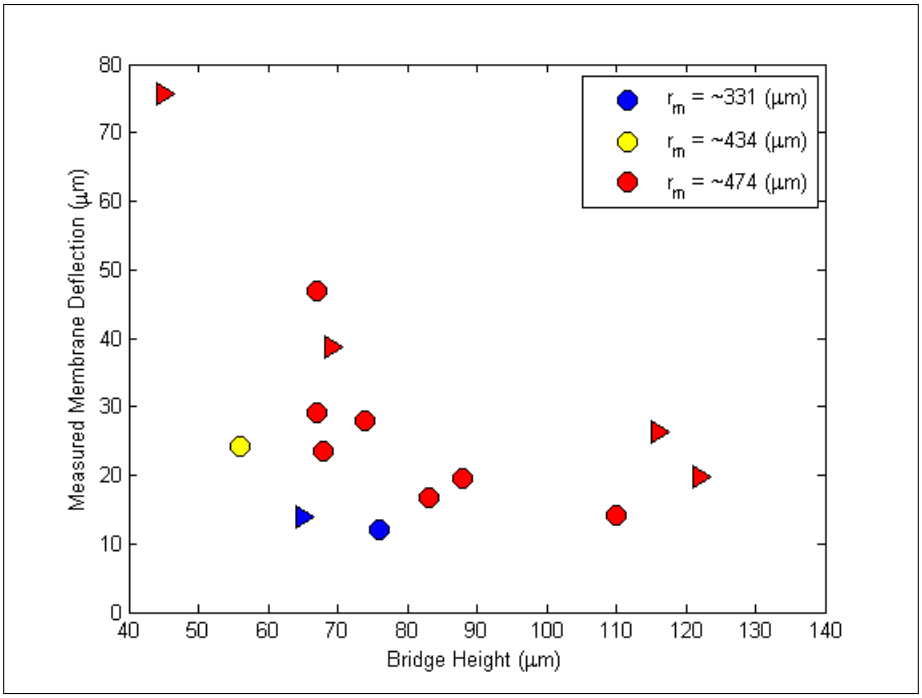

Figure 4.5: Effect of bridge height on measured membrane deflection. Circle markers indicate a membrane thickness of ∼45 microns, while triangle markers indicate a membrane thickness of ∼35 microns.

voltages, since these are generally associated with larger changes in capillary pressure. The reader will note that data is more closely grouped together at the 10V applied potential; the clustering of data for tests with thin and thick membranes is an artifact of testing - a result of the thicker membrane tests being conducted at smaller bridge heights. The two smaller deflections of the thick membrane prototypes at 10V have bridge heights comparable to the thin membrane cases at 10V. Overall, it can be seen increased voltage has a strong impact on achievable deflection over the range of voltages considered; at higher voltages bridge height and membrane thickness can be seen to result in significant variations in displacement.

As Figure 4.8 demonstrates, larger membrane deflection is strongly correlated to the increase in contact line radius. The change in contact line radius increases both in response to any decrease in contact angle (greater wetting) and in response to smaller bridge height. Both of these are, of course, associated with a larger change in capillary pressure, thus resulting in larger membrane deflections. Along the same line of argument, the further the

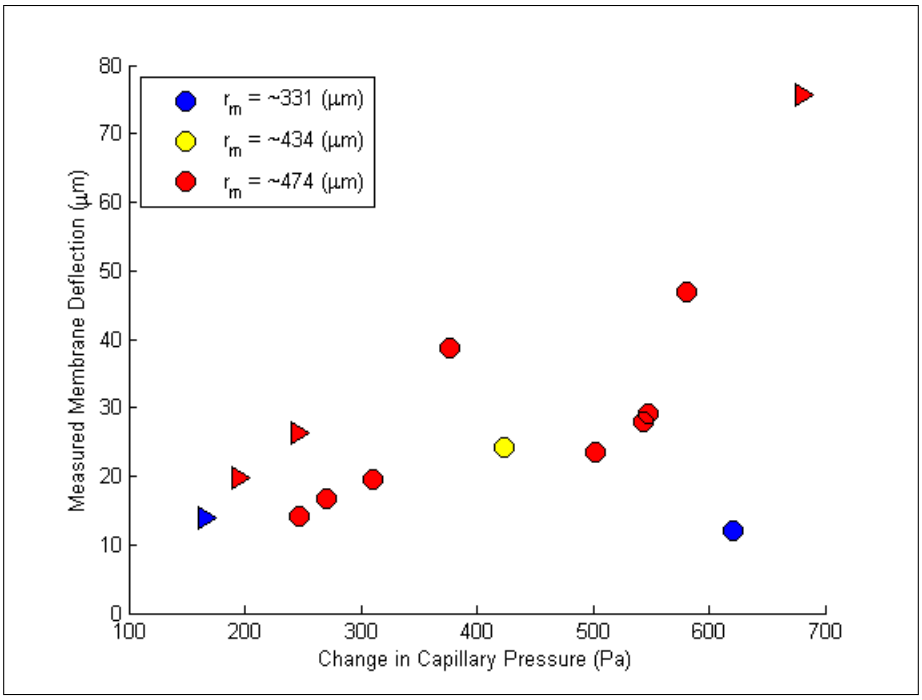

Figure 4.6: Effect of change in capillary pressure on measured membrane deflection. Circle markers indicate a membrane thickness of ∼45 microns, while triangle markers indicate a membrane thickness of ∼35 microns.

membrane deflects downward the more fluid volume is displaced, and thus the further the capillary radius must displace outward.

4.4 Comparisons between Individual Tests

In this subsection we examine direct comparisons between the measured displacements in pairs of tests where all but a single parameter are nearly the same. These comparisons allow for a more direct examination of the impact of a parameter on performance than that obtainable via trend analysis (Section 4.3).

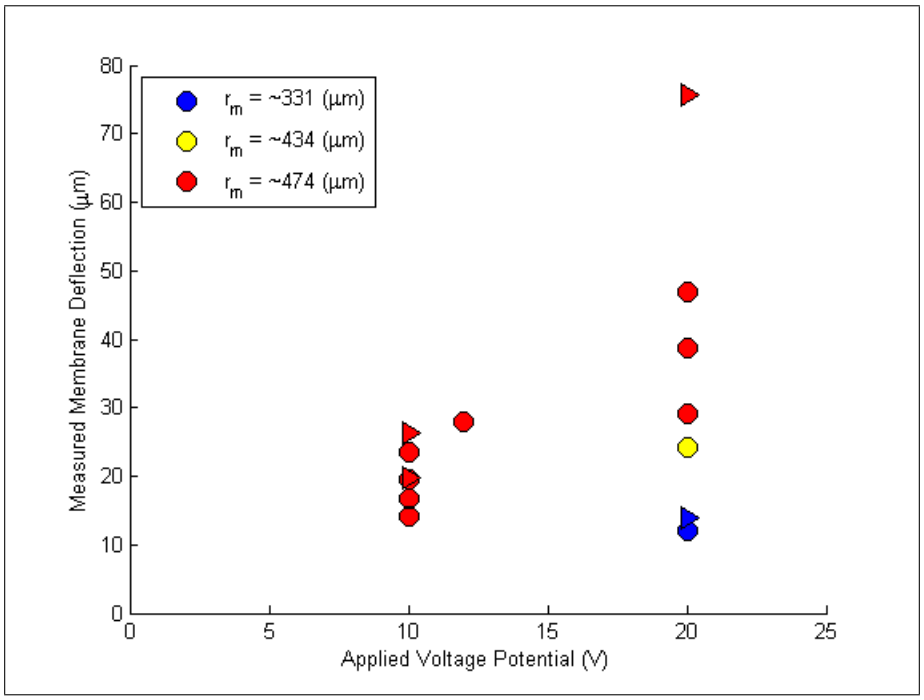

Figure 4.7: Effect of applied voltage potential on measured membrane deflection. Circle markers indicate a membrane thickness of ∼45 microns, while triangle markers indicate a membrane thickness of ∼35 microns.

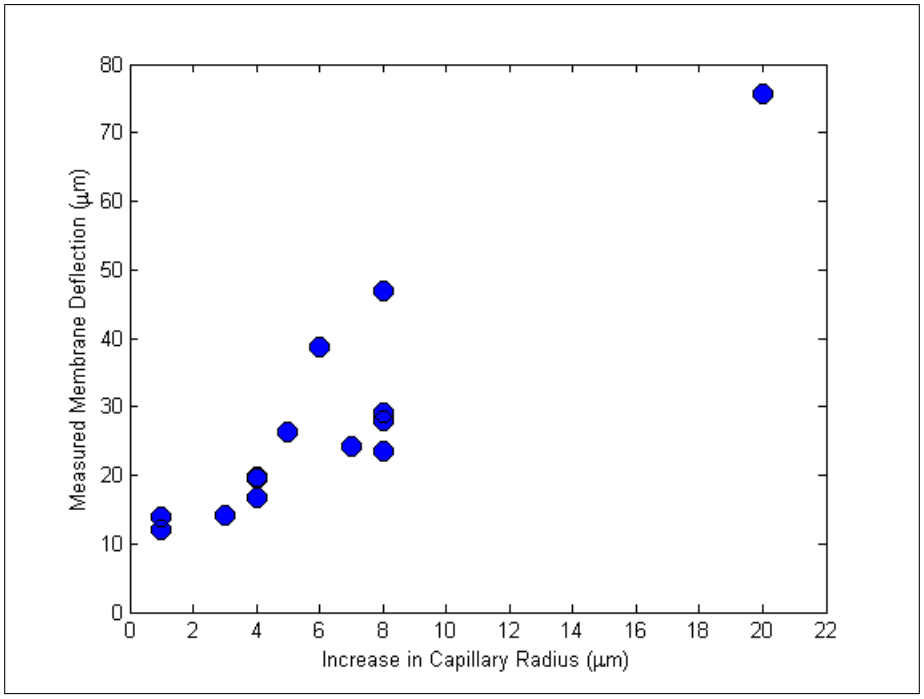

Figure 4.8: The correlation between the increase in capillary radius and the measured membrane deflection.

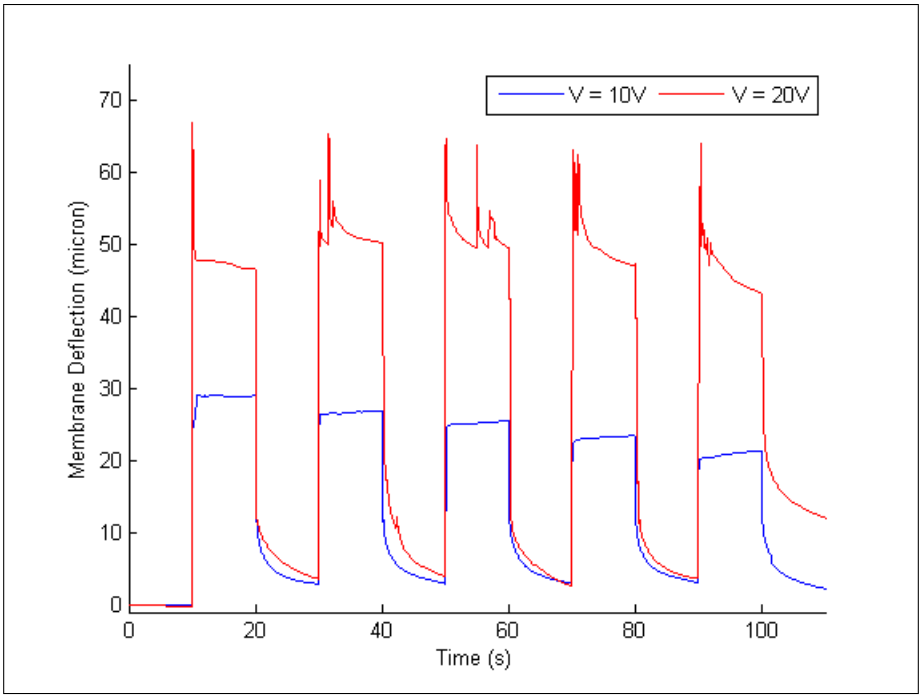

Figure 4.9: Comparison of membrane deflection results for two applied voltage square waves.

4.4.1 Effects of voltage potential on the displacement of the membrane

Figure 4.9 shows a comparison of the membrane displacement for tests C and H. The tests employ an actuator of nearly the same bridge height and identical membrane radius and thickness. (The same top plate is used in these tests; the bottom plate and droplet are new. Reassembly results in a slight variation in bridge height.) The difference between these two experiments is primarily the voltage first applied in square wave testing, 10V in Test C and 20V in Test H. These potentials were chosen to sample the behavior below and above the contact angle saturation voltage. Due to the saturation, the 20V case can be considered the maximum achievable deflection associated with prototypes of this construction and dimensions.

The higher voltage results in a significantly larger displacement of the membrane, an increase of 62.2% (17.8 µm), on the first actuation cycle. The increased displacement comes

from the larger change in capillary pressure due to the lower contact angles achieved. The percent increase in membrane displacement is quite significant since the contact angles in the 10V case (Test C) are not far from those associated with contact angle saturation. Test H is performing significantly better than was expected with the saturated LY model suggesting that contact angles better than saturated LY model predicts were obtained in this test. These results strongly indicate the benefit of improving contact angle saturation behavior to actuation performance.

The reader will note in examining Figure 4.9 that the 10V cycles exhibit a much more repeatable deflection behavior than those seen with 20V case. The irregularities seen in the 20V test stem from the nature of cyclic wetting above the saturation voltage. It is hypothesized that the that the larger applied potential causes the conducting electrolyte drop to momentarily wet out below the angle that is statically achieved. Thus a greater deflection is achieved in the transient immediately after the voltage is applied; the contact line then retracts to the static equilibrium position, causing the decay in membrane displacement immediately following the applied voltage step. With the current frame rate of the side view camera ($\sim$1Hz) this transient even cannot be captured. This transient should not be confused with the large spikes sporafically seen in the displacement. These artifacts are believed to be a result of a momentary misreading by the interferometer caused by a sudden change in displacement (e.g. drop shift), and are discussed in Section 3.6.

4.4.2 Effect of bridge height on the displacement of the membrane

Figure 4.10 shows the measured deflection during 10V square wave testing of two devices where all parameters are nearly identical with the exception of capillary bridge height; in Test B the height is 17.4 µm (24%) greater than in Test C. The magnitude of capillary pressure change is inversely proportional to bridge height and therefore devices with shorter bridges should exhibit larger deflections. As expected, the device with the shorter capillary bridge displaces the membrane significantly more (12.3 µm, 73.2%) than the taller bridge device

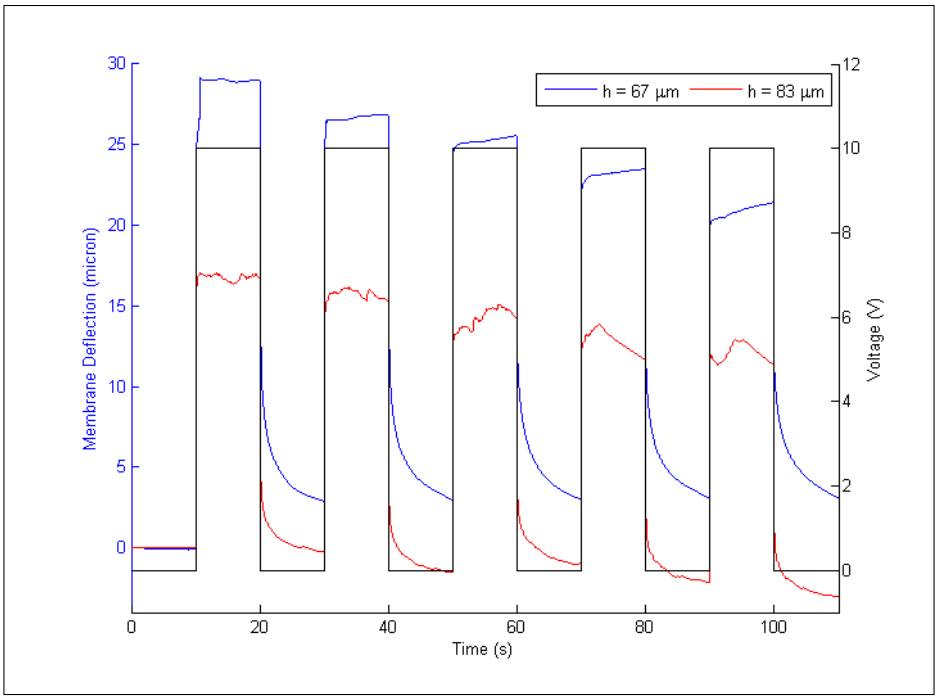

Figure 4.10: Comparison of membrane deflections with 10V square wave. Effect of bridge height on behavior.

during the first actuation cycle. The results show that relatively modest decreases in bridge height can have a significant impact on deflections achieved. The reader will note that the shorter bridge device has a slightly greater loss of deflection with repeated actuation than its counterpart. A hypothesized cause for this is that greater fluidic resistance is achieved in the case of the shorter bridge, accentuating the impact of contact angle hysteresis.

4.4.3 Effect of membrane radius

In Figure 4.11 the displacements achieved in Tests H and I are shown. Both tests are conducted with 20V square wave applied potential and have nearly identical membrane thicknesses. Test H has an 11% smaller bridge height than Test I and a significantly larger membrane radius (474 µm vs. 338 µm, 40.2% greater). From both theory and trend analysis we expect that the predominant factor in influencing the difference in displacements between these tests would be membrane radius. The smaller radius test shows much smaller membrane displacement (12.1 µm) than that achieved by its larger radius counterpart (46.9

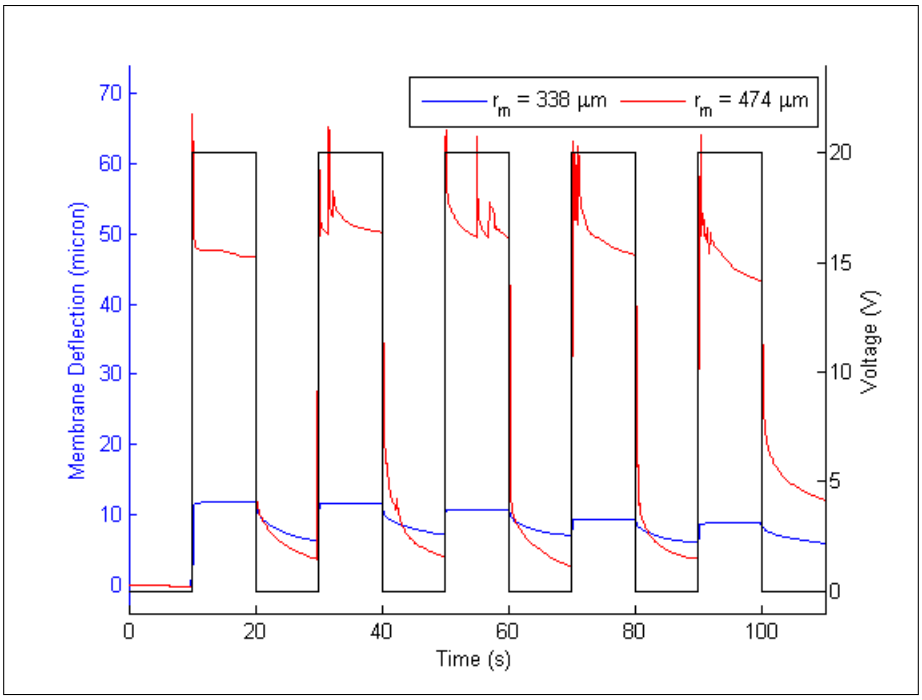

Figure 4.11: Comparison of membrane deflection with 20V square wave. Impact of membrane radius on achieved deflection. devices with varied membrane radius.

µm).

To confirm that the height variations between these tests did not significantly contribute to the differences in displacement seen, the theoretical displacements were calculated for each device using the capillary pressures predicted for each test. Recall that a variation in bridge height influences membrane displacement by altering the capillary pressure. For the device used in Test H (larger membrane radius), the predicted displacements was 30.8 µm using the capillary pressure change of Test H (shorter bridge) and 32.3 µm using the capillary pressure change of Test I (longer bridge). For the device used in Test I these predicted displacements were 9.5 µm and 8.9 µm, respectively. The difference between these predicted displacements is quite small in both calculations indicating that the effect of the difference in bridge height between Test H and Test I is a very small contributor to the difference in deflections seen. The huge difference in membrane displacement in this comparison is due overwhelmingly to the difference in membrane radius. Finally, it should be noted that Test I shows a very

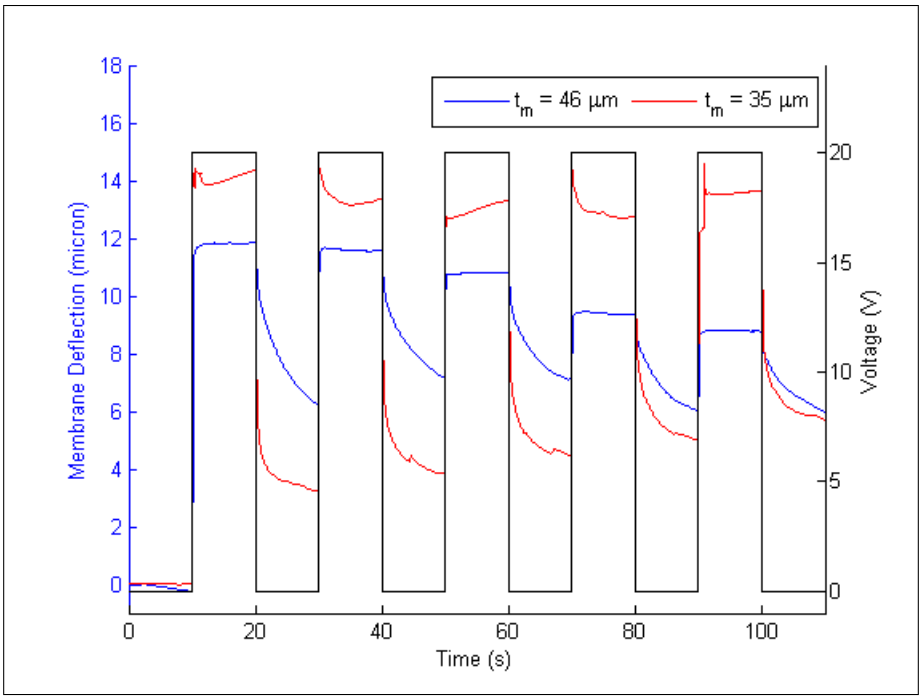

Figure 4.12: Comparison of displacements in tests with varied membrane thickness, 20V square wave voltage signal.

hysteretic response after its first actuation cycle, resulting in decreased membrane return to equilibrium in subsequent cycles. As this is a 20V test we expect that charge trapping was particularly important here; the underlying cause, however, is unknown.

4.4.4 Effects of membrane thickness on the displacement of the membrane

Our final comparison examines the effect of membrane thickness on deflection. Tests F and I are comparable 20V square wave tests in this regard and their displacement signals are shown in Figure 4.12. Tests L and N are also comparable; the input signal in these tests was a staircase voltage signal with a 10V maximum, - see Figure 4.13 for their displacement signals. We expect from theory and trend analysis that the membrane thickness will have a relatively moderate effect on deflection in comparison to bridge height and membrane radius.

The devices in Tests F and I have a membrane thickness 35.3 µm and 46.0 µm respectively.

The other device parameters are comparable although the membrane radii and heights vary slightly. (The effect of these differences will be analyzed later) As expected the test with the thinner membrane deflects a greater distance than that with the thicker membrane. However, the difference in displacement is rather minor; a 23.3% decrease membrane thickness results in just a 14.9% increase in the static displacement during the first actuation cycle.

As noted previously the bridge height and membrane radius also vary between Tests F and I. The effect of the difference in bridge heights, in fact, works in favor of the thinner membrane test since the thicker membrane test has a greater bridge height. If the two tests had identical heights the difference in the displacements should be even less than 14.9% seen in Figure 4.11. However, the thinner membrane test (F) also has a smaller membrane radius (326 µm) than its counterpart (338 µm) which would tend to decrease its deflection – could this be responsible for the minor difference in performance?

To see the ideal effects of membrane thickness, the theoretical displacements were calculated for each device using the capillary pressure change of Test I (-621 Pa), and the membrane radius of Test I (338 micron). This comparison therefore removes the effect of any bridge height or membrane radius variation from the comparison of performance; in this theoretical comparison, only membrane thickness is different between the two tests. For the device in Test F, the predicted displacement was 18.9 µm using the capillary pressure change and membrane radius of Test I. For the device in Test I the predicted displacement was 9.5 µm using the same capillary pressure change and membrane radius. While the measured difference between the membrane displacement in Tests F and I was only 1.8 µm, When the compared at the same pressure change and membrane radius, the difference in theoretical membrane deflection is much larger, 9.4 µm.

One possible reason for the rather small difference in the two tests may be the increase in PDMS' Young's modulus when spun at higher speeds so as to achieve reduced thickness. It is believed the chains of spin coated PDMS become more aligned with increased spin RPM [64]. The Young's moduli reported for membrane thicknesses of 46.0 and 35.0 microns

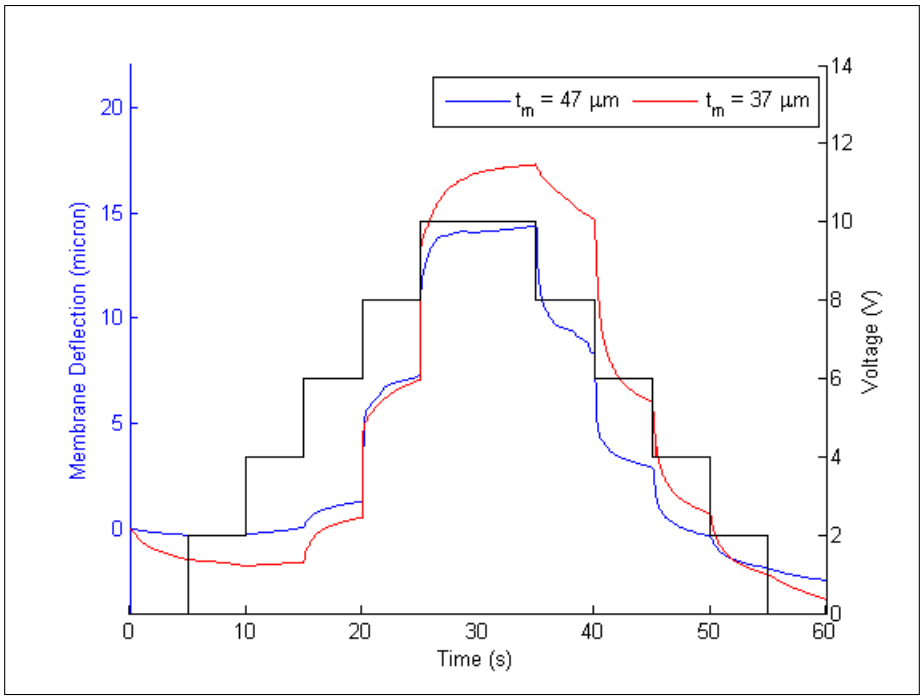

Figure 4.13: Comparison of devices with varied membrane thickness, 10V staircase wave.

are 1.22 MPa and 1.34 MPa respectively. However, this is unlikely to fully account for the small difference.

Our second comparison examines the data from Test L and Test N. The membrane thickness in these tests are 47 µm and 37 µm, respectively. The remaining parameters are similar although the bridge height varies slightly; the effect of this difference will be analyzed later. What sets the L/N comparison apart from that just examined is that Tests L and N have larger membrane radii and bridge heights. Figure 4.13 presents the comparison of deflections during Tests L and N. The thinner membrane (N) deflects further than the thicker membrane (I) by 5.6 microns at the peak voltage, an increase of 39.4%. This percent increase is comparable in magnitude to the decrease in the membrane thickness from I to N (21.2%), demonstrating again that the effect of changes in membrane thickness is much less dramatic than bridge height or membrane radius.

The height varies by 12 microns; to see the effect of this height variation on the deflection of the membrane, the theoretical displacements were calculated for each device using capillary

pressure change of each device. For device in Test L, the predicted displacements were 13.3 microns and 10.5 microns for capillary pressure changes of Tests L and N respectively. The device in Test N had predicted displacements of 19.8 microns and 24.3 microns for capillary pressure change of Tests N and L respectively. The difference in height, therefore, is likely a small contributor to the variations between tests. Theory predicts that variation between tests should, in fact, be much greater than that actually seen when the differences in height are accounted for. Just as in the F/I comparison the effect of membrane thickness is quite moderate in test results and is smaller than one would expect from theory. This again raises the possibility that differences in Young's modulus could be a contributor.

4.5 Displacements with an Ideal Lippmann-Young Model

The predicted static displacements were also calculated using an ideal Lippmann-Young model for the contact angles. The initial angle was chosen to match the typical sessile angle of the conducting electrolyte drop on the CYTOP surface of the CFAM (103°). The final angle corresponds to the predicted Lippmann-Young angle at the maximum input voltage for the test. Contact angle saturation was ignored so as to examine the detrimental impact of saturation on device performance. Table 4.3 presents the calculated angle data of the ideal Lippmann-Young prediction for each test along with the resulting predicted membrane deflections.

A comparison of the deflection predictions made with the Saturated Lippmann-Young model (Table 4.2) and with the Ideal Lippmann-Young model (Table 4.3) for those tests conducted at voltage potentials below that associated with contact angle saturation (Tests A-D, K-O) shows that these predictions are in good agreement; the average discrepancy is just 15.5%. In these cases, the discrepancy results only from the differences in the zero-voltage contact angle used in the two models. This result, although expected, demonstrates that the tested CFAM devices are functioning as an ideal Lippmann-Young model predicts

Table 4.3: Ideal Lippmann - Young Angle Values and Predicted Deflection.

Test	Bridge Height (µm)	Mem. Thickness (µm)	Mem. Radius (µm)	Max Volt (V)	R_c (µm)	ΔR_c (µm)	θ_0 (°)	θ_V (°)	Ideal L-Y Predicted Deflection (µm)
A-DAS	116	37	475	10	1738	4	103	89	24.2
B-DAS	83	46	480	10	2102	3	103	89	22.3
C-DAS	67	47	474	10	1973	7	103	89	24.5
D-DAS	68	47	474	10	1948	7	103	89	24.2
E-DAS	45	36	476	20	2369	18	103	44	122.7
F-DAS	65	35	326	20	1888	1	103	44	43.0
G-DAS	56	39	434	20	2185	6	103	44	84.9
H-DAS	67	47	474	20	1963	8	103	44	75.2
I-DAS	76	46	338	20	1932	1	103	44	24.6
J-DAS	69	47	474	20	1942	5	103	44	73.8
K-DAS	66	47	474	10	-	-	-	-	-
L-DAS	110	47	471	10	1785	2	103	89	15.5
M-DAS	88	46	480	10	1965	4	103	89	21.2
N-DAS	122	37	475	10	1694	3	103	89	23.2
O-DAS	74	44	467	12	1876	7	103	83	36.1

Note: Test K is a high frequency input test; no predicted values are available.

below the saturation voltage. However, the difference in predicted displacements made by the two models for the tests conducted above the voltage of contact angle saturation is very large – see Figure 4.14. Without contact angle saturation (Ideal L-Y model) membrane deflection would be 2–4 times greater than it is when saturation is present (Saturated L-Y model). Thus, the actuation performance would be greatly improved for a wide variety of device configurations if the saturation behavior of the electrowetting surface could be improved, even moderately.

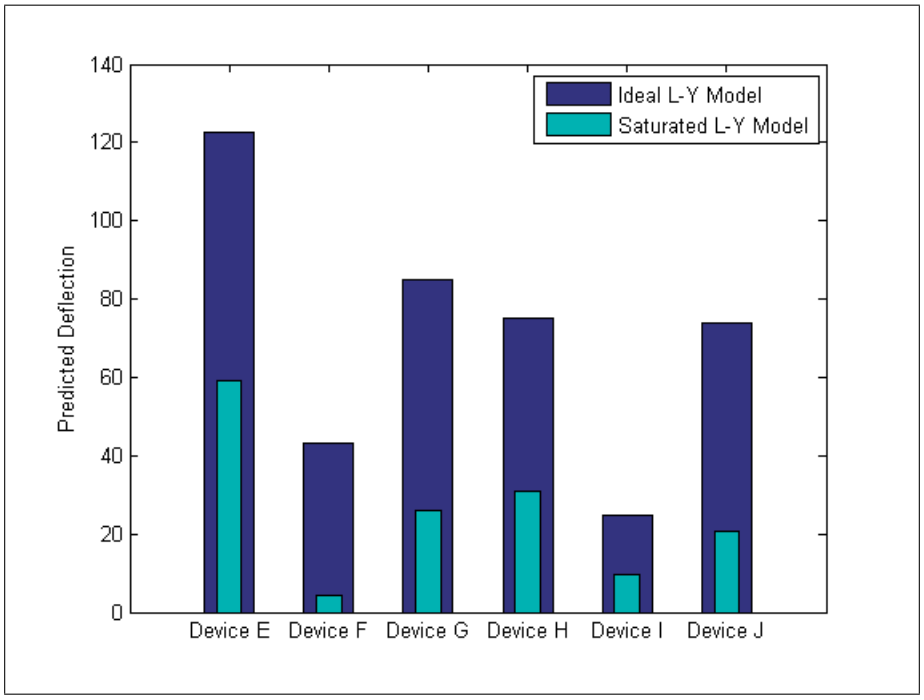

Figure 4.14: Comparison of deflection predictions with ideal Lippmann-Young model and with Saturated Lippmann-Young model, for tests where voltages exceeded that associated with contact angle saturation.

Chapter 5

Static Performance of Single Active Surface Prototypes

The performance of CFAM devices in which the liquid bridge electrowets on only one of the two solid surfaces that it spans between is reviewed in this Chapter. This is an alternative device configuration to that studied in Chapter 4 and is referred to the *Single Active Surface* (SAS) configuration. The governing equation for this configuration, however, are the same as for the dual active surface case, only the contact angles on the passive surface (i.e., the one without electrowetting) do not change due to the applied voltage potential. The results presented will focus on the effects of varying design parameters on the membrane displacements achieved.

5.1 Summary of Static Tests Conducted

Table 5.1 presents a summary of the tests conducted on prototypes with a single electrowetting surface. For convenience the tests have been labeled with letters A– Q and this designation is followed by the notation "-SAS" indicating *Single Active Surface* whenever necessary to avoid confusion. For any comparisons to dual active surface devices those tests will be labeled with the suffix "-DAS". Displacement signals from each test conducted are pre-

Table 5.1: Details of tests conducted.

Test	Bridge Height (µm)	Membrane Thickness (µm)	Membrane Radius (µm)	Max Volt (V)	Input
A-SAS	98	33	515	12	0.167 Hz square wave
B-SAS	125	39	439	16	0.167 Hz square wave
C-SAS	102	39	439	16	0.167 Hz square wave
D-SAS	108	39	438	14	0.167 Hz square wave
E-SAS	111	40	441	14	0.167 Hz square wave
F-SAS	106	40	442	16	0.167 Hz square wave
G-SAS	95	41	438	14	0.167 Hz square wave
H-SAS	95	24	442	22	0.167 Hz square wave
I-SAS	117	39	438	22	0.167 Hz square wave
J-SAS	93	39	438	22	0.167 Hz square wave
K-SAS	93	41	438	22	0.167 Hz square wave (R)
L-SAS	91	39	510	10	Staircase (1s_1V)
M-SAS	93	39	510	25	Staircase (1s_1V)
N-SAS	123	39	439	24	Staircase (3s_1V)
O-SAS	94	39	439	24	Staircase (3s_1V) (R)
P-SAS	111	40	441	20	Staircase (3s_1V)
Q-SAS	96	50	510	25	Staircase (3s_1V)

Staircase Wave inputs show step duration and increment in parenthesis,
(R) indicated that the test was repeated for the assembled device.

sented in Appendix H. The membrane radius and thicknesses were determined as described in Chapter 4. Bridge heights and contact angles were determined via video stills from the side view imaging system, presented in table 5.2. Capillary bridge radius was determined via volumetric analysis of the electrolyte drop, see Section 2.2 for details of the calculation.

5.2 Static Displacement Results and Comparison to Theory

Figure 5.1, shows the correlation between the predicted static displacements and the measured static displacements during single active surface tests. A line of slope 1 is also provided so that the quality of the correlation can be more easily visually evaluated by the reader. In

Table 5.2: Measured values from testing and predictions from theory.

Test	R_c (µm)	ΔR_c (µm)	θ_{L_0} (°)	θ_{U_0} (°)	θ_L (°)	θ_U (°)	Measured Deflection (µm)	Theoretical Deflection (µm)	Abs. % Error
A-SAS	1188	4	99	88	89	92	8.6	10.1	14.9
B-SAS	1086	1	97	95	85	98	6.0	5.4	11.1
C-SAS	1736	1	95	88	87	89	4.6	5.5	16.4
D-SAS	967	2	91	101	81	104	6.2	4.7	31.9
E-SAS	1235	3	103	94	80	98	13.4	12.2	9.8
F-SAS	1699	2	97	90	84	91	7.3	8.6	15.1
G-SAS	685	5	101	84	79	93	8.7	9.3	6.5
H-SAS	1242	4	101	83	83	95	12.6	12.8	1.6
I-SAS	1350	1	102	79	86	86	5.4	6.1	11.5
J-SAS	1512	2	99	97	85	100	6.7	8.4	20.2
K-SAS	695	6	103	88	84	91	11.5	11.3	1.8
L-SAS	1265	1	102	100	95	102	3.0	4.3	30.2
M-SAS	1357	4	107	58	89	64	15.2	13.8	10.1
N-SAS	1580	3	103	99	78	100	15.5	14.3	8.4
O-SAS	1805	1	101	89	83	96	7.3	9.0	18.9
P-SAS	1235	3	101	91	80	94	13.9	11.9	16.8
Q-SAS	1328	3	104	86	80	94	9.2	12.3	25.2

general, the correlation between measured and predicted values is quite good.

While the design parameters (height, membrane thickness, and membrane radius) are similar to the dual active surface results presented in Chapter 4, the deflections achieved are significantly lower for the singles active surface devices. The maximum measured deflection was in Test N with a displacement of 15.5 micron under 24V applied.

The discrepancy between measured and predicted deflections over the tests conducted had an average value of 14.8% and a median value of 14.9%. These metrics are higher than the corresponding values in dual active surface tests. However, the highest discrepancy for SAS tests was 31.9% which was significantly lower than that seen in DAS tests. This is to be expected since the very large discrepancies in DAS tests were due to our inability to image the bridge profile. The averages and medians discrepancies in the SAS tests, however, are much larger than those values in DAS tests where the contact angles were

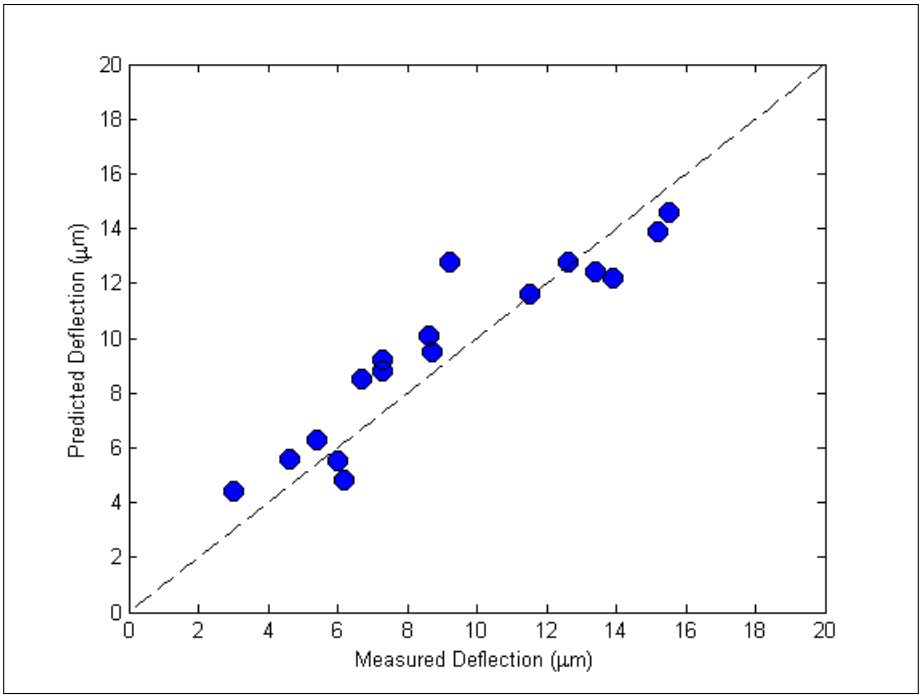

Figure 5.1: Correlation of Measured Deflection to Predicted Deflection.

visually determinable (compare the average discrepancy 14.8% for SAS vs. 3.6% for DAS). We believe that the reason for this situation is our inability to examine the bridge profile over the entire liquid/gas interface of the bridge. There is the possibility that the contact angles around the bridge's perimeter are not equal due to surface hysteresis and that the measured angles are not predictive of the actual change in capillary pressure.

5.3 Effect of the Passive Surface

An examination of the results from the SAS prototypes shows that their behavior was much less repeatable then for DAS prototypes (Chapter 4). The cause of this result is wetting hysteresis on the passive surface. During the first deflecting actuation of the membrane the liquid bridge advances on both the passive and active surface. While the contact angle on the active surface will largely be dictated by the electrowetting curve, the contact angle on passive surface should be unchanged, remaining at the (equilibrium) sessile contact angle

Table 5.3: Contact angles at 0V and at maximum voltage for SAS tests. Also presented is the calculated change in capillary pressure as well as the corresponding value assuming no hysteresis (NH) on the passive surface.

Test	θ_{L_0} (°)	θ_{U_0} (°)	θ_L (°)	θ_U (°)	ΔP_c True (Pa)	ΔP_c NH (Pa)
A-SAS	99	88	89	92	72	121
B-SAS	97	95	85	98	85	114
C-SAS	95	88	87	89	81	93
D-SAS	91	101	81	104	77	110
E-SAS	103	94	80	98	202	244
F-SAS	97	90	84	91	134	145
G-SAS	101	84	79	93	162	274
H-SAS	101	83	83	95	74	224
I-SAS	102	79	86	86	91	161
J-SAS	99	97	85	100	140	178
K-SAS	103	88	84	91	203	242
L-SAS	102	100	95	102	65	90
M-SAS	107	58	89	64	160	227
N-SAS	103	99	78	100	230	239
O-SAS	101	89	83	96	138	226
P-SAS	101	91	80	94	191	223
Q-SAS	104	86	80	94	196	294

Change in capillary pressure for NH case is calculated assuming no change in passive surface contact angle.

for the passive surface. However, due to wetting hysteresis the contact angle on the passive surface increases, becoming greater than the sessile contact angle. The degree of hysteresis the passive surface has varies from sample to sample, and is very sensitive to fabrication processing. While precautionary steps were taken to minimize the wetting hysteresis of the passive surface, a hysteresis of approximately 10° seems unavoidable for a water/air system on CYTOP [35].

The increase in the passive surface contact angle tends to reduce the curvature of the bridge profile and thus lessen the change in capillary pressure during electrowetting. Table 5.3 presents the calculated capillary pressures for the CFAM-SAS tests. Also presented is the capillary pressure change that would have occurred if the passive surface contact angle

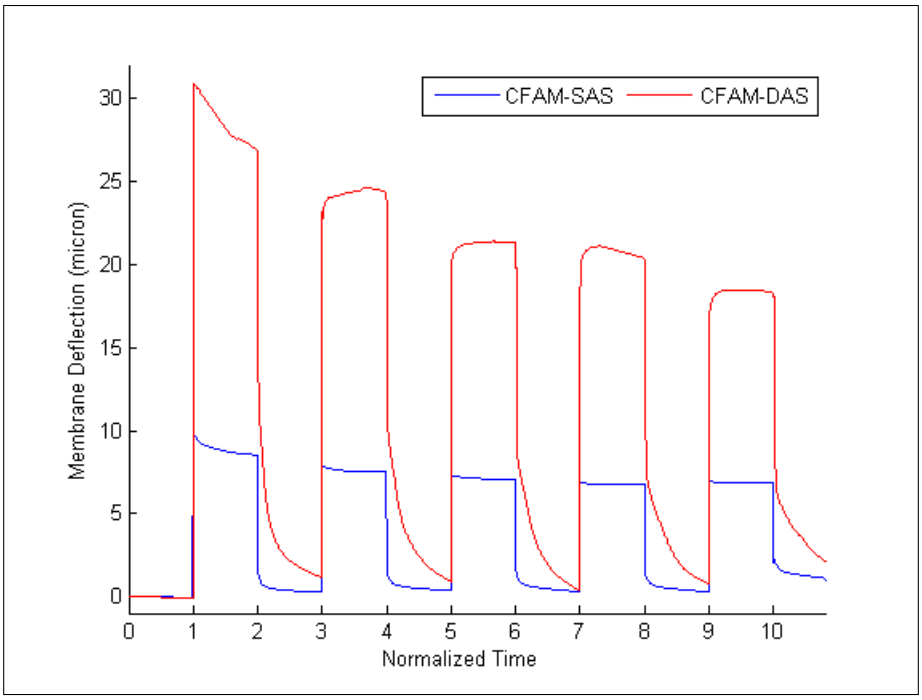

Figure 5.2: Comparison of displacement curves between CFAM-SAS and CFAM- DAS Devices

had remained at its sessile value during electrowetting. As the table indicates, in most of the tests the pressure change is significantly less due to the wetting hysteresis. On average, the pressure change with hysteresis is 72% of the pressure change without hysteresis.

5.4 Comparison of CFAM SAS and CFAM-DAS.

Figure 5.2 shows a comparison between the deflections achieved during a single active surface test (A-SAS) and a dual active surface test (A-DAS). Both tests were conducted at low frequencies, however since the frequencies were different the time data has been normalized for better comparison. Table 5.4 presents detailed information about both tests. There are minor differences in several of the test parameters including bridge height, membrane thickness, membrane radius, and maximum voltage applied. However, all the differences between test parameters work in the favor of greater displacement in the SAS test (thinner membrane, shorter bridge height, larger membrane radius, and higher voltage). Nevertheless,

Table 5.4: Comparison of parameters for tests examined in Figure 5.2.

	A-SAS	A-DAS
Max Volt (V)	12	10
Input Frequency (Hz)	12	10
Bridge Height (µm)	98	116
Membrane Thickness (µm)	33	37
Membrane Radius (µm)	515	475
ΔP_c (Pa)	72	245
Measured Deflection (µm)	8.6	26.3
Theoretical Deflection (µm)	10.1	24.7

Figure 5.2 shows that the DAS test has significantly greater membrane deflection (over 200%) than the SAS test.

An examination of the calculated capillary pressures provides potential insight into the significantly greater deflection of the DAS test. The capillary pressure of the SAS test is 29% that of the DAS test, this is roughly analogous to the membrane deflection – with the SAS test's deflection being 33% of the DAS test's deflection. If the SAS test did not have the hysteresis on the passive surface, see Section 5.3, the capillary pressure of the SAS test would 49% that of the DAS test. This should result in a SAS membrane deflection roughly half that of the DAS test.

5.5 Parameter Comparison of CFAM-SAS Devices

In this section we examine direct comparisons between the measured displacements in pairs of tests where all but a single parameter are nearly the same. Due to the variation in contact angles due to hysteresis, as discussed in Section 5.3, only tests with similar pressure changes will be presented for comparison.

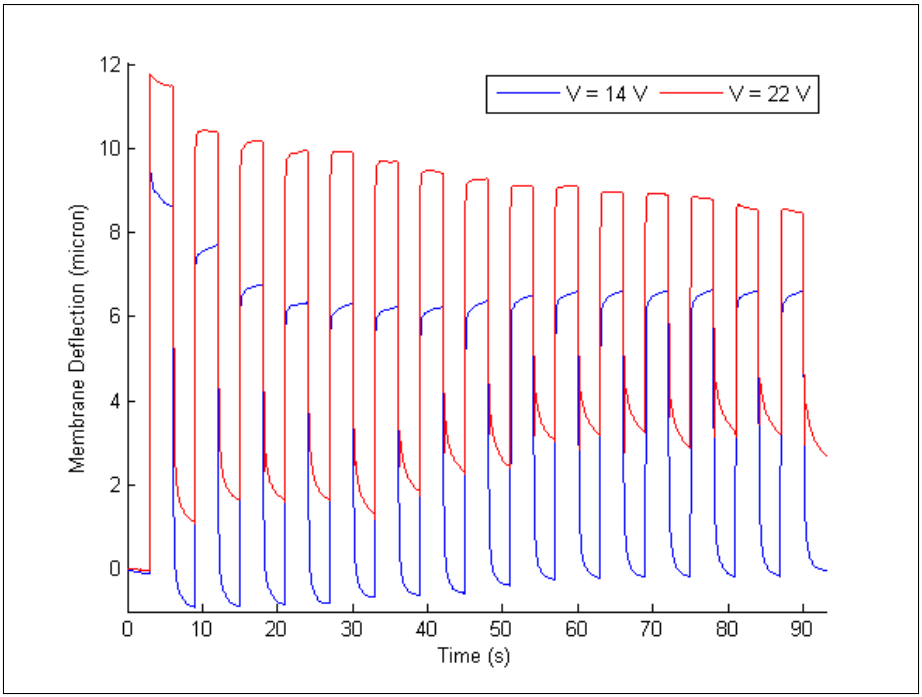

Figure 5.3: Device comparison for varied square wave voltage input.

5.5.1 Effects of Voltage Potential on the Displacement of the Membrane

Figure 5.3 shows a comparison of the membrane displacement for two SAS tests (G and K) with different applied voltage potentials (14V and 22V respectively). In each case the voltage signal is a low frequency square wave (0.167 Hz). The voltage values were chosen to sample behavior at voltages below and above the saturation voltage value.

These tests use the same active and passive surfaces, so the membrane radius and thickness are identical. The measured bridge height varies slightly (2 microns) which is attributed to human error in measurement of the side view images (3 pixels). Test K is performed after Test G so there may be some minor effects on K's behavior due of charge injection. However, this should be minimal since Test G was performed at a voltage below that associated with significant charge injection (see Section 6.3.2). The membrane in Test G displaces 8.7 µm after 14V is first applied. The magnitude of the deflecting and retracting motion decreases

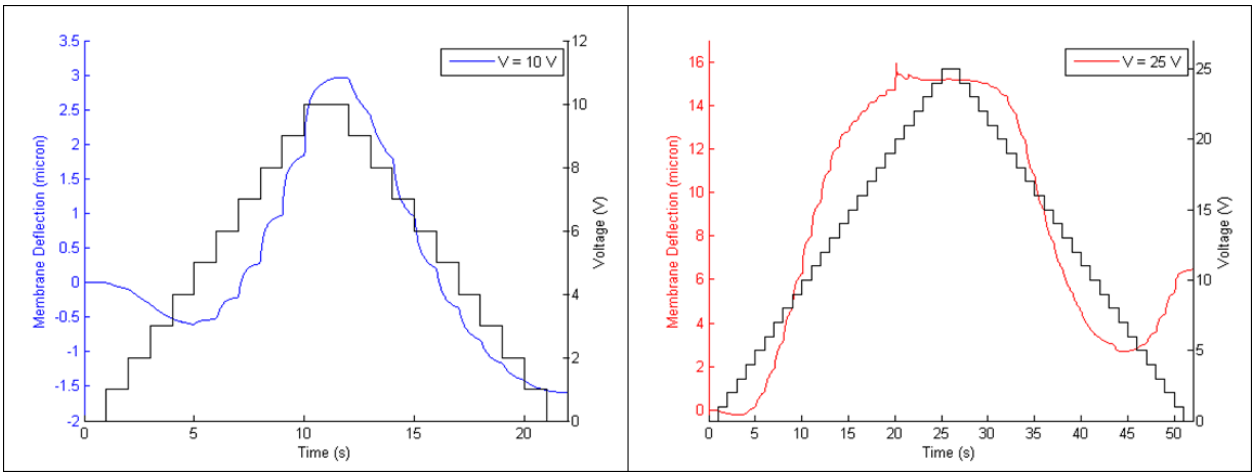

Figure 5.4: Device comparison for varied staircase wave voltage input.

somewhat with further cycles but is relatively constant during the entire test. In Test K the initial membrane deflection (11.5 µm) is 32% greater than in Test G due to the larger applied voltage. There is, however, a significantly greater change throughout the test in the deflecting and retracting cyclic behavior than was seen at lower voltage; this is due to much stronger charge injection into the active surface.

A second comparison of tests examining the effects of applied voltage potential on membrane displacement is provided in Figure 5.4. Tests L and M are both driven by staircase waves with maximum voltages of 10V and 25V respectively. Test L has a peak displacement of 3.0 µm while Test M achieves a displacement of 9.2 µm, an increase of 206.7% with 150% increase in applied voltage. Both tests use the same upper surface and membrane, but the active surface and droplet are new in Test M. Thus, there can be no residual charge injection in the active surface for Test M from the previous test. It should be noted that Test M exhibits charge injection effects after it is brought to its peak voltage. This can be seen in the unusual increasing deflection as the voltage is decreased from ∼5V to 0V.

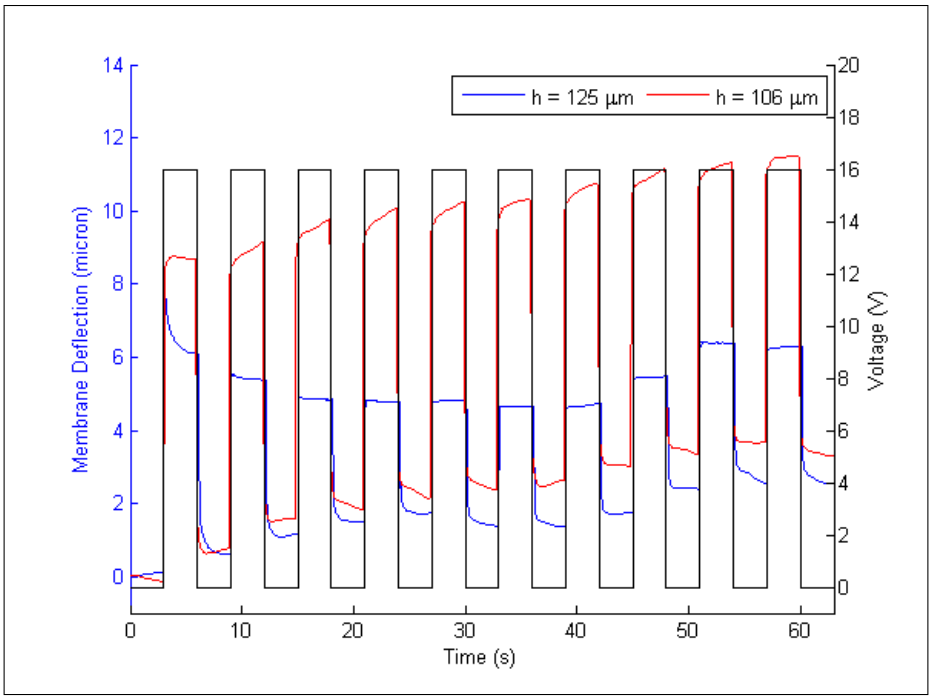

Figure 5.5: Comparison of devices with varied bridge height, with a below CAS input square wave.

5.5.2 Effect of Bridge Height on the Displacement of the Membrane

Figures 5.5 and 5.6 illustrate the effect of bridge height on the membrane displacement in SAS tests. Figure 5.5 presents results for voltages below that associated with contact angle saturation (Tests B and F). Figure 5.6 presents results for higher voltage (Tests I and J).

The first comparison, tests B & F, is performed with an applied voltage of 16V, below the saturation voltage for the presented devices. The differences in the membrane parameters for the two tests are negligible. Test B has a bridge height of 125 micron while Test F has a smaller bridge height, 106 microns. It is therefore to be expected that Test F should have larger membrane displacement. This is, in fact, the behavior seen: the deflection in Test F is 7.3 µm while it is 6.0 µm in Test B. and 7.3 µm respectively. The improvement seen is somewhat less than one would expect from theory. Both tests show significant variations in membrane displacement with repeated cycling; this may be due to significant variations in

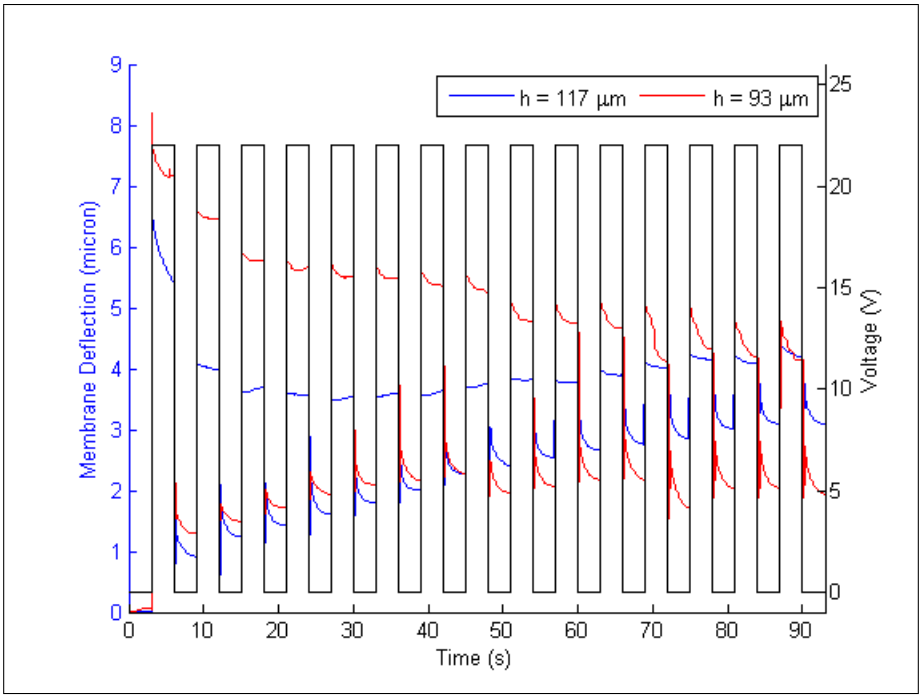

Figure 5.6: Comparison of devices with varied bridge height, with an above CAS input square wave.

angles on the passive surface during testing.

Tests I and J offer a second comparison of the effect of bridge height in SAS tests. These tests are performed at 22V, above the voltage associated with contact angle saturation. Tests I and J use the same passive surface and membrane; the active surface and droplet are new in Test J. Test I and J have bridge heights of 117 µm and 93 µm respectively.

In the first actuation cycle the membrane displaces 5.4 µm in Test I and 6.7 µm in Test J. A 24 µm decrease in bridge height results in a 1.3 µm increase in membrane deflection. The magnitude of the effect is not much different than was observed in the previous pair of comparison tests.

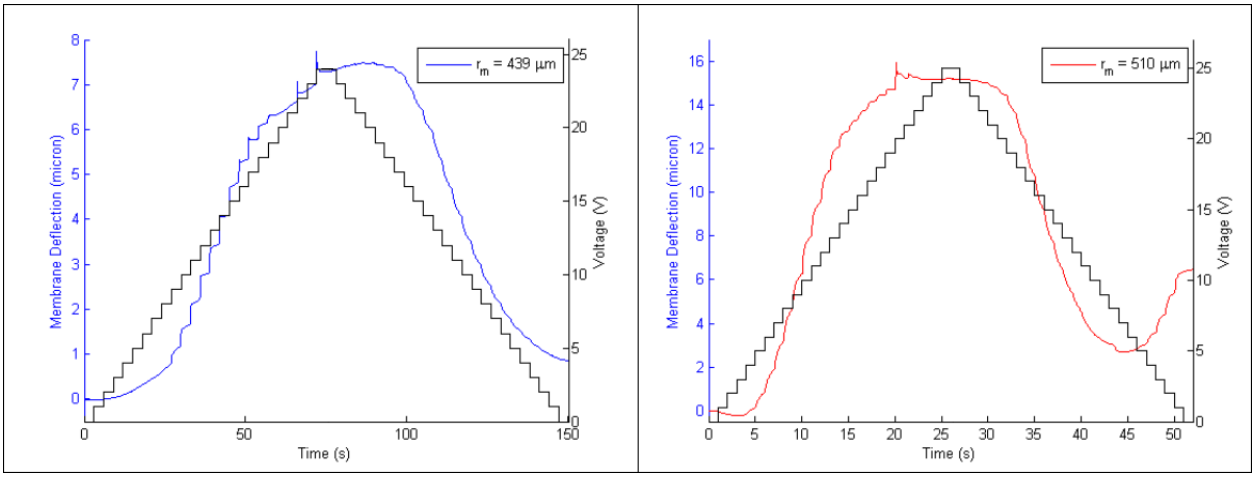

Figure 5.7: Comparison of tests with different membrane radii. Tests O (left) and Test M (right).

5.5.3 Effect of Membrane Radius on the Displacement of the Membrane

Figure 5.7 present a comparison of two tests with different membrane radii, Tests O and M. The applied voltage potential is staircase wave with the maximum voltage above that associated with saturation. Test O has a maximum potential of 24V and the step duration of 3 seconds; Test M has a maximum potential of 25V and the step duration of 1 second. It should be noted that Test M has a thicker CYTOP layer than Test O, 2 spins of 2% wt. rather than 1 spin of 1% wt., but both tests have reached the saturation angle at the point of comparison. Furthermore, the differences in capillary pressure change between the two tests are small; they vary by only 22 Pa. The differences between the bridge heights and membrane thicknesses between the two tests are negligible. Thus, we may attribute the differences in membrane deflection that occur in this comparison to the difference in membrane radii.

Test O has a membrane radius of 439 µm and displaces 7.3 µm. Test M has a membrane radius of 510 µm and displaces 15.2 µm. Thus, a 16% increase in membrane radius may be viewed as yielding more than a 100% increases in deflection. The effect of membrane radius on achieved membrane deflection is quite similar to that seen in Chapter 4 for dual active

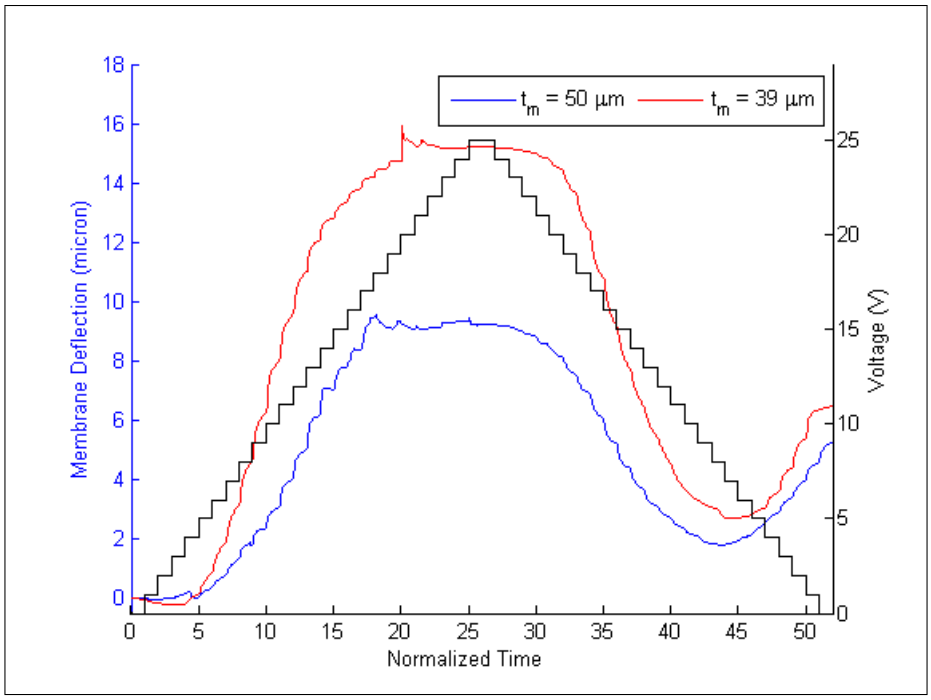

Figure 5.8: Comparison of tests with varied membrane thickness, 25V staircase wave. Time is normalized due to different durations of steps employed in the two tests.

surface devices, as expected.

5.5.4 Effect of Membrane Thickness on the Displacement of the Membrane

Figures 5.8 and 5.9 illustrate the effect of membrane thickness on the achieved deflection of the membrane in SAS tests. The two comparisons provided are (1) Test M vs. Test Q, Figure 5.8; and (2) Test H vs. Test K, Figure 5.9. In both comparisons the voltages employed are above that of contact angle saturation. In Figure 5.8 both tests have a staircase wave voltage applied, but the results are presented in terms of normalized time, since Test B employed a 1 second step duration and Test F employed a 3 second step duration. In Figure 5.9 both tests have a low frequency square wave as the applied voltage.

In the first comparison, see Figure 5.8, the membrane radii are identical and bridge heights are nearly so. The device in Test Q has a thick membrane (50 µm) while that

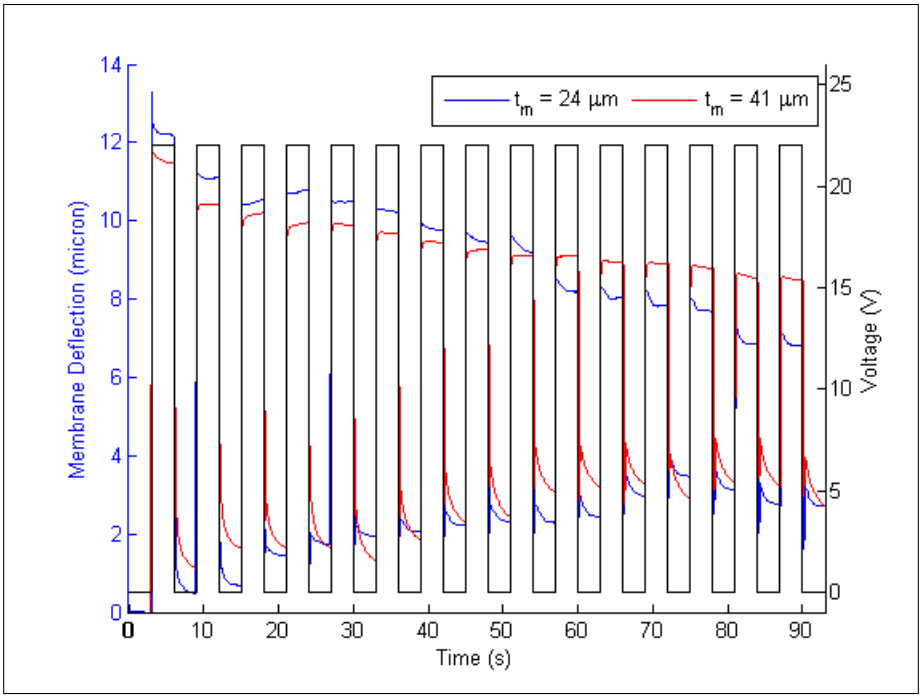

Figure 5.9: Comparison of tests conducted on devices with varied membrane thickness, 22V square wave input.

used in Test M is significantly thinner (39 µm). The displacement achieved by the thinner membrane device was much larger as Figure 5.8 shows, 15.2 µm vs 9.2 µm.

In the second comparison, Tests H vs. Test K, the devices are driven by a square wave voltage signal. The devices have identical membrane radii, and the bridge height difference is negligible. The device in Test K has a membrane thickness of 41 µm while that employed in Test H has a thickness of 24 µm. The membrane displacements during the first actuation cycle in this comparison, however, are quite similar, 11.5 µm (K) and 12.6 µm (H). The effect of membrane thickness is relatively small in these comparisons and is likely dominated by the effect of uncontrolled variables (e.g., passive surface hysteresis). A complicating factor when comparing results with different membrane thickness is the increased Young's modulus for thinner PDMS layers that was commented upon in Chapter 4. The thin membrane in Test H may have a modulus about 15% greater than that of its thicker counterpart in Test K. As Figure 5.9 shows, the devices in both Test H and Test K have significantly reduced actuated motion (both deflection and retraction) with repeated cycles. As these tests were

done at larger voltages this result is due to charge injection into the dielectric layer of the active surface.

Chapter 6

Dynamic and Dielectric Performance Results

This chapter will discuss the dynamic and time-varying aspects of the actuating behavior of both the single active surface and dual active surface devices. While this thesis is primarily focused on the static performance of these actuators, some trends in the dynamic behavior were pronounced and are worthy of discussion as an invitation for future investigation.

We begin by introducing some nomenclature for describing the movement of the membrane. When the potential is applied and the membrane displaces away from its rest (0V) position and toward the direction of the liquid bridge, this phase of actuation will be referred to as the *deflection* phase. When the voltage potential is removed and the membrane moves from its deflected position toward its rest position this will be referred to as the *return* phase.

6.1 High Frequency Performance

In the interest of investigating the suitability of the actuation approach for applications requiring repeated actuation at higher frequency (e.g., micropumps), prototypes were driven by square wave signals of varying frequency. The static performance results discussed in Chapters 4 and 5 used square waves with the frequencies chosen such that transients would

Table 6.1: Details of high frequency tests conducted.

Test	Bridge Height (µm)	Membrane Thickness (µm)	Membrane Radius (µm)	Max Volt (V)	Input Frequency (Hz)	Test # on Assembly
R-SAS	∼ 150 to 175	30	438	18	0.167	1
S-SAS	∼ 150 to 175	30	438	18	1	1
T-SAS	∼ 150 to 175	30	438	25	0.167	1
U-SAS	∼ 150 to 175	30	438	25	1.0	2
V-SAS	∼ 150 to 175	30	438	25	5.0	3
C-DAS	67	47	474	10	0.167	1
K-DAS	66	47	474	10	5.0	2

All voltage inputs are square waves.

decay during each "on" and "off" stage of an actuation cycle and an equilibrium position would be reached (typically frequencies from 0.05 to 0.1667 Hz were chosen). In the tests discussed herein, summarized in Table 6.1, we examine actuator performance at higher frequencies where the transient may not have had sufficient time to decay before the next switch in the voltage signal. In these tests the applied voltage potential was cycled between 0V and a value chosen based on the dielectric layers used, this voltage corresponding to a value just below (18V) or above (25V) that of contact angle saturation (CAS). The CFAM-SAS tests use the same actuator, the membrane thickness is 30 µm, membrane radius is 438 µm, and the bridge height between ∼150-175 µm, a low deflection device. The image quality of the capillary bridge is poor for these tests, therefore theoretical predictions are not possible and the device is not included in Chapter 5.

Figure 6.1, presents the comparison of the CFAM-SAS device tested at two different square wave frequencies, 0.167 Hz (R-SAS) and 1 Hz (S-SAS), at 18V. The tests use separate assemblies – reassembly may result in a slight variation in bridge height but there is no residual charge injection from previous tests. It is to see easy in the 1 Hz response that the deflection and return transients have a different characteristic time in each cycle. This is not as clear in the response to the lower frequency square wave because these transients are much smaller than the fundamental period. A possible reason for the small difference

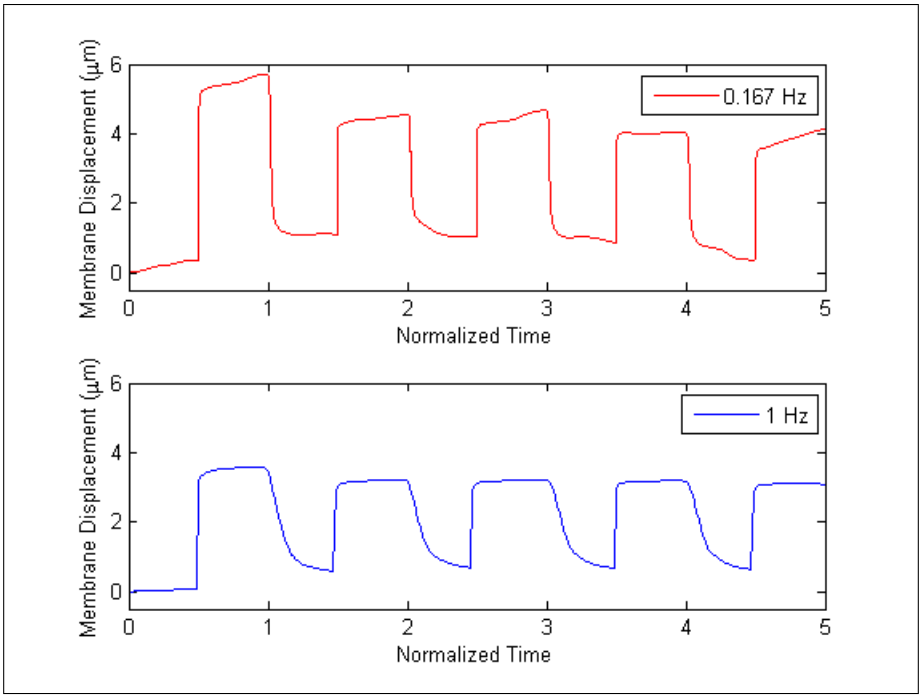

Figure 6.1: Comparison of SAS actuation performance at two frequencies (R-SAS & S-SAS), time normalized by square wave period. (18V square wave, below CAS).

in deflection could changes in the capillary bridge height, or surface contamination between assemblies – the lesser deflecting test was performed on the later assembly.

Figure 6.2 presents a comparison of the same actuator device tested with a 25V square wave input at three frequencies: 0.167Hz (T-SAS), 1Hz (U-SAS), and 5Hz (V-SAS). This series of tests are performed sequentially on the same assembly, therefore there may be residual charge injection effects. However, the device utilizes a the thicker – 2 spin coat applications of 2% wt. – CYTOP layer where charge injection effects are minimal, see Section 6.3.2. Nevertheless, the charge injection could be the cause for the smaller deflection on each subsequent test. As in the previous figure, the time is normalized by the square wave period. These results are for a device with a large bridge height (∼150-175 µm) and moderate membrane radius (438 µm), and therefore low deflections can be expected even at low frequencies. The figure shows that as the frequency increases that the amplitude of the swing in membrane deflection is significantly reduced. This decrease is primarily due

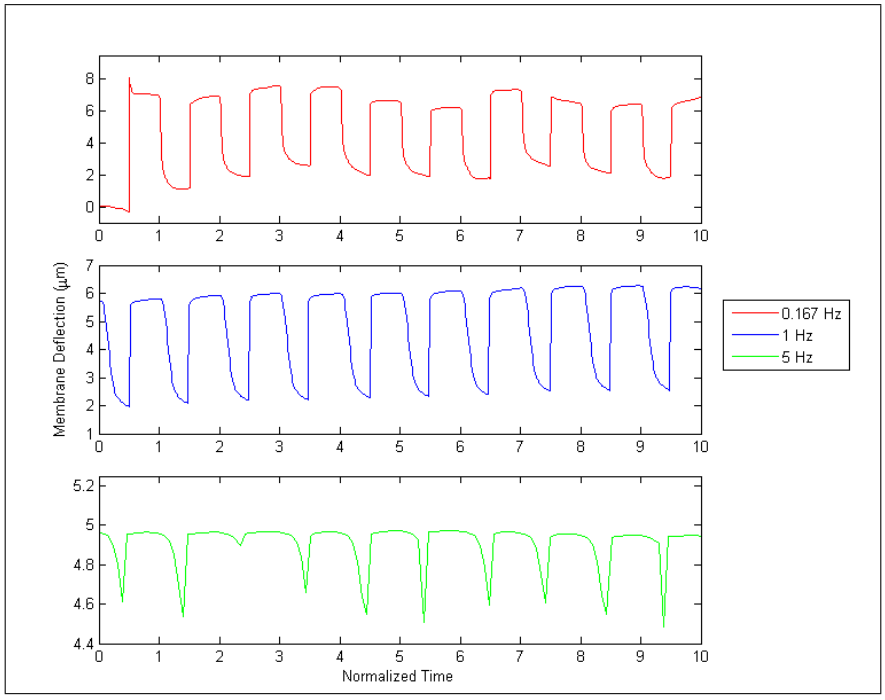

Figure 6.2: Comparison of SAS actuation performance at three frequencies - 0.167 Hz (T-SAS), 1 Hz (U-SAS) & 5 Hz (V-SAS), time normalized by square wave period. (25V square wave, above CAS). Note that deflection scales are not equal in subplots so that greater detail can be seen in higher frequency plots.

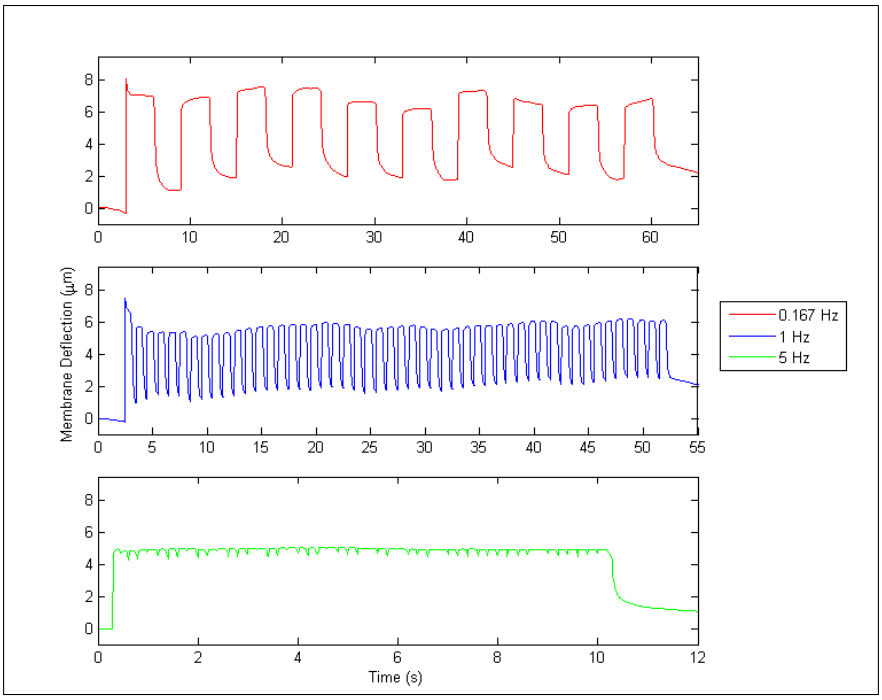

Figure 6.3: Above CAS (25V) frequency comparison of a CFAM-SAS device at 0.167 Hz (T-SAS), 1 Hz (U-SAS), and 5 Hz (V-SAS) plotted against real time.

to the incomplete transient during the return phase of the actuation cycle. As the square wave frequency was increased the duration of the return phase is shortened, resulting in an incomplete return to the 0V membrane position. There could be several causes to this behavior, including fluid dynamics, electrowetting behavior, nonlinear membrane stiffness, and charge injection into the CYTOP dielectric. Presently, the side-view imaging system has insufficient frame acquisition frequency (∼1Hz) to allow for exploration of the nature of the cause. Unraveling this phenomenon is left as a topic for future investigation.

The entire data set of the tests presented in Figure 6.2 is shown in Figure 6.3, this time without normalizing the time axis. The 5Hz case is particularly interesting. The membrane displacement undergoes a nearly 5 µm shift in the first deflection phase. This is followed by a return phase that is so incomplete that the swing in membrane deflection is quite small in all subsequent cycles until the conclusion of the test when the voltage returns and remains at 0V. At this time the membrane completes its return phase and retracts close to its position

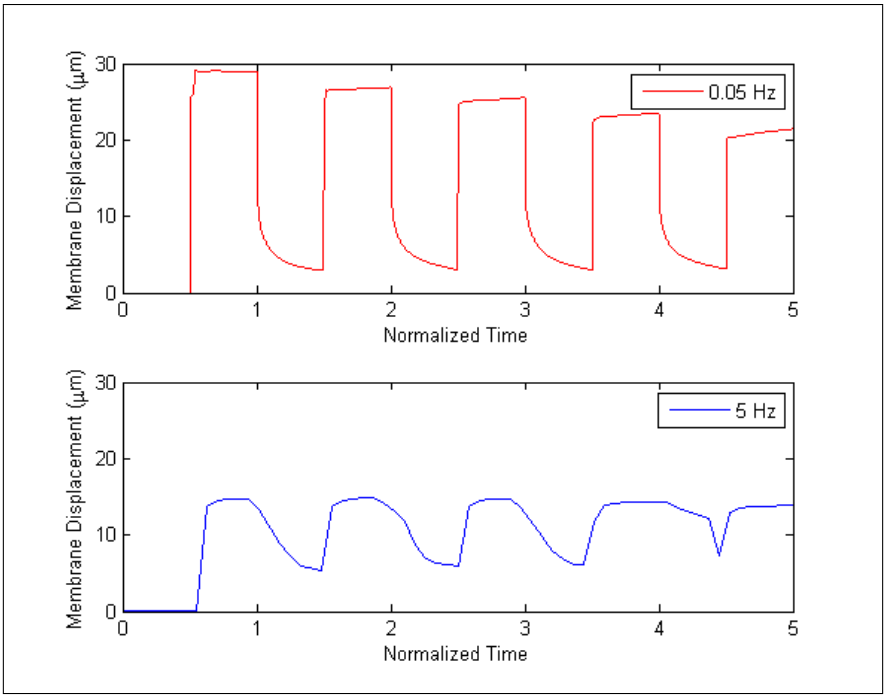

Figure 6.4: Comparison of low and high frequency square wave response of a dual active surface device, C-DAS (0.05 Hz) & K-DAS (5 Hz), below CAS voltage (10V). Time normalized by square wave period.

at the start of the test. Some residual membrane deflection remains, most likely due to charge injection.

As described early, the devices examined so far are prototypes with low static deflections. Let us now examine the dynamic performance of dual active surface device with significantly greater static deflection at low voltage. The tests compared are Test C-DAS and Test K-DAS (see Section 4.1). The device used here has a bridge height of 67 µm, a membrane thickness of 47 µm, and membrane radius of 474 µm. At low frequency the membrane is able to achieve close to 30 µm of displacement with 10V applied. At 5Hz the membrane achieves considerably less swing than at low frequencies, moving an average of 7.4 µm between the deflection and return phases of its cycle. This swing is much larger percentage of the static deflection (25%) than that for the device examined in Figure 6.2 (< 5 %). It is thought that the presence of electrowetting on both the upper and lower surfaces in DAS devices enhances the closing rate; the cause may be either the fluid mechanic response with DAS or

the nonlinearity of membrane's elastic deformation in the case of greater deflection occurring in DAS. The reader should note that the deflecting phase of the actuation cycle achieves only half the motion at 5Hz that it did at 0.05 Hz. This cannot be due to the time constant of the return phase of the cycle as it appears in the very first cycle of Figure 6.4. Instead, the deflection phase of actuation appears to have been incomplete before the square wave voltage switched to zero for the return phase. (Since the voltage is low in this test charge injection is not expect to contribute to the observed behavior.) Further investigation is needed to determine the mechanisms of this behavior.

6.2 Transient Behavior of Membrane Deflection

To better understand the transient behavior of the actuation cycle discussed in Section 6.1, a preliminary analysis of the collected data was conducted. As described in the previous section the deflection phase and the return phase of the actuation cycle appear to have two different time constants. The deflection phase consists of a very quick motion to a displaced position while the return phase has a much longer transient. It is the later, more limiting, transient that we will focus on in this section.

The return transient of dual active surface devices that is analyzed here. The input signal in all cases is a low frequency square wave. The behavior of the membrane displacement is examined in the period immediately following the switch of the voltage back to 0V in the return phase of each cycle. For comparison of the performance of various devices the displacement in return phase is rescaled as follows:

$$X_n = \frac{X - X_\infty}{X_1 - X_\infty} \tag{6.1}$$

where X_n is the rescaled deflection (unitless), X is measured deflection during the return phase; X_1 is fully deflected (equilibrium) position immediately prior to the start of the return phase; and X_∞ is final position at the end of the return phase.

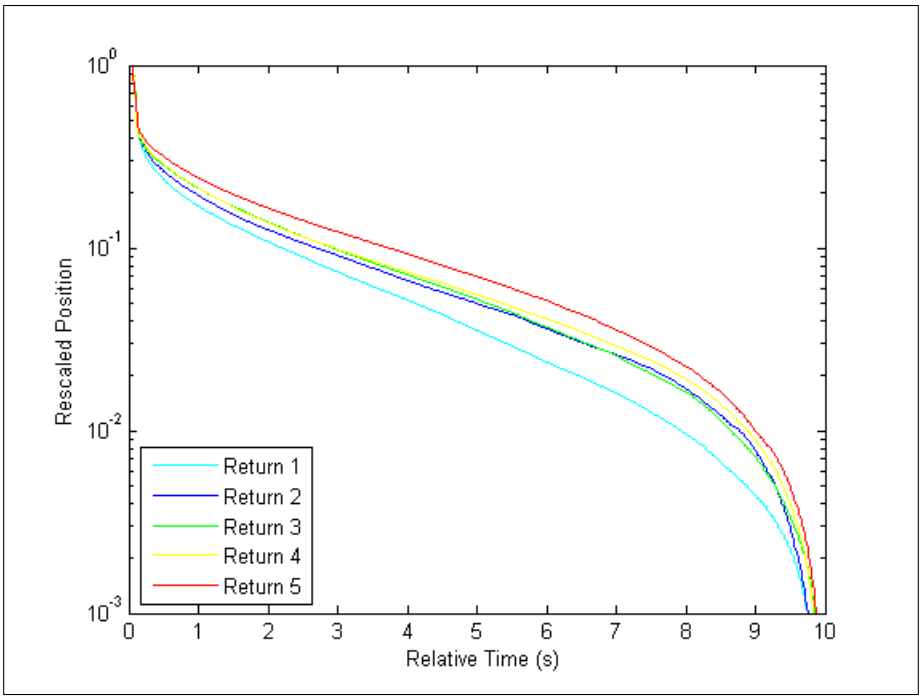

Figure 6.5: Rescaled membrane deflection transient for the return phases of several actuation cycles. Test C-DAS (h=72 µm , t_m=46 µm, r_m= 474 µm, 10V square wave at 0.05 Hz.)

To accompany the rescaled deflection, we will define a nondimensional measure of the actuation cycle – the return – deflection ratio, ζ:

$$\zeta = \frac{\text{return phase displacement}}{\text{deflection phase displacement}} = \frac{X_1 - X_\infty}{X_1 - X_0} \tag{6.2}$$

where X_0 is the position of the membrane immediately before voltage is applied in the first actuation phase. If ζ is equal to 1, the membrane has returned to its position at the start of the actuation cycle.

Figure 6.5 provides an example of rescaled return transient curves for Test C-DAS. A semilog scale is used for position and time axis displays the time since the start of the particular return phase. The transients are displayed for the first five return phases in this test. Ideally, the rescaled return curves should be the same from cycle to cycle, but there is a subtle but distinct trend in the results; this is most likely due to charge injection. There are two distinct time scales to the transient response: a large return motion that occurs very

Table 6.2: Transient properties of CFAM tests.

Test	Return time (s)	τ (s)	ζ
A-DAS	10	2.65 (0.27)	0.95
B-DAS	10	2.66	1.02
C-DAS	10	2.56	0.9
E-DAS	10	2.81	0.86
F-DAS	10	3.42	0.83
G-DAS	10	2.71	1.02
H-DAS	10	3.64	0.92
I-DAS	10	3.86	0.47
A-SAS	3	1.02 (0.34)	0.97

Return time is set by the voltage input frequency.
Normalized τ values are in parenthesis.

quickly, mostly within 0.5 second after voltage switches to 0V, and a much slower exponential decay that occurs over the remainder of the return. (The final very rapid decrease in each transient is an artifact of the manner in which the position was rescaled and can be ignored.) It is this exponential decay portion of the return phase that we will seek to characterize. This portion of each transient curve appears as a straight line segment; the slope of this line then yields the time constant (labeled τ) of the exponential decay.

Generally – as presented in the Figure 6.5 – the subsequent transients are slower and return less of the deflection distance over the return phase. Each subsequent return tends to have a somewhat larger time constant, τ. Because of the tendency of drops to shift after the first actuation cycle we will focus our examination on the time constants appearing in the very first return phase of actuation. Tests where strong charge injection was suspected to occur (D-DAS and J-DAS) were not included in this analysis.

The exponential decay during the first return phase of each transient was fitted to find the time constant associated (i.e., a least squares fit of the linear segment). The duration of the return phase of actuation is 10 seconds, as set by the 0.05 Hz square wave input signal. The time constants of the analyzed return phases, τ, ranged from 2.5 to 4 seconds. Table 6.2 gives the calculated τ and ζ values. Two general trends were observed, both associated with the voltage of the square wave used.

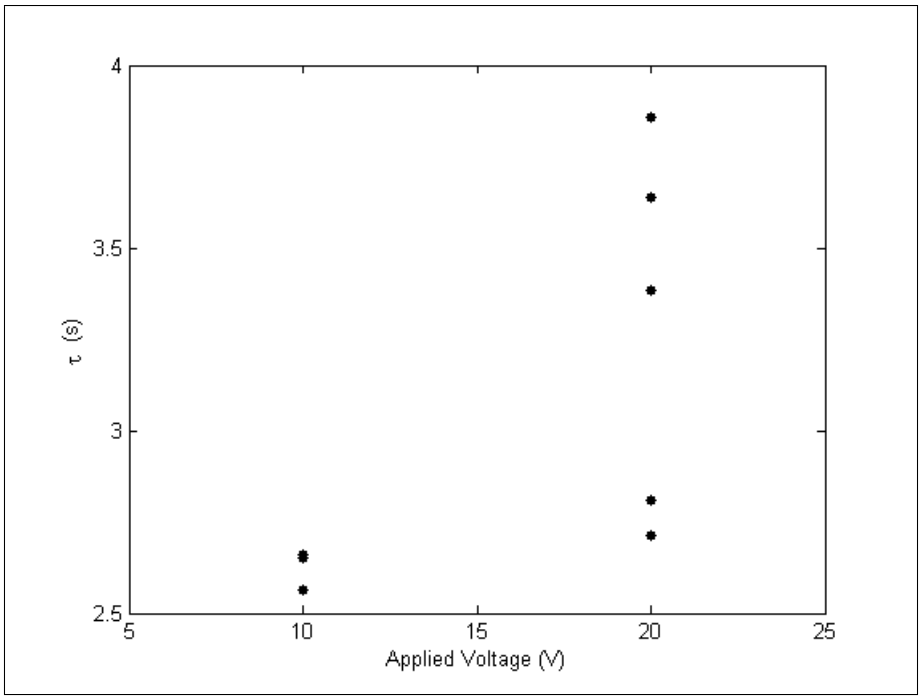

Figure 6.6: The effect of applied voltage on the return phase time constant, τ.

Figure 6.6 shows the return phase time constant as a function of voltage applied. All time constants determined for 10V tests showed smaller values (~2.7 seconds); when 20V was applied the time constants found were more varied and generally larger, with values up to 3.9 seconds.

Figure 6.7 illustrates the relationship between the return-deflection ratio, ζ, and the time constant τ. In general, when the ratio is high the time constant tends to be lower.

The results of Figures 6.6 and 6.7 suggest that the variations seen in return phase time constant is related to the completeness of the dewetting process. Charge injection can result in a residual electric field after voltage is removed; this field would both slow the dewetting (capillary pressure increases less in the retreat phase) and prevent the return of the membrane to its original position (ζ is close to 1). Where ζ is greater than 1 may be a result of drop shifting or minor evaporation prior to the start of the test – which lowers the static equilibrium angle.

When charge injection is minimal dual active surface devices should generally have shorter

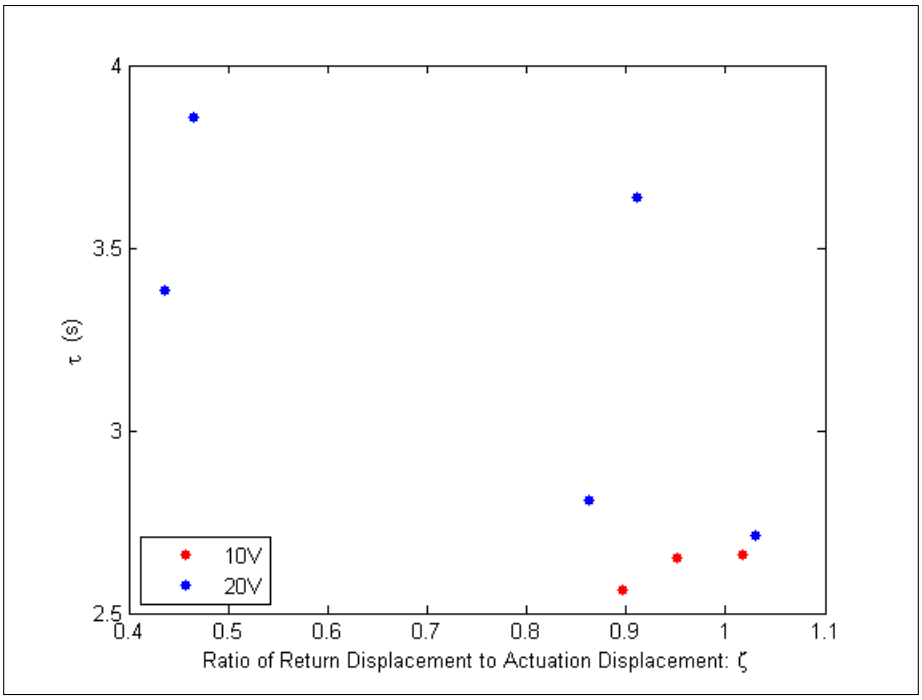

Figure 6.7: The relationship of return phase time constant, τ, to the return-deflection ratio, ζ.

return phase time constants than single active surface devices since dewetting is occurring on both surfaces and pressure changes are greater. This is demonstrated by normalizing the return positions and times of the A-SAS and A-DAS, since the voltage inputs have varying frequencies. Test A-SAS has a normalized return time constant of 0.34, while A-DAS has a normalized return time constant of 0.27.

6.3 Repeatability of Actuation and Charge Injection.

It was observed in square wave input tests of the devices that the first actuation phase produced the largest displacement of the membrane; subsequent actuations showed reduced absolute displacement. It is believed that charge injection and increased contact angle hysteresis with repeated cycling are the dominant factors behind this loss in performance. Steps were taken to minimize hysteresis, but it was observed in several cases after re-assembly and reuse of a device.

Charge injection is not as easily prevented as hysteresis due to the electret nature of CYTOP. For CFAM-DAS devices there will be residual embedded charge in the CYTOP layer on the top plate for any test subsequent to the first test (perhaps even subsequent to the first actuation cycle). It is demonstrated in the section below that the charge injection effect is minimal for voltages well below that associated with contact angle saturation. To minimize the embedded charge, tests at higher voltages are never performed on a device before the conclusion of low voltage tests. The following results present a strong case for charge injection affecting the actuator behavior during repeated actuations.

6.3.1 Loss of deflection phase motion over repeated actuation cycles

To better illustrate the loss of motion during the deflection phase in each actuation cycle we will define a normalized deflection ($\widehat{D_i}$) as follows:

$$\widehat{D_i} = \frac{D_i}{D_1} \tag{6.3}$$

where D_i is the displacement during the deflection phase of actuation cycle i and D_1 is the displacement during the first deflection phase. This normalization allows for the straightforward comparisons of the deflection loss across all devices. Figure 6.8 and 6.9 presents the normalized deflecting phase displacement for CFAM-DAS tests (square wave input only) introduced in Section 4.1. It can be seen that for tests conducted at lower voltages, Figure 6.8, the loss in deflection is fairly consistent across tests and linearly decreasing over the first few cycles. The presented tests, which concluded after 5 actuations, final normalized deflection being an average of 69% of the first normalized deflection. The consistent decrease is consistent with the notion that some additional charge is being embedded with each subsequent cycle of actuation. It is expected that the deflection will continue to decrease for subsequent cycles until the no additional charge is able to embed into the Layer.

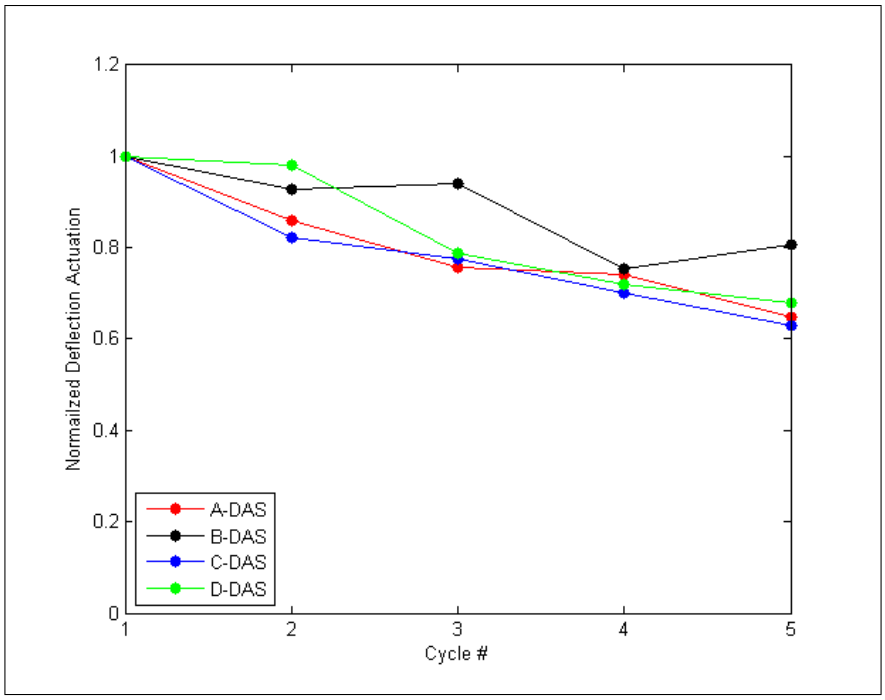

Figure 6.8: Normalized deflection phase displacement plotted against cycle or period, for below CAS voltage test (10V).

Figure 6.9 presents a similar deflection loss curve for tests at higher voltages (above that associated with contact angle saturation). The normalized deflection phase displacement curves are less repeatable than the low voltage case. Three trends were observed in the behavior corresponding to three physical phenomena. In the first trend the deflection loss behavior is fairly uniform and linear in its decrease (E-DAS, F-DAS), similar to that in Figure 6.8. An example of the displacement signal during actuation is shown in Figure 6.9B.

The second trend is observed in those case where there are multiple large liquid bridge shifts during actuation (G-DAS, H-DAS). The lateral shift of the bridge allows part of the bridge to wet a "fresh" surface, where no previous wetting, hence charge injection, has occurred. It is theorized that the shift allows the deflecting phase actuation to displace a similar distance to that it achieved in the first actuation phase – see Figure 6.9C. Thus the loss of deflection phase motion is much less severe in these cases than seen in Figure 6.8. We would expect that once the "fresh" surfaces are exhausted the deflection loss will follow a

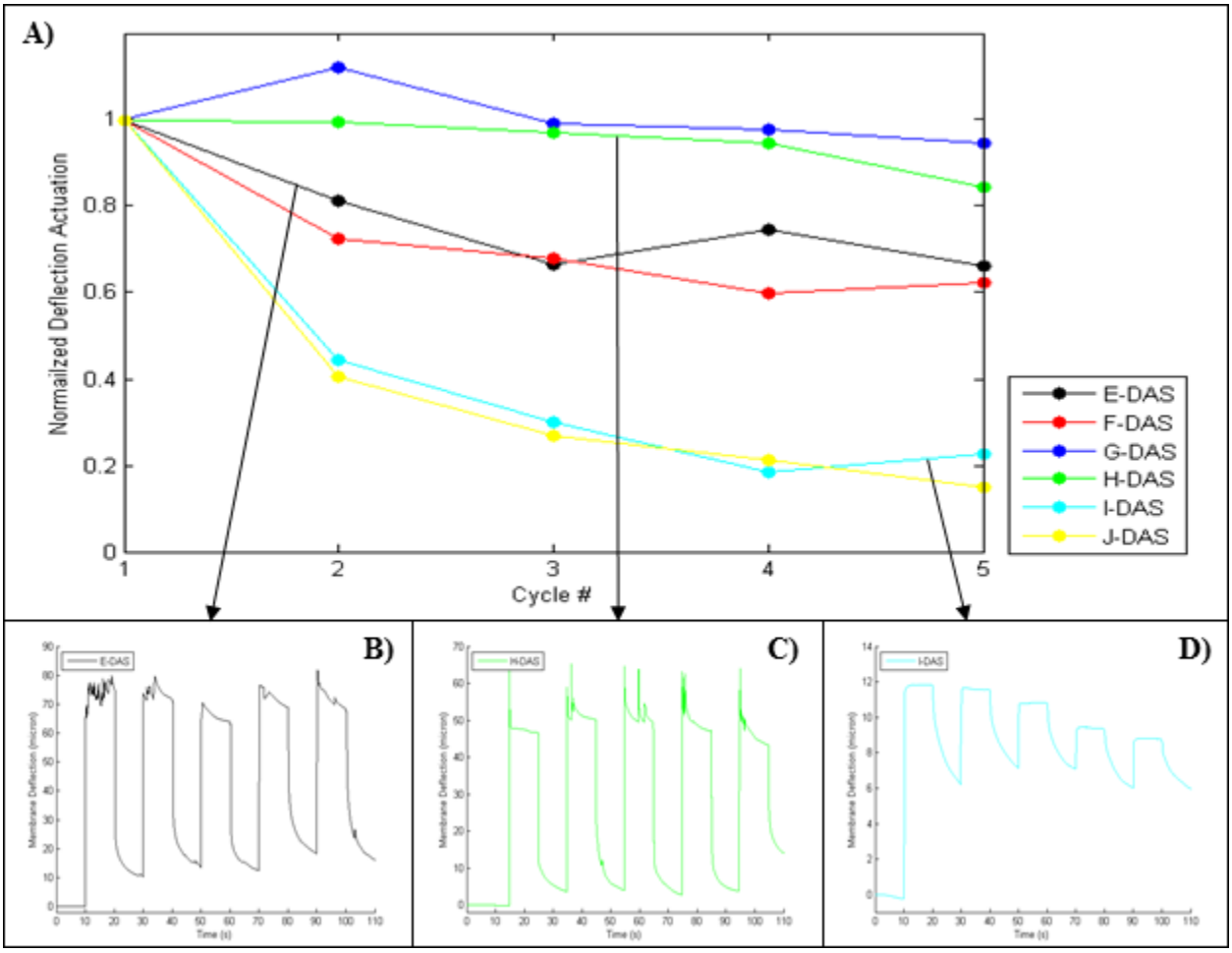

Figure 6.9: A) Normalized deflection phase displacement plotted against cycle for 25V square wave tests. B) Displacement response of a device with uniform wetting (E-DAS). C) displacement response of device with drop shifting (H-DAS). D) displacement response of a device with severe wetting hysteresis (I-DAS).

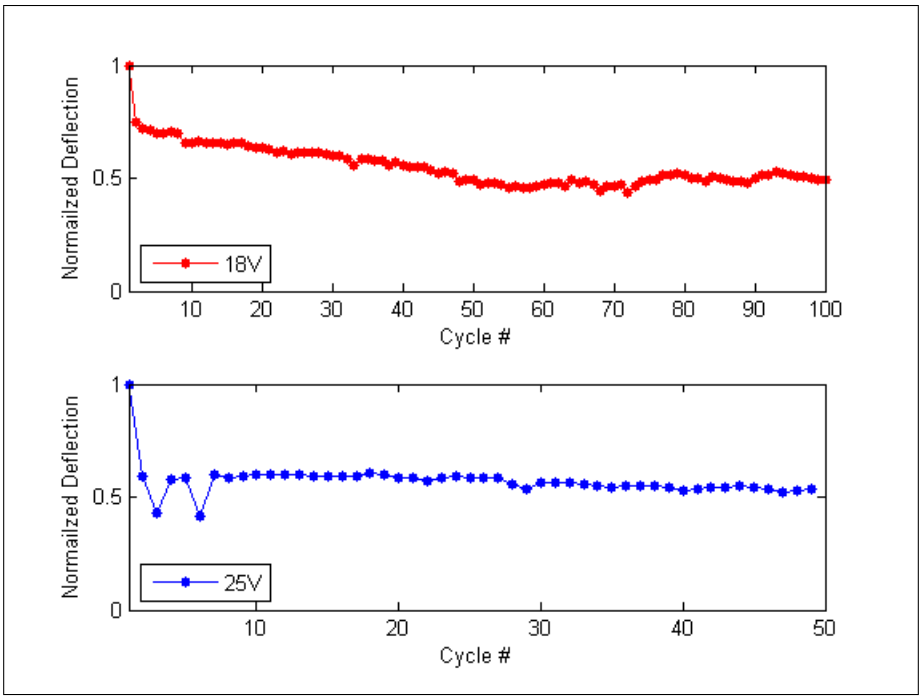

Figure 6.10: Normalized deflection phase displacements for 1Hz square wave tests of SAS devices. Note that the 25V (U-SAS) case presents data from 50 actuation cycles while the 18V (S-SAS) case shows data from 100 cycles.

trend similar to the low voltage case.

In the third observed trend (Tests I-DAS and J-DAS) the loss in deflection phase motion is quite severe, with most of the loss occurring after the first actuation cycle – see Figure 6.9D for an example. It is conjectured that this behavior is due to wetting hysteresis on the Cytop surfaces. As shown in Figure 6.9D, the membrane fails to return the majority of its initial deflection phase motion in the first cycle. Subsequent deflections phase motions decrease more slowly in a fashion similar to the Figure 6.8. It is unclear why these prototypes were more hysteretic than others tested.

Figure 6.10 presents the normalized defection for 1 Hz CFAM-SAS devices presented in section 6.1, for U-SAS above (25V) and R-SAS below (18V) contact angle saturation. The loss of deflection begins to taper off after approximately 10 cycles, especially in the above CAS case – since it is a repeated test on an assembly. This tapering could indicated that the electret nature of the surface seems to be reaching a limit in its stored potential. The

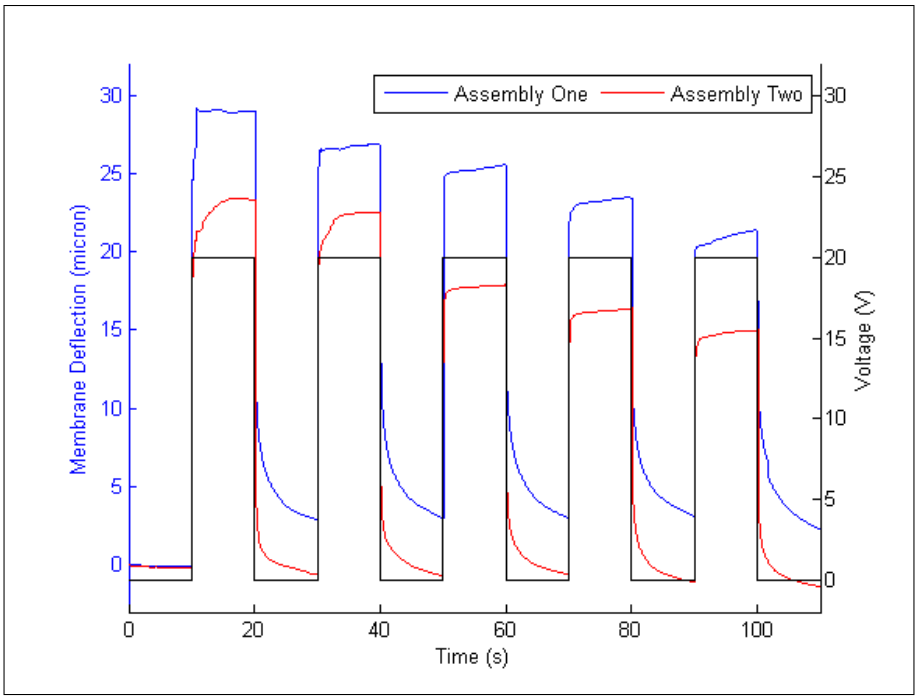

Figure 6.11: Comparison of a CFAM-DAS device tested twice utilizing a new assembly for the second test, the tests are C-DAS and D-DAS.

continued gradual deflection loss seen in the below CAS case may be a result of the fewer ions being imbedded on each actuation compared to the above CAS case.

6.3.2 Effects of charge injection on repeated tests.

Further evidence for charge injection is presented in Figure 6.11, comparison of Test C-DAS and Test D-DAS, first presented in Section 4.1. A second test (D-DAS) was performed after the first test on the device (C-DAS). Between the tests the device was disassembled and reassembled so as to provide a fresh surface for the lower active surface and a new conducting drop for the second test. The second test yielded lower static deflections than the first test. All test conditions (bridge height, membrane thickness and radius, applied voltage) are essentially the same. One difference is that the initial contact angle (prior to the application of voltage) was significantly lower on the upper surface in the second test (89° vs. 97°). Since the upper surface is the same in both tests, it is believed that embedded

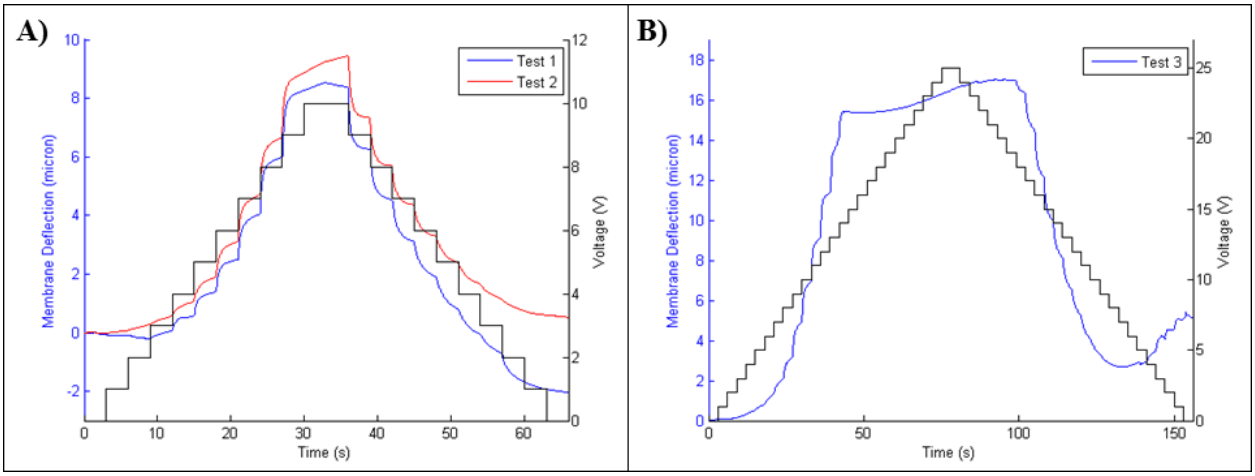

Figure 6.12: Comparison of a CFAM-SAS device utilizing the same assembly and conducting drop for each test to examine charge injection. A) Below CAS, 10V, staircase input (W-SAS & X-SAS). B) Above CAS, 25V, staircase input (Y-SAS).

charge from the first test is responsible for this lowering of the initial contact angle. (The initial contact angles on the lower surface differed slightly - 102° in C-DAS and 106° ; this is most likely due to assembly.) Overall the performance is similar between the two tests in all aspects except the magnitude of the deflection.

One particularly interesting display of embedded charge is seen in three staircase wave tests (W-SAS, X-SAS, & Y-DAS) performed on single active surface prototypes. Figure 6.12 shows the displacement signal from three successive tests. The first two tests were conducted with a maximum voltage of 10V (below contact angle saturation) while the third had a much higher maximum voltage (25V, above saturation). Each test used the same assembly and the same conducting drop, therefore changes in displacement behavior are only due to the previously applied inputs.) There are very minimal differences between the displacements recorded during the first two tests, W-SAS and X-SAS. both tests displace roughly the same distance, and return roughly the same distance; some drift in measurement may also present due to thermal effects. The limited differences in the repeated tests at voltages below contact angle saturation indicate that the effects of charge injection are likely minimal at low voltages, especially for short test durations.

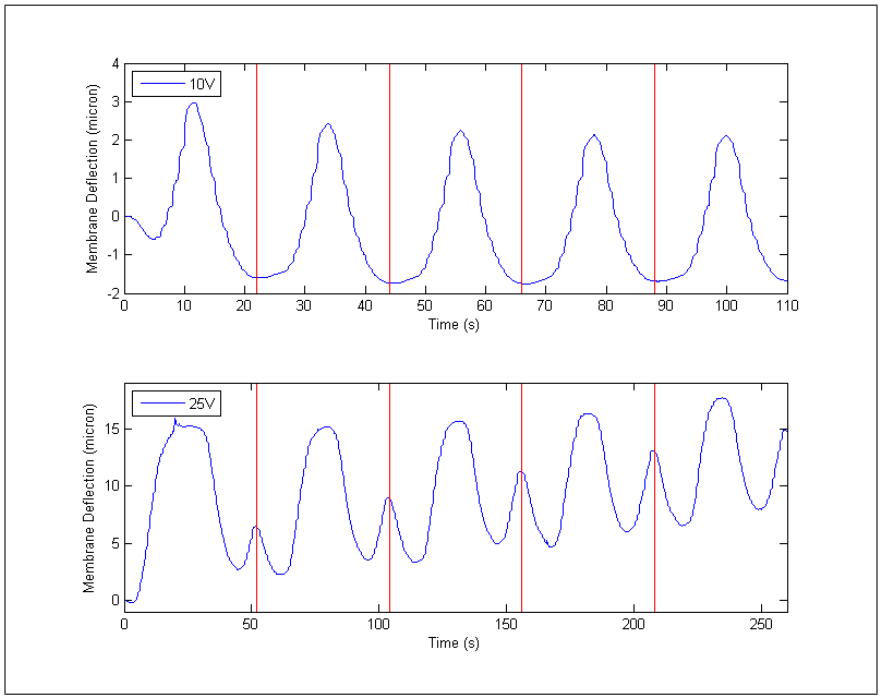

Figure 6.13: Comparison of the displacement response to repeated staircase wave inputs with low (10V, above) and high (25V, below) peak voltages. The red lines indicate the points with 0V applied. (Tests L-SAS and M-SAS).

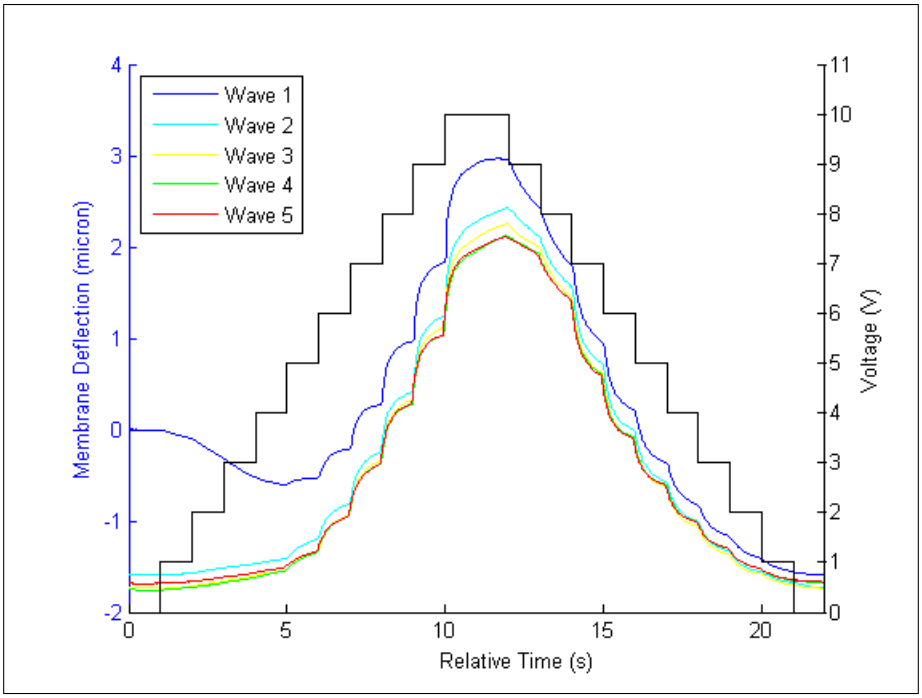

Figure 6.14: Displacement response to successive staircase waves (10V) overlaid for comparison; time is from start of cycle. (Test L-SAS).

The third test (Y-SAS), conducted with much higher maximum voltage, displaces much further than in the previous tests. It is apparent that contact angle saturation occurs at approximately 14V, after which the deflection only increases marginally. As the voltage steps backward to zero in the test the displacement decreases as expected until approximately 7V, after which the displacement begins to increase again as the voltage is lowered further. This reversal of motion in the return phase of staircase wave response is due to significant charge injection into the CYTOP. The reversal is not seen in the response to all staircase voltage inputs; it is exclusive to devices operated at higher maximum voltages and constructed with the thinnest layers of CYTOP, ($\sim$ 50 nm, fabricated by 1 spincoat application of 1 wt.% CYTOP). Thinner layers result in greater electric field in the Cytop resulting in more charge injection.

Figure 6.13 shows a comparison of two single active surface tests, each conducted with a repeating staircase wave input. In Test L-SAS (top plot) the maximum voltage is 10V.

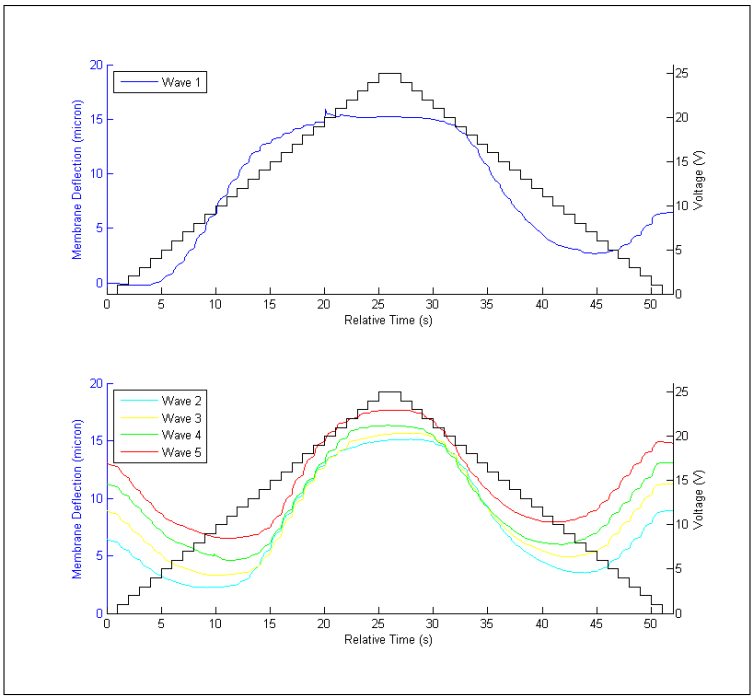

Figure 6.15: Displacement response to successive staircase waves (25V) overlaid for comparison; time is from start of cycle (Test M-SAS). First cycle of response displayed separately for ease of visual inspection.

The membrane displacement is quite repeatable over several cycles of the staircase wave. No reversal in the displacement is seen as the voltage is decreased. In Test M-SAS (lower plot) the maximum voltage is much higher (25V). The behavior here is less repeatable from cycle to cycle. There is clearly a reversal in the displacement with decreasing voltage; This reversal results in a second peak in the displacement curve which occurs each time the voltage returns to zero. The voltage at which reversal begins increases from one cycle to the next resulting in the magnitude of this second peak increasing with the number of waves. The behavior observed is highly consistent with the CYTOP layer acting as an electret due to injected charge. In Figures 6.14 and 6.15, the displacement waveforms provided in Figure 6.13 are presented again with each cycle of the staircase response overlaid so as to better illustrate the time-varying nature of the behavior in the case of higher voltage.

A comparison of the two figures clearly shows the time-varying nature of the response in the case of the higher voltage input. A close examination of Figure 6.15 shows that the

voltage where displacement reversal occurs is increasing with each successive cycle of the staircase wave; these reversals are at approximately 6V, 8V, 9V, 10V, and 10V; the electret nature of the surface seems to be reaching a limit in its stored potential.

Chapter 7

Conclusions and Future Work

This chapter summarizes and concludes the thesis and proposes future avenues for the CFAM device.

7.1 Conclusions

A new application of CFA, the capillary force actuated membrane – CFAM, was designed, microfabricated and tested in this work. A theoretical model is developed that shows, for given CFA and membrane parameters the displacement may be accurately predicted. The CFAM device can deliver significantly greater displacements than comparably sized electrostatic membrane actuators, 14.2 microns at 20V compared to 7 microns at 120V [12]. A maximum displacement of 75.7 micron is achieved at 20V, and 29.1 microns at 10V applied voltage.

A fabrication process is developed for utilizing a simple photolithography-less procedure, and high performance thin dielectric layers. A dual active surface CFAM device, CFAM-DAS, is composed of a conducting aqueous droplet in contact with three electrodes on two surfaces. The lower surface has a single electrode and consists of a glass slide upon which an aluminum film was deposited. The aluminum was anodized to provide a dielectric layer of Al2O3. This was then covered, via spin-coating, with an ultrathin film of hydrophobic

fluoropolymer (CYTOP-809). The upper surfaces consist of two glass slides, each with an electrode. The top glass slide has a laser cut hole, and has a thin PDMS layer placed on the top surface of the glass, covering the hole, to form the elastomeric membrane. The bottom surface of this slide is coated with a gold layer to form an electrode. The second glass slide of the upper surface assembly has a larger concentric hole. This allows the droplet to contact the gold electrode and membrane. The bottom of the second glass slide had an aluminum film deposited upon it, followed by a dielectric layer of Al2O3 and CYTOP, using the same procedure as the lower surface. The two slides at the top assembly are secured to each other using CYTOP as the adhesive. The prototype device was assembled after first depositing a droplet of an aqueous solution (0.1M Cs2SO4 in DI water with 10 µMol/L Fluorescein Salt) under the membrane. Controlled separation of the surfaces was achieved via microbeads spacers.

An alternative single active surface CFAM, CFAM-DAS, is also designed and fabricated. The CFAM-SAS is composed of a conducting liquid droplet extending between two electrodes. The upper surface consists of a glass slide in which a hole has been laser cut. The bottom surface was coated with a gold layer to form an electrode. A thin PDMS layer placed on the top surface of the glass, covering the hole, to form the elastomeric membrane. The lower surface is identical to the lower surface of CFAM-DAS devices.

Prior to the CFAM testing the membrane parameters are characterized via optical measurement. CFAM performance was assessed by applying voltage and measuring the displacement of the elastomeric membrane with a Fabry-Perot interferometer. Contact angles and bridge heights were determined via side-view imaging of the droplet which was fluoresced under laser illumination. Membrane displacements ranging between 12.1 and 75.7 micron are achieved by the CFAM-DAS, and a range of 3.0 to 15.5 micron is achieved by the CFAM-SAS. The experimental characterization agree with predictions from a model based on large deflection theory and Laplace pressure change. The CFAM can be optimized for even larger deflections at lower voltages.

Charge injection of the CYTOP electret is examined, and characterized to account for the loss of deflection over repeated actuations. Dynamic analysis of the CFAM shows repeatable actuation is attainable at below contact angle saturation voltages. At a high frequency of 5 Hz a CFAM-DAS device was able to displace an average of 7.4 microns.

7.2 Future Work

The following future work is proposed to improve the performance of the CFAM in terms of membrane deflection, actuation repeatability and implementation of CFAM applications.

1. The CFA portion of the CFAM may be surrounded in oil environment rather than an ambient air environment. An oil environment reduces the hysteresis, and contact angle pinning. This will allow for increased deflection via the contact angle changing at a lower voltage. Additionally, the repeatability of actuation will be improved by the reduced hysteresis and the increased speed of drop retraction.

2. Another way to improve the displacement of the CFAM is to optimize the CFA and membrane parameters. The CFA qualities may be improved by reducing the gap between two plates. Additionally, the resolution of contact angle saturation would greatly improve the deflection of CFAM. The membrane parameters may be improved by reducing the thickness of the PDMS. The Young's modulus may also may be reduced by altering the fabrication of the PDMS [66].

3. Higher frequency data acquisition may be implemented to characterize the displacement and electrowetting properties of the CFAM. High-speed cameras would allow to the imaging of the dynamic change in contact angle, or impedance spectroscopy could be measure the change in capacitance brought on by the electrowetting [39]. If higher frequency displacement data is collected the membrane dynamics could give insight into fluid dynamic motions of the conducting liquid drop and the nature of electrowetting fluid dynamics.

4. The final recommended of future work is to apply the CFAM to an application such as a microvalve to determine the further design improvements to the CFAM, and to characterize application specific qualities of the CFAM, such as max line pressure of a valve.

Appendices

Appendix A

Bottom Plate Fabrication

The bottom plate was fabricated on a soda-lime glass slide with the dimensions: 3.81cm x 7.62cm x 0.1599cm (1.5" x 3" x 1/16"). The slide may be cut in half, lengthwise, prior to fabrication with a glass cutting tool.

A.1 Standard Clean

The following procedure was the cleaning procedure unless otherwise noted:

1. Rinse with acetone for 30 seconds
2. Rinse with DI (De-Ionized) water for 30 seconds
3. Blow dry with nitrogen gun

A.2 Aluminum Deposition

1. Swab glass slide with acetone
2. Ultrasonicate in acetone than isopropyl alcohol for 5 minutes each
3. Rinse with DI (De-Ionized) water for 5 seconds

4. Blow dry with nitrogen gun
5. Place on 90°C hot plate for 60 seconds
6. Load samples into e-beam evaporator
7. Deposit 1000 angstroms of aluminum at a deposition rate of 1.0 angstrom per second

A.3 Aluminum Anodization

1. Perform standard clean
2. Place the copper tape over the edge of the aluminum on the slide
3. Cover the copper tape and surrounding Al with Kaptan tape
4. Anodize at 18 or 30V for 8 minutes in 30 wt.% ammonium pentaborate ($NH_4B_5O_8$) in 99.99% ethylene glycol at room temperature
5. Rinse with DI
6. Remove tapes
7. Perform standard clean

A.4 Hydrophobic layer

The 3 hydrophobic layer fabrications will be detailed, for each of the Hydrophobic layers used within this work. One spin coat of 1 wt.% CYTOP (section A.4.1), two spin coats of 2 wt.% CYTOP (section A.4.2), three spin coats of 0.5 wt.% CYTOP (section A.4.3).

A.4.1 Single spin coat application

1. Mix CYTOP from (Bellex International Corporation) and its solvent to 1 wt.%
2. Perform standard clean
3. Spin coat 1 wt.% CYTOP on the slide at 2000 RPM for 30 seconds
4. Bake at 160°C for 1 hour

A.4.2 Dual spin coat application

1. Mix CYTOP from (Bellex International Corporation) and its solvent to 2 wt.%
2. Perform standard clean
3. Spin coat 2 wt.% CYTOP on the slide at 2000 RPM for 30 seconds
4. Bake at 90°C for 15 minutes
5. Spin coat 2 wt.% CYTOP on the slide at 2000 RPM for 30 seconds
6. Bake at 160°C for 1 hour

A.4.3 Triple spin coat application

1. Mix CYTOP from (Bellex International Corporation) and its solvent to 0.5 wt.%
2. Perform standard clean
3. Spin coat 0.5 wt.% CYTOP on the slide at 2000 RPM for 30 seconds
4. Bake at 90°C for 15 minutes
5. Spin coat 0.5 wt.% CYTOP on the slide at 2000 RPM for 30 seconds
6. Bake at 90°C for 15 minutes

7. Spin coat 0.5 wt. % CYTOP on the slide at 2000 RPM for 30 seconds

8. Bake at 160°C for 1 hour

A.4.4 Silicon Oil Treatment

1. Mix silicon oil (Dow Corning OS-10, OS-20, and OS-30) to a 1:8:1 by weight ratio.

2. Perform standard clean

3. Apply oil mixture to surface

4. Allow oil to evaporate from surface for 15 minutes

A.5 Electrical Connection

1. Scratch CYTOP surface at the bare Al edge of slide

2. Place copper tape over scratches

3. Check resistance with multimeter

Appendix B

Fabrication of the Dual Active Surface CFAM Top Plate

The top plate of the CFAM-DAS was composed of 2 glass slides, each with an electrode – one electrode covered in a dielectric layer (the second active surface), the other uncovered. The slide with the uncovered electrode is referred to as Part A, while the slide with the active surface on the electrode is referred to as Part B. Part A and Part B of the top plate are fabricated with a borosilicate glass slide, 22mm x 22mm x 0.012mm (120µm).

B.1 Laser Cut Geometry

Both Parts A and B use this procedure

1. Place tape on both faces of the slide
2. Place slide in laser cutter and secure it – bottom side facing up
3. Align and focus laser head
4. Input design and laser power settings
5. Perform laser cut

6. Remove slide from cutter
7. Soak slide in D'limonene solvent for 5 minutes
8. Remove tape with tweezers
9. Rinse with DI
10. Swab slides with trichloroethylene (TCE) for 30 seconds on each side
11. Rinse with acetone, isopropyl alcohol, and DI for 5 seconds each
12. Blow dry with nitrogen gun
13. Blade backside of slide with razor blade

B.2 Part A Fabrication

1. Rinse with acetone, isopropyl alcohol, and DI (De-Ionized) water for 30 seconds each
2. Blow dry with nitrogen gun
3. Place on 90°C hot plate for 60 seconds
4. Load samples into e-beam evaporator
5. Deposit 25 angstroms of titanium (Ti) then 100 angstroms of gold (Au) at a deposition rate of 1.0 angstrom per second
6. Deposit black wax dissolved in TCE adjacent to the hole with a toothpick

B.3 Part B Fabrication

B.3.1 Aluminum Deposition

1. Rinse with acetone, isopropyl alcohol, and DI water for 30 seconds each

2. Blow dry with nitrogen gun
3. Place on 90°C hot plate for 60 seconds
4. Load samples into e-beam evaporator
5. Deposit 1000 angstroms of aluminum (Al) at a deposition rate of 1.0 angstrom per second

B.3.2 Aluminum Anodization

1. Perform standard clean, see Appendix A.1
2. Place the copper tape over the bottom edge of the Al on the slide
3. Cover the copper tape and adjacent Al with Kaptan tape
4. Anodize at 18V for 8 minutes in 30 wt. % ammonium pentaborate ($NH_4B_5O_8$) in 99.99 % ethylene glycol at room temperature
5. Rinse with DI
6. Remove tape
7. Perform standard clean

B.3.3 Titanium Deposition

1. Rinse with acetone, isopropyl alcohol, and DI water for 30 seconds each
2. Blow dry with nitrogen gun
3. Place on 90°C hot plate for 60 seconds
4. Load samples into e-beam evaporator with shadowmasks protecting the laser cut geometry

5. Deposit 1000 angstroms of Ti at a deposition rate of 1.0 angstrom per second

B.3.4 Hydrophobic layer

1. Mix CYTOP from (Bellex International Corporation) and its solvent to 1 wt.%
2. Perform standard clean
3. Spin coat 1 wt.% CYTOP on the Slide at 2000 RPM for 30 s
4. Remove CYTOP from Ti edge with a swab
5. Bake at 160°C for 1 hour

B.4 Assembly of Top Slides Part A and Part B

1. Perform standard clean
2. Mix CYTOP from (Bellex International Corporation) and its solvent to 8 wt.%
3. Spin coat 8 wt.% CYTOP on the Part A Slide at 2000 RPM for 30 s
4. Remove CYTOP from side edge with a swab
5. Align laser cut geometry on Part A and Part B
6. Press Part B onto Part A
7. Bake at 160°C for 1 hour
8. Remove black wax, with TCE Rinse for 30 seconds
9. Blade conductive silver epoxy on the top of the plate over the edge from Part A to Part B
10. Allow epoxy to fully cure

11. Perform silicon oil treatment on the CYTOP layer, see Appendix A.4.4
12. Cut and secure MetGlas to the top of the plate with tape
13. Paint gallium indium, GaI, from the epoxy on Part A around the edge of the Part A slide to the Au layer
14. Paint GaI, from the top of Part B around the edge of the Part B slide to the Ti layer
15. Tape 25 µm Dia. copper or Au wires over the two GaI spots on the top of the plate
16. Check resistance with multimeter – check for short between Part A and B
17. Place PDMS over hole geometry on top surface
18. Check PDMS flatness with DekTAK profilometer
19. Deposit microbead spacers – in solution – on the bottom of the plate
20. Inspect the microbeads with a microscope
21. Allow the micobead solution to evaporate for 30 minutes

Appendix C

Alternative CFAM-DAS Top Plate Hole Geometries

C.1 CFAM-DAS Top Plate Part A – Nominal Membrane Diameter 800 microns

This was laser cut design used to implement a membrane radius of approximately 400 microns for the top plate Part A of CFAM-DAS prototypes. It was the laser cut used on device G-DAS. Figure C.1 shows the laser cutter input with added dimensions for this design. The design differs from the laser cut presented in section 3.2.1 by the removal of the outer two concentric circle, to reduce the size of the throughcut hole. Table C.1 gives a summary of the cutting parameters.

C.2 CFAM-DAS Top Plate Part A – Nominal Membrane Diameter 600 microns

This was laser cut design used to implement a membrane radius of approximately 300 microns for the top plate Part A of CFAM-DAS prototypes. It was the laser cut used on device F-

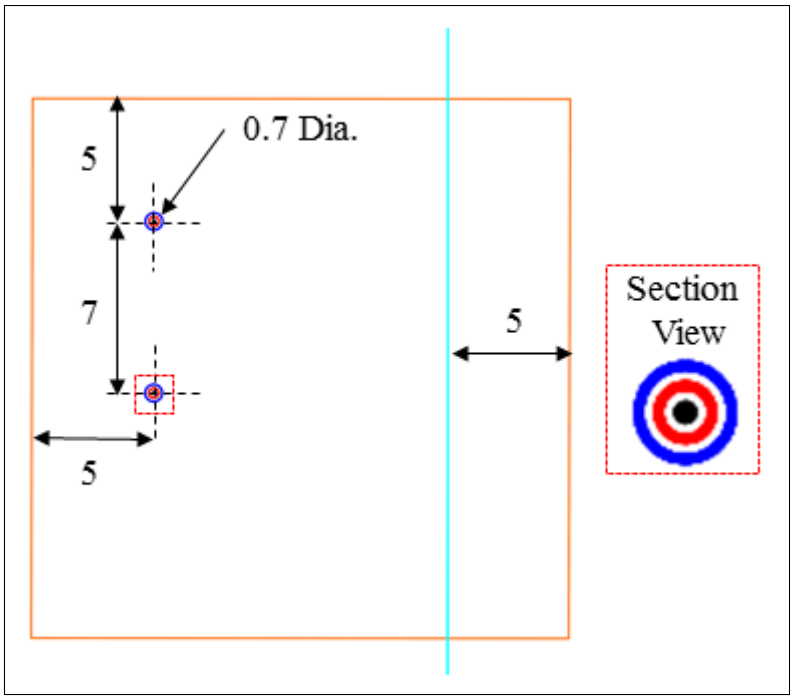

Figure C.1: Laser cutter input for CFAM-DAS top plate part A with a nominal diameter of 800 µm. Note: Dimensions are in mm, and the orange square is for laser alignment.

Table C.1: Laser cutter inputs for CFAM-DAS top plate Part A with a nominal dia. of 800 µm.

Feature	Color	Dimension. (mm)	Laser Power (%)	Laser Speed (%)	# of Passes
Circle	Black	0.1 Dia.	24	31	5
Circle	Red	0.4 Dia.	24	31	7
Circle	Blue	0.7 Dia.	24	31	8
Line	Cyan	25 x 0	24	31	5
Square	Orange	22 x 22	0	N/A	0

Note, the orange square is an alignment feature. The cyan line is over sized to ensure a through cut.

DAS and I-DAS. Figure C.2 shows the laser cutter input with added dimensions for this design.The design differs from the laser cut presented in section 3.2.1 by the removal of the outer three concentric circle, to reduce the size of the throughcut hole. Table C.2 gives a summary of the cutting parameters.

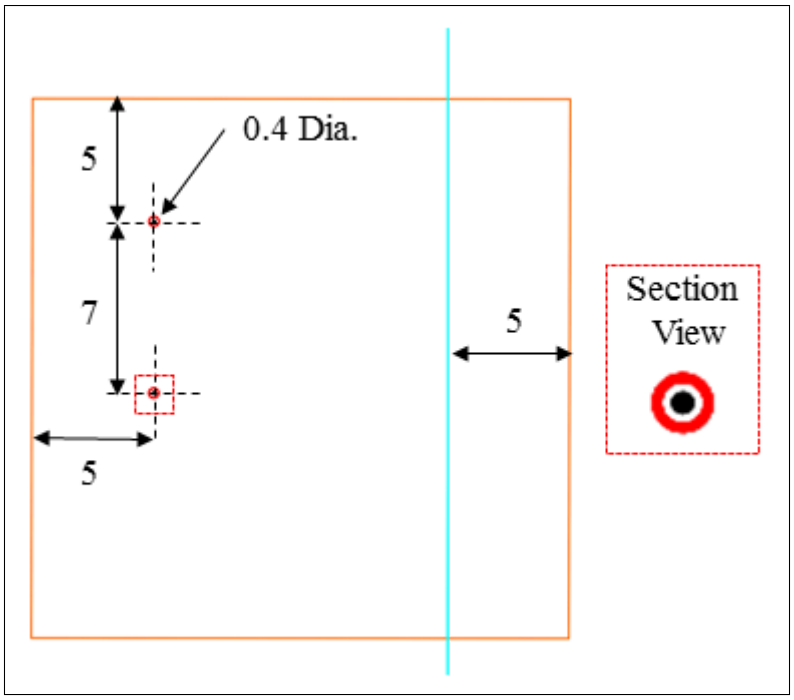

Figure C.2: Laser cutter input for CFAM-DAS top plate part A with a nominal diameter of 600 µm. Note: Dimensions are in mm, and the orange square is for laser alignment.

Table C.2: Laser cutter inputs for CFAM-DAS top plate Part A with a nominal dia. of 600 µm.

Feature	Color	Dimension. (mm)	Laser Power (%)	Laser Speed (%)	# of Passes
Circle	Black	0.1 Dia.	24	31	5
Circle	Red	0.4 Dia.	24	31	7
Square	Orange	22 x 22	0	N/A	0

Note, the orange square is an alignment feature. The cyan line is over sized to ensure a through cut.

C.3 CFAM-DAS Top – Alternative Design 1 – Nominal Membrane Diameter 1000 microns

These laser cut designs differs from the final design by lacking a throughcut line on the Part B design. The throughcuts were made with a glass cutter after discovering a narrowed Part B aided in the electrical connection to Part A, later prototypes use the laser cut design in section 3.2.2. The throughcut holes were also centered in this design, they are offset in

the future design to accommodate the throughcut lines. This design was used with devices B-DAS and M-DAS

C.3.1 Top Plate Part A

This design was used to implement a membrane radius of approximately 1000 microns in the alternative design. Figure C.3 shows the laser cutter input with added dimensions for this design. The only difference from the final design was the hole location. Table C.3 gives a summary of the cutting parameters.

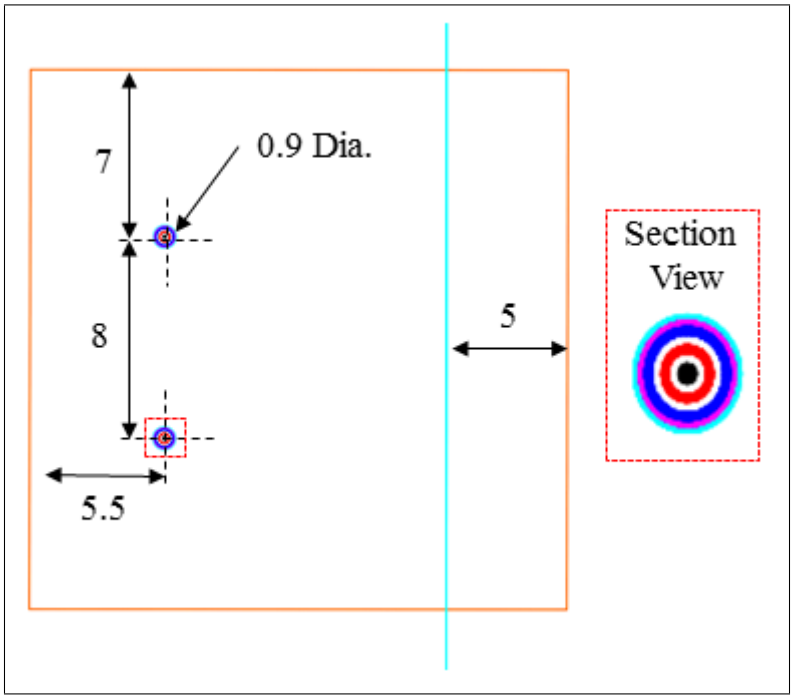

Figure C.3: Laser cutter input for CFAM-DAS top plate part A with a nominal diameter of 1000 µm. Note: Dimensions are in mm, and the orange square is for laser alignment.

C.3.2 Top Plate Part B

This design was used to define the concentric hole to allow the conducting drop to contact the ground electrode in the alternative design. Figure C.4 shows the laser cutter input

Table C.3: Laser cutter inputs for Alternative Design 1 for CFAM-DAS top plate Part A.

Feature	Color	Dimension. (mm)	Laser Power (%)	Laser Speed (%)	# of Passes
Circle	Black	0.1 Dia.	24	31	5
Circle	Red	0.4 Dia.	24	31	7
Circle	Blue	0.7 Dia.	24	31	8
Circle	Magenta	0.8 Dia.	24	31	7
Circle	Cyan	0.9 Dia.	24	31	7
Line	Cyan	25 x 0	24	31	5
Square	Orange	22 x 22	0	N/A	0

Note, the orange square is an alignment feature. The cyan line is over sized to ensure a through cut.

with added dimensions for this design. The ony difference from the final design was the hole location and lack of a throughcut line. Table C.4 gives a summary of the cutting parameters.

Table C.4: Laser cut inputs for Alternative Design 1 for CFAM-DAS top plate Part B.

Feature	Color	Dimension. (mm)	Laser Power (%)	Laser Speed (%)	# of Passes
Circle	Black	0.6 Dia.	24	31	5
Circle	Red	0.9 Dia.	24	31	7
Circle	Blue	1.2 Dia.	24	31	8
Circle	Magenta	1.3 Dia.	24	31	7
Circle	Cyan	1.4 Dia.	24	31	7
Square	Orange	22 x 22	0	N/A	0

Note, the orange square is an alignment feature. The cyan line is over sized to ensure a through cut.

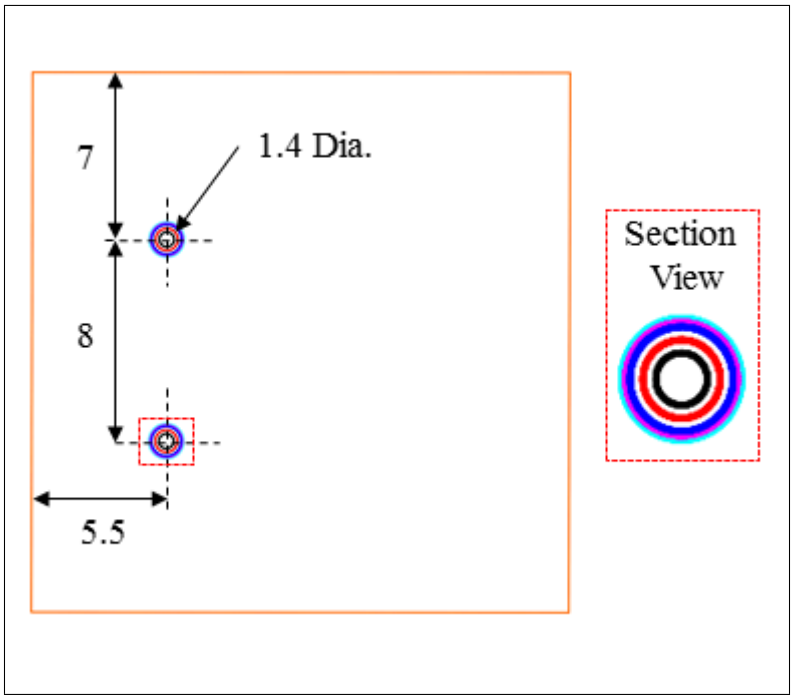

Figure C.4: Laser cutter input for CFAM-DAS top plate part B with a nominal diameter of 1500 µm. Note: Dimensions are in mm, and the orange square is for laser alignment.

Appendix D

Fabrication of the Single Active Surface CFAM Top Plate

The top plate of the CFAM-SAS was composed of 1 glass slide, with one uncovered electrode (the passive surface). The top plate was fabricated with a borosilicate glass slide, 22mm x 22mm x 0.012mm (120µm).

D.1 Laser Cut Geometry

1. Place $\sim$ 50 µm PDMS on both faces of the slide
2. Place slide in laser cutter and secure it – bottom side facing up
3. Align and focus laser head
4. Input design and laser power settings
5. Perform laser cut
6. Remove slide from cutter
7. Remove PDMS with tweezers

8. Blade backside of slide with razor blade

D.2 Gold Deposition

1. Rinse with acetone, isopropyl alcohol, and DI (De-Ionized) water for 30 seconds each
2. Blow dry with nitrogen gun
3. Place on 90°C hot plate for 60 seconds
4. Load samples into e-beam evaporator
5. Deposit 25 angstroms of titanium (Ti) then 100 angstroms of gold (Au) at deposition rate of 1.0 angstrom per second

D.3 Hydrophobic layer

1. Mix CYTOP from (Bellex International Corporation) and its solvent to 1 wt.%
2. Perform standard clean
3. Spin coat 1 wt.% CYTOP on the slide at 2000 RPM for 30 s
4. Remove CYTOP from edge with a swab
5. Bake at 160°C for 1 hour

D.4 Assembly of Top Plate

D.4.1 Version I

1. Perform standard clean
2. Perform silicon oil treatment on the CYTOP layer, see Appendix A.4.4

3. Secure top of top plate to plexiglas holder with superglue
4. Paint GaI, from the top of plate around the edge of the to the Au layer
5. Tape copper tape onto the plexiglas holder and over the GaI spot on the top of the plate
6. Check resistance with multimeter
7. Place PDMS over hole geometry on top surface
8. Check PDMS flatness with DekTAK profilometer
9. Deposit microbead spacers – in solution – on the bottom of the plate
10. Inspect the microbeads with a microscope
11. Allow the micobead solution to evaporate for 30 minutes

D.4.2 Verison II

1. Perform standard clean
2. Perform silicon oil treatment on the CYTOP layer, see Appendix A.4.4
3. Cut and secure MetGlas to the top of the plate with tape
4. Paint GaI, from the top of plate around the edge of the to the Au layer
5. Tape 25 µm Dia. copper or Au wires over the GaI spot on the top of the plate
6. Check resistance with multimeter
7. Place PDMS over hole geometry on top surface
8. Check PDMS flatness with DekTAK profilometer
9. Deposit microbead spacers – in solution – on the bottom of the plate

10. Inspect the microbeads with a microscope

11. Allow the micobead solution to evaporate for 30 minutes

Appendix E

Alternative CFAM-DAS Top Plate Hole Geometries

E.1 CFAM-SAS Top Plate – Nominal Diameter 1000 micron – Alternative Laser Cut Design 1

This design was the original Top Plate design, for CFAM-SAS, it implemented a smaller pinning ring, and a slightly altered concentric circle design. Also, there was only 1 hole in this design. To cut a second hole in the top plate a second cut was performed in a new location on the glass slide. Hole location is unimportant for CFAM-SAS devices. The laser settings were lower because the laser was performing at a overall higher power ($\sim$ 50Watt verses the final $\sim$ 30Watt). This cut was used on the majority of CFAM-SAS devices: B, C, E, F, G, H, K, N , O, and P. Figure E.1 shows the laser cutter input with added dimensions for this design, and Table E.1 gives a summary of the cutting parameters.

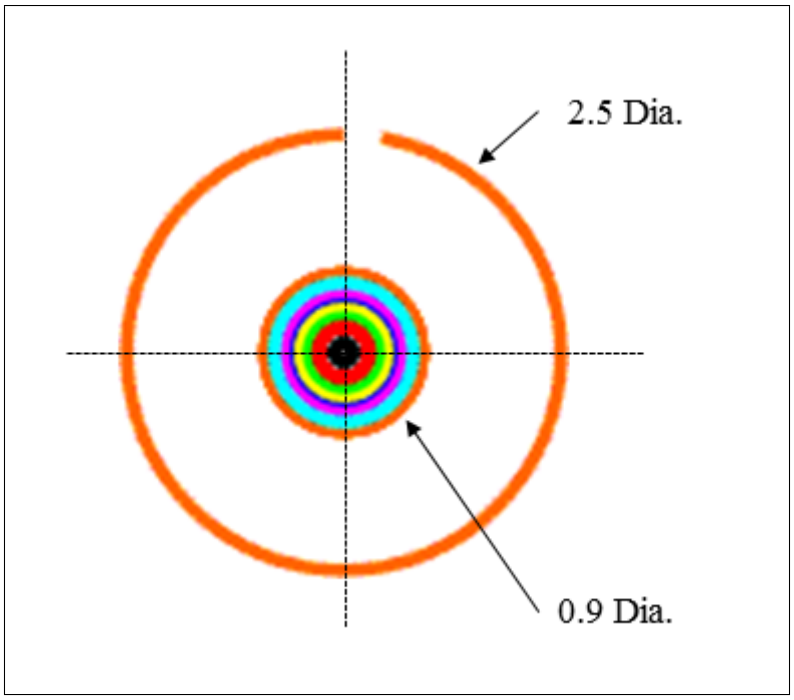

Figure E.1: Laser cutter input for CFAM-SAS Alternative Laser Cut Design 1. Note: Dimensions are in mm, and the orange square is for laser alignment.

Table E.1: Laser cutter inputs for CFAM-SAS Alternative Laser Cut Design 1.

Feature	Color	Dimension. (mm)	Laser Power (%)	Laser Speed (%)	# of Passes
Circle	Black	0.1 Dia.	13	35	5
Circle	Red	0.3 Dia.	13	35	7
Circle	Green	0.4 Dia.	13	35	7
Circle	Yellow	0.5 Dia.	13	35	7
Circle	Blue	0.6 Dia.	13	35	7
Circle	Magenta	0.7 Dia.	13	35	7
Circle	Cyan	0.8 Dia.	13	35	7
Circle	Orange	0.9 Dia.	13	35	7
350° Arc	Orange	2.5 Dia.	13	35	1

E.2 CFAM-SAS Top Plate – Nominal Diameter 1000 micron – Alternative Laser Cut Design 2

This design was a modification of the alternative design presented in section E.2, only the diameter of the pinning ring differs. This design was used for CFAM-SAS devices: D, I, and

J. Figure E.2 shows the laser cutter input with added dimensions for this design, and Table E.2 gives a summary of the cutting parameters.

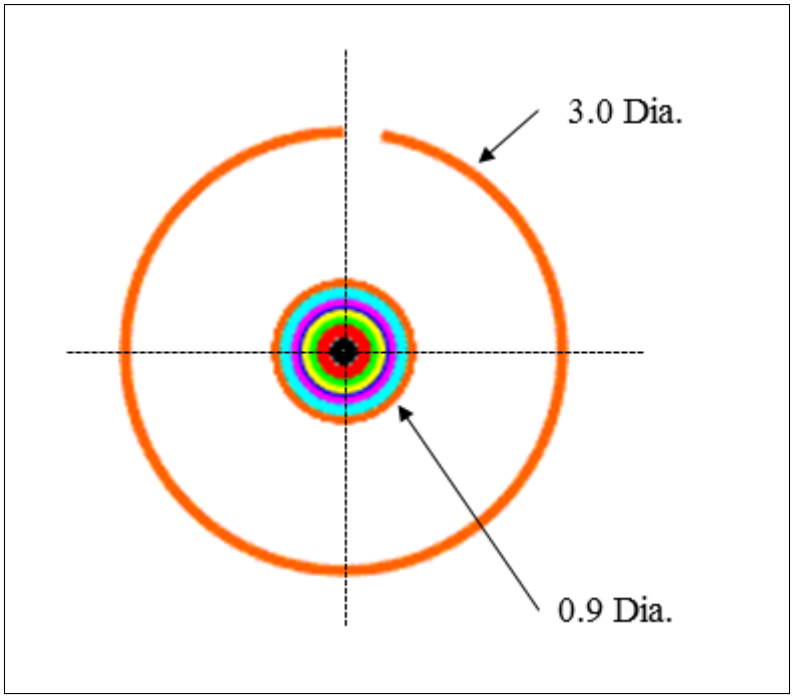

Figure E.2: Laser cutter input for CFAM-SAS Alternative Laser Cut Design 2. Note: Dimensions are in mm.

Table E.2: Laser cutter inputs for CFAM-SAS Alternative Laser Cut Design 1.

Feature	Color	Dimension. (mm)	Laser Power (%)	Laser Speed (%)	# of Passes
Circle	Black	0.1 Dia.	13	35	5
Circle	Red	0.3 Dia.	13	35	7
Circle	Green	0.4 Dia.	13	35	7
Circle	Yellow	0.5 Dia.	13	35	7
Circle	Blue	0.6 Dia.	13	35	7
Circle	Magenta	0.7 Dia.	13	35	7
Circle	Cyan	0.8 Dia.	13	35	7
Circle	Orange	0.9 Dia.	13	35	7
350° Arc	Orange	3.0 Dia.	13	35	1

Appendix F

Fabrication of the PDMS Membranes

Dow Corning (USA) Polydimethysiloxane (PDMS) was used to manufacture the elastomeric membranes. The PDMS kit contains a base polymer (part A) and a curing agent (part B).

F.1 PDMS Fabrication

1. Mix base polymer (part A) and a curing agent (part B) 10 to 1 by wt.
2. Degas in ambient air for 90 minutes
3. Spin coat $\sim$ 1.5g of PDMS onto a PMMA wafer the slide at 1100 – 2200 RPM for 60 seconds
4. Bake in oven at $\sim$ 70 °C for 1 hour
5. Cut PDMS film into $\sim$ 5 mm squares
6. Transfer PDMS square samples to a glass slide
7. Check the thickness of the samples with the DekTAK profilometer
8. Place Ti foil on top of PDMS

Appendix G

CFAM-DAS Membrane Displacement Curves

Presented in this appendix are the individual membrane displacement curves for the CFAM-DAS tests presented in Chapter 4.

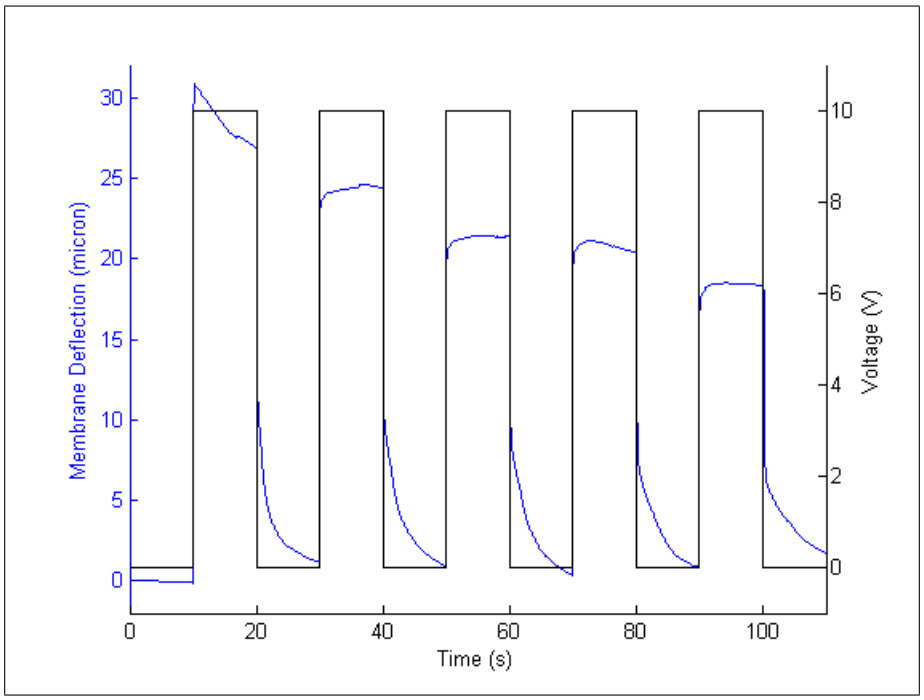

Figure G.1: Test A-DAS with $h = 116$ µm – $t_m = 37$ µm – $r_m = 475$ µm.

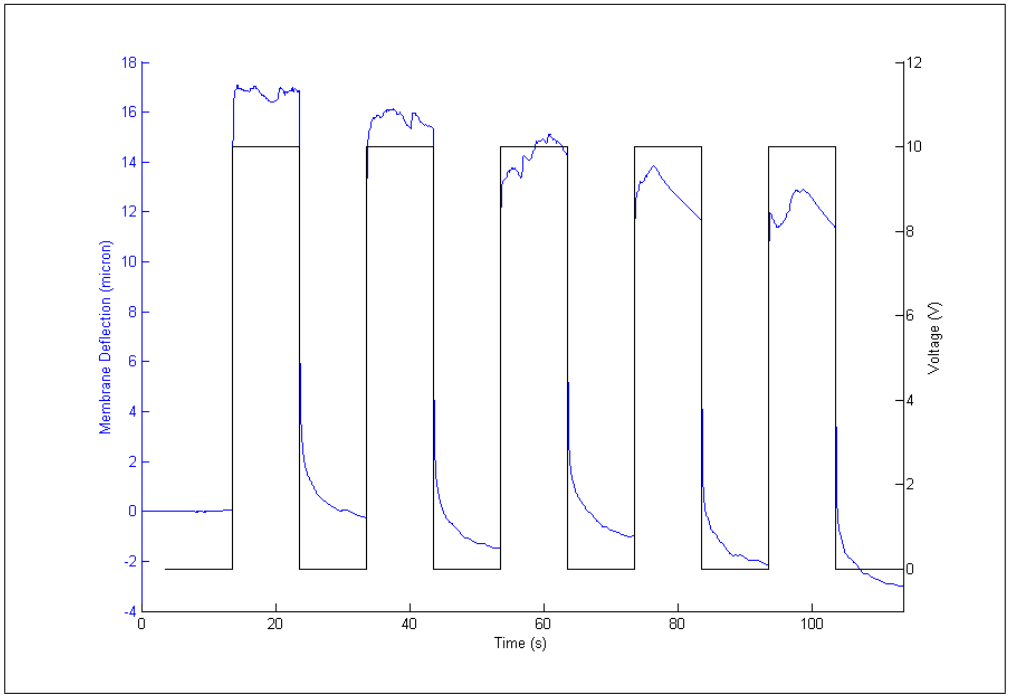

Figure G.2: Test B-DAS with $h = 83$ µm – $t_m = 46$ µm – $r_m = 480$ µm.

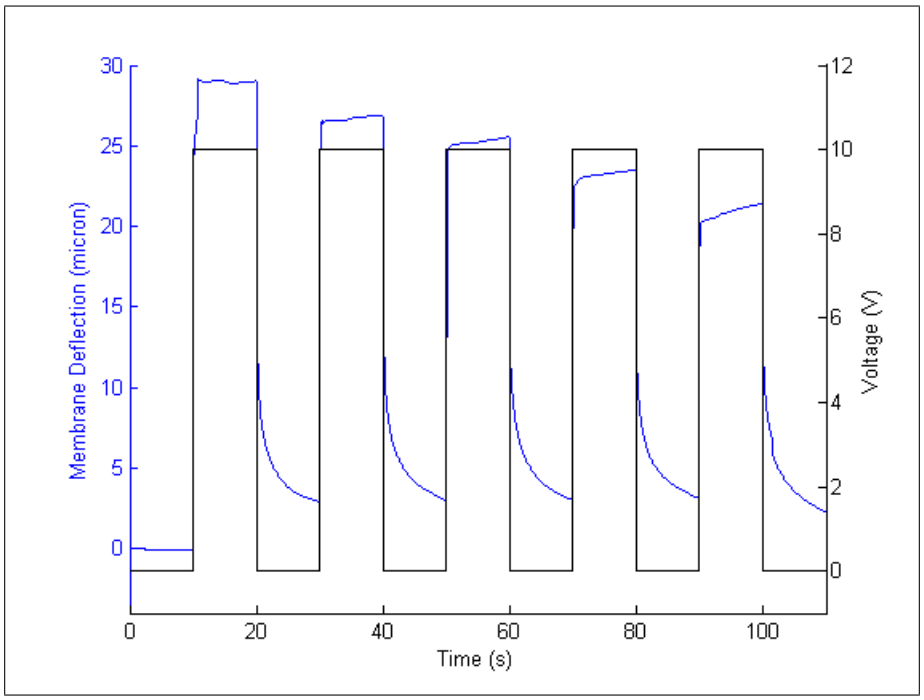

Figure G.3: Test C-DAS with $h = 67$ µm – $t_m = 47$ µm – $r_m = 474$ µm.

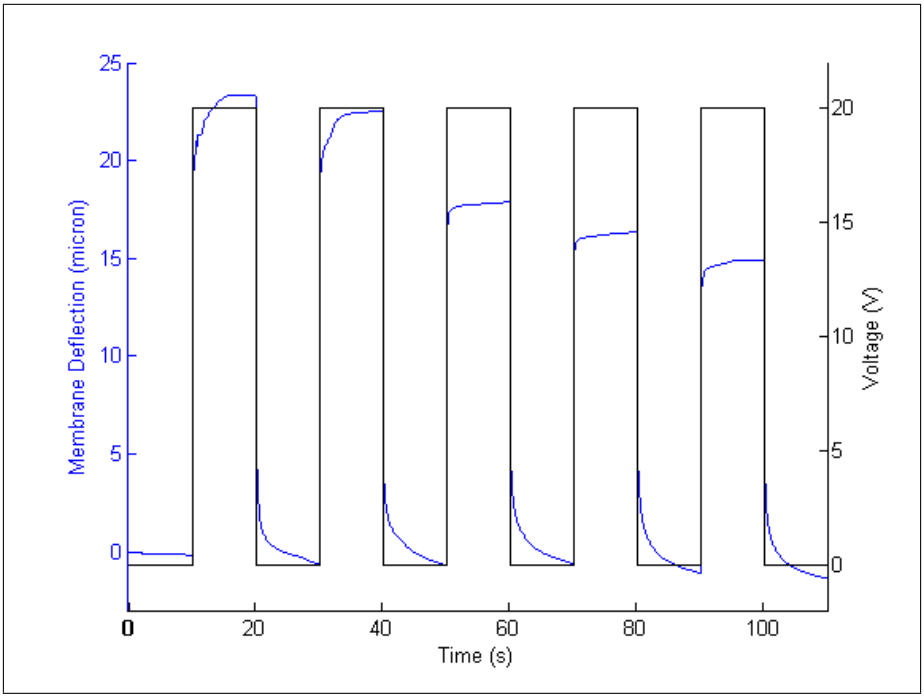

Figure G.4: Test D-DAS with $h = 68$ µm – $t_m = 47$ µm – $r_m = 474$ µm.

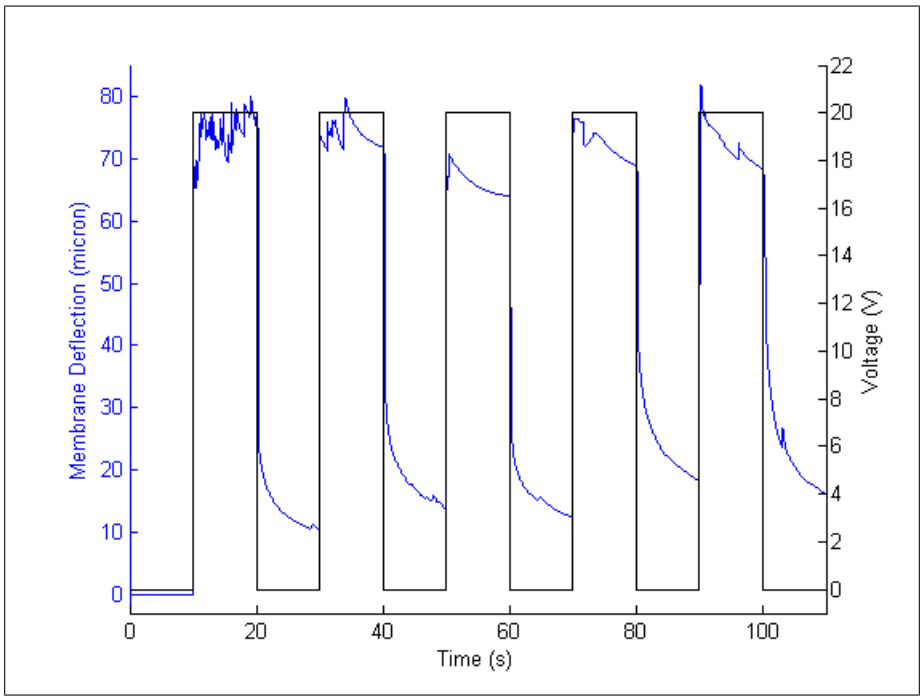

Figure G.5: Test E-DAS with $h = 45$ µm – $t_m = 36$ µm – $r_m = 476$ µm.

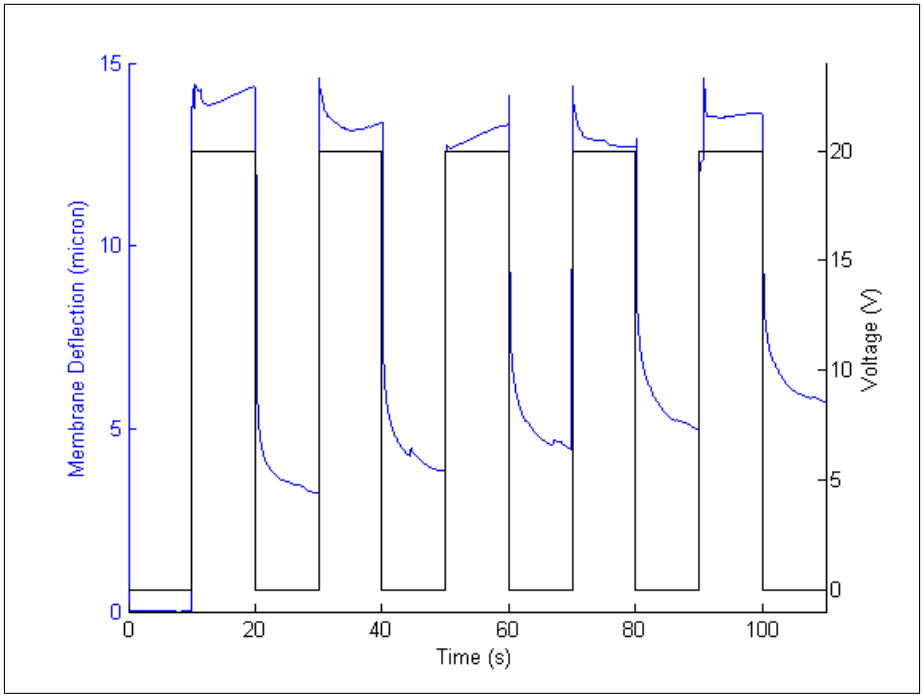

Figure G.6: Test F-DAS with $h = 65$ µm – $t_m = 35$ µm – $r_m = 326$ µm.

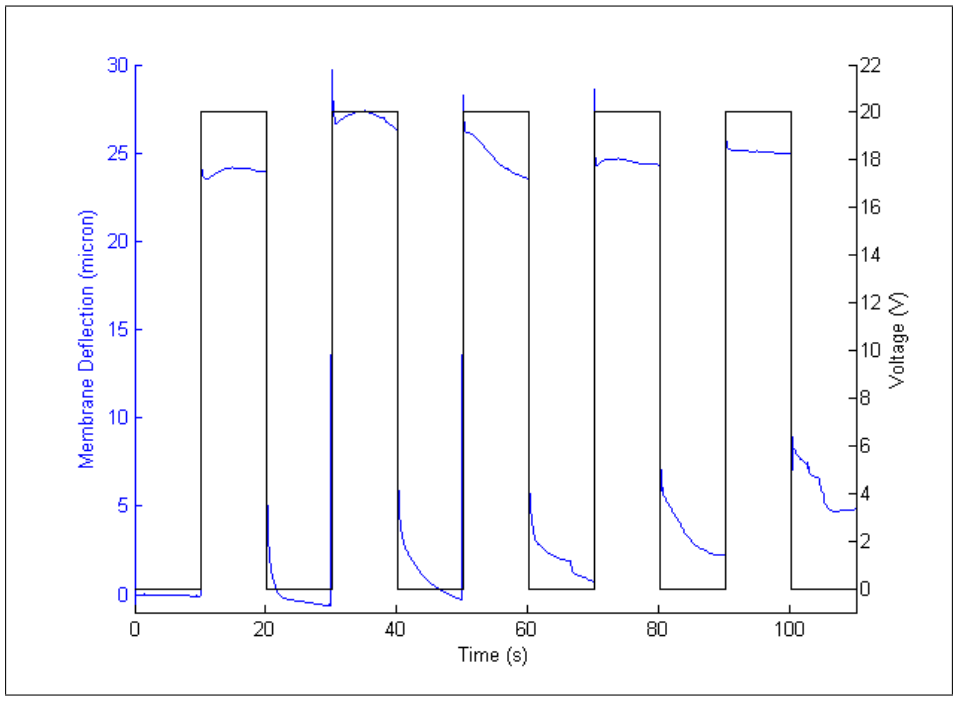

Figure G.7: Test G-DAS with $h = 56$ µm – $t_m = 39$ µm – $r_m = 434$ µm.

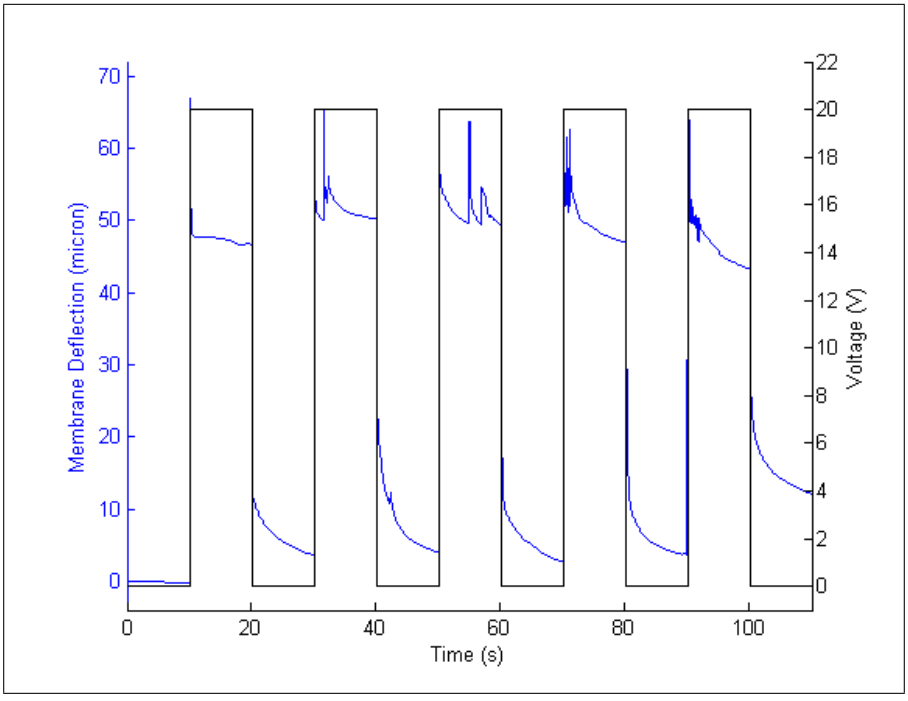

Figure G.8: Test H-DAS with $h = 67$ µm – $t_m = 47$ µm – $r_m = 474$ µm.

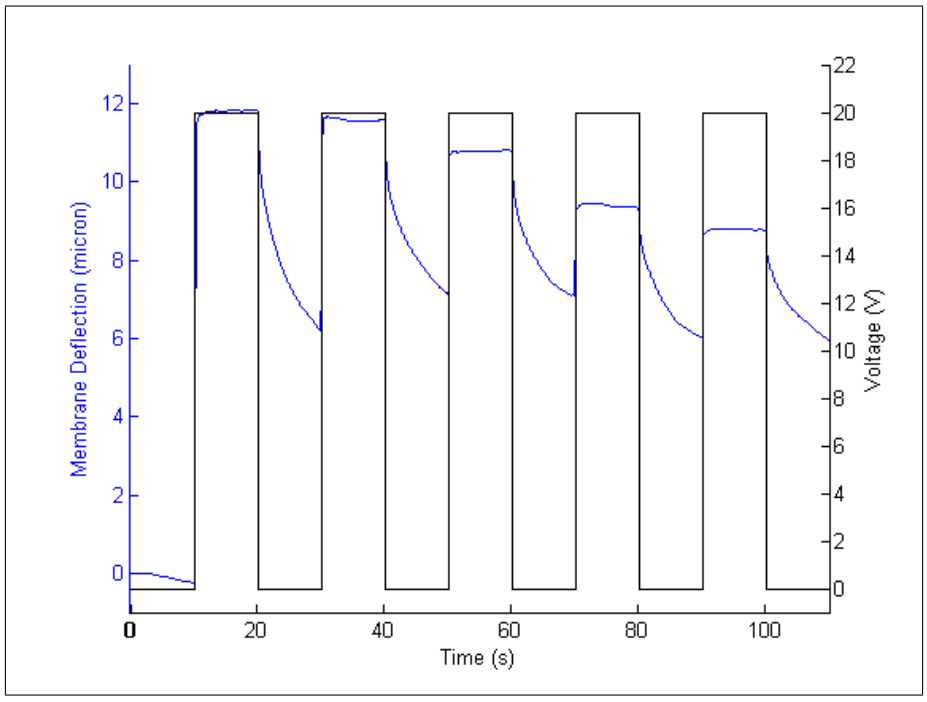

Figure G.9: Test I-DAS with $h = 76$ µm – $t_m = 46$ µm – $r_m = 338$ µm.

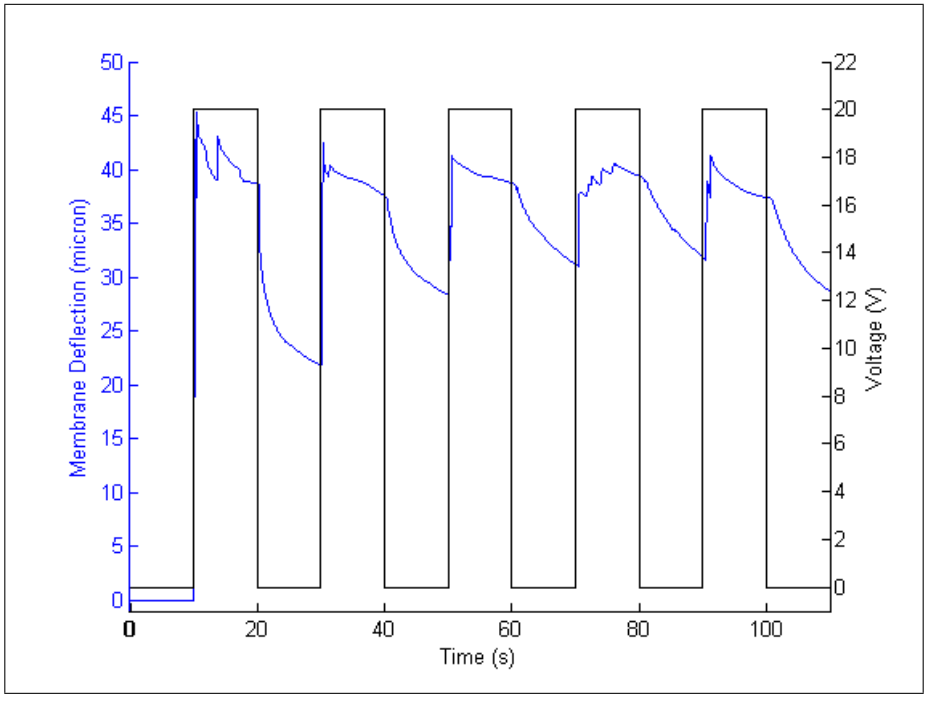

Figure G.10: Test J-DAS with $h = 69$ µm – $t_m = 47$ µm – $r_m = 474$ µm.

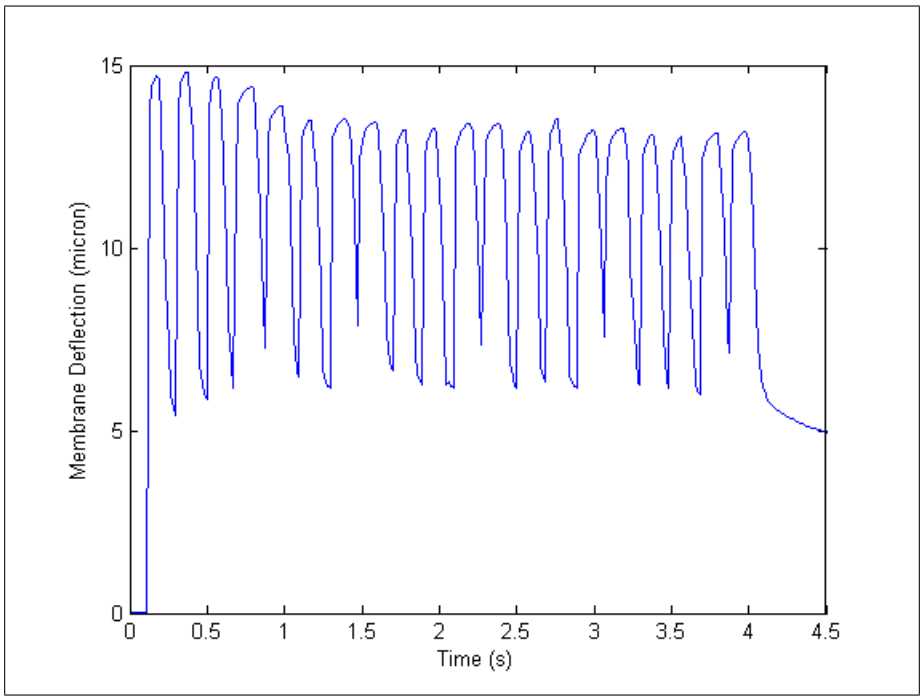

Figure G.11: Test K-DAS with $h = 66$ µm – $t_m = 47$ µm – $r_m = 474$ µm – 10V – 5 Hz.

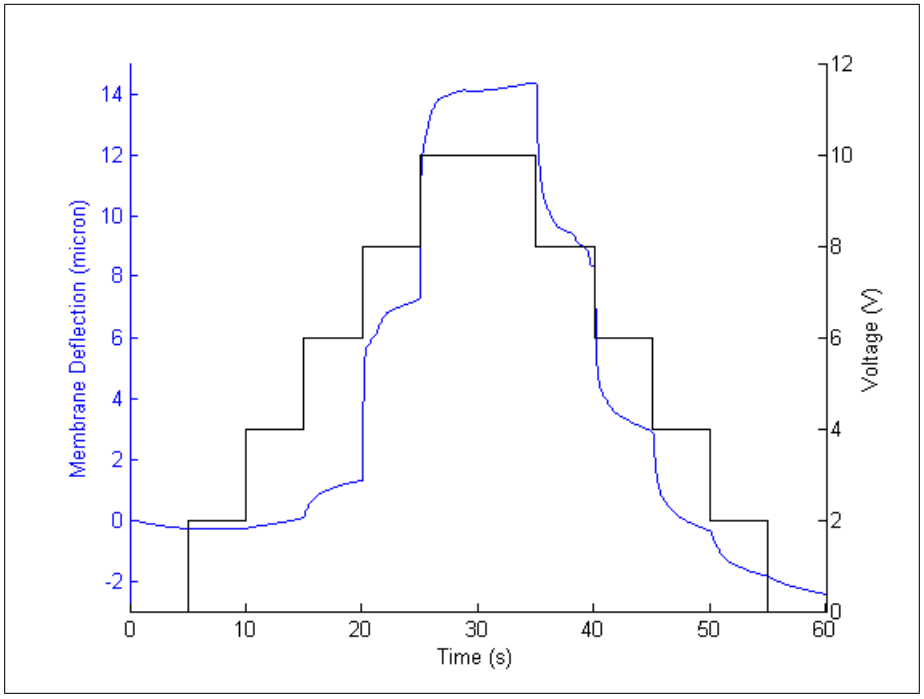

Figure G.12: Test L-DAS with $h = 110$ µm – $t_m = 47$ µm – $r_m = 471$ µm.

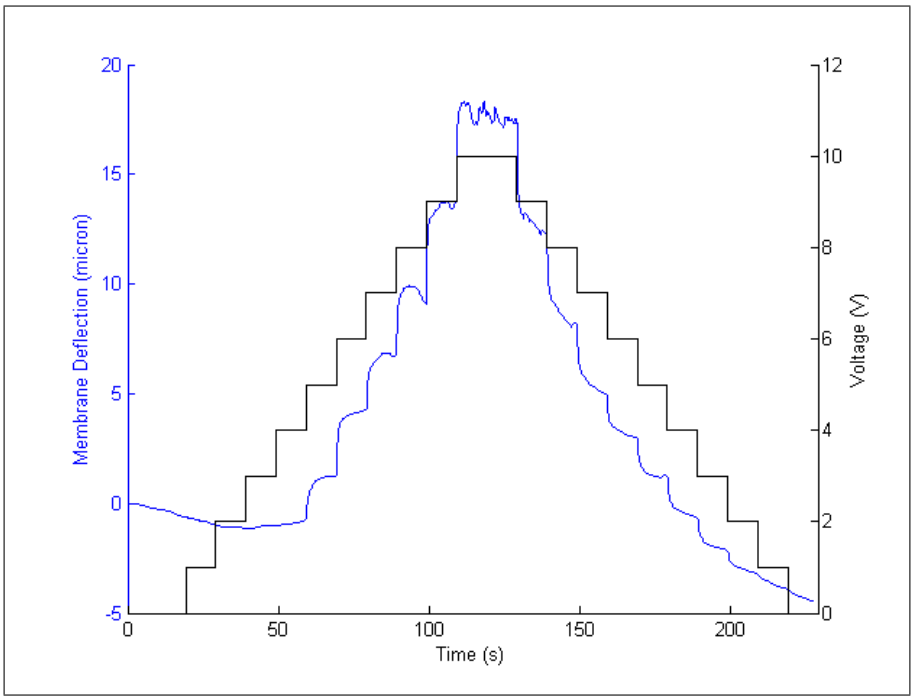

Figure G.13: Test M-DAS with $h = 88$ µm – $t_m = 46$ µm – $r_m = 480$ µm.

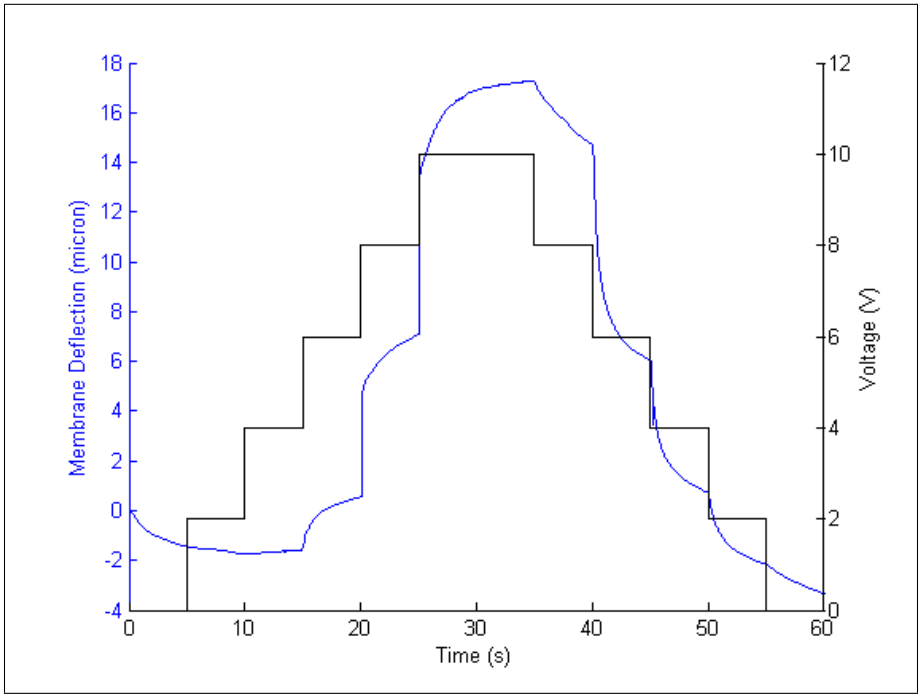

Figure G.14: Test N-DAS with $h = 122$ µm – $t_m = 37$ µm – $r_m = 475$ µm.

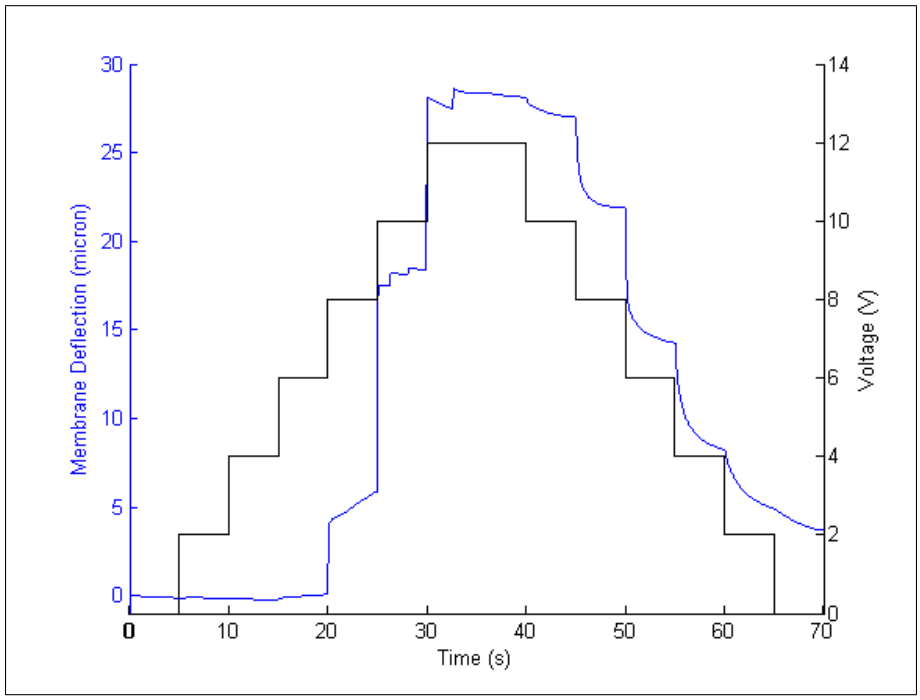

Figure G.15: Test O-DAS with $h = 74$ µm – $t_m = 44$ µm – $r_m = 467$ µm.

Appendix H

CFAM-SAS Membrane Displacement Curves

Presented in this appendix are the individual membrane displacement curves for the single active surface CFAM tests presented in Chapter 5.

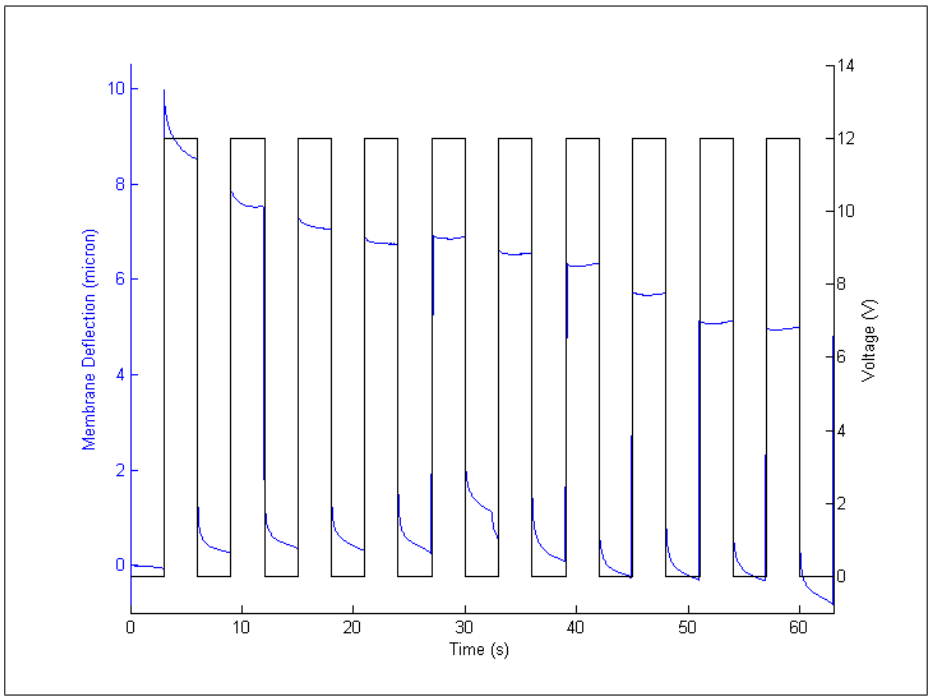

Figure H.1: Test A-SAS with h = 98 µm – t_m = 33 µm – r_m = 515 µm.

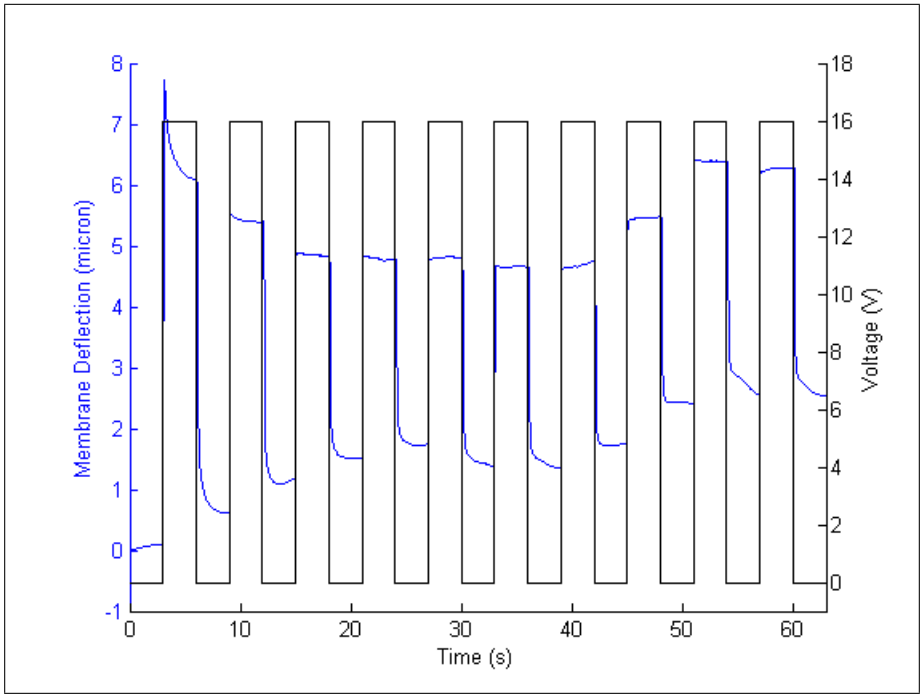

Figure H.2: Test B-SAS with h = 125 µm – t_m = 39 µm – r_m = 439 µm.

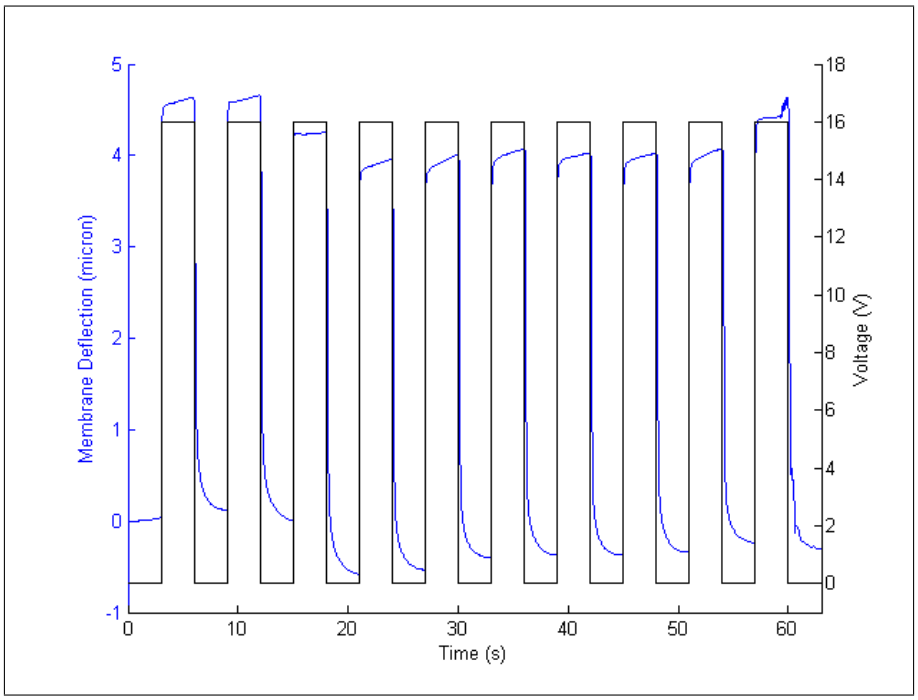

Figure H.3: Test C-SAS with $h = 102$ µm – $t_m = 33$ µm – $r_m = 439$ µm.

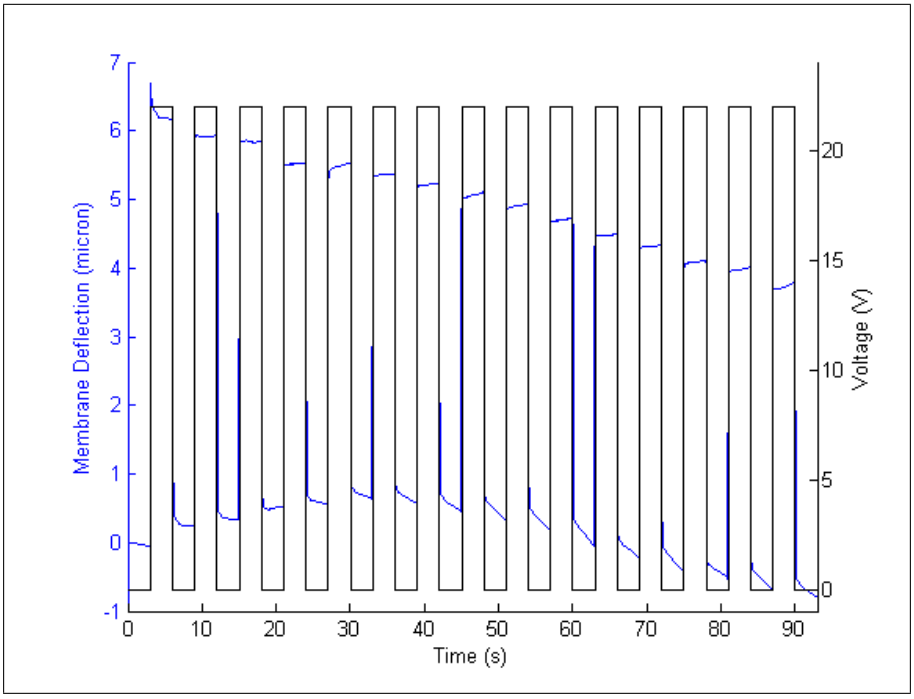

Figure H.4: Test D-SAS with $h = 108$ µm – $t_m = 39$ µm – $r_m = 438$ µm.

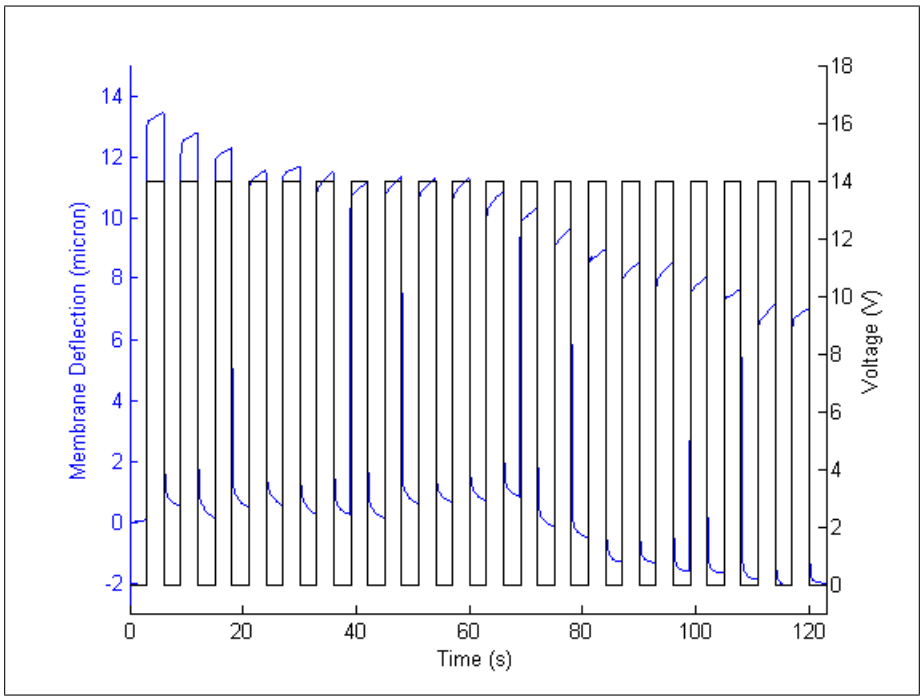

Figure H.5: Test E-SAS with $h = 111$ µm – $t_m = 40$ µm – $r_m = 441$ µm.

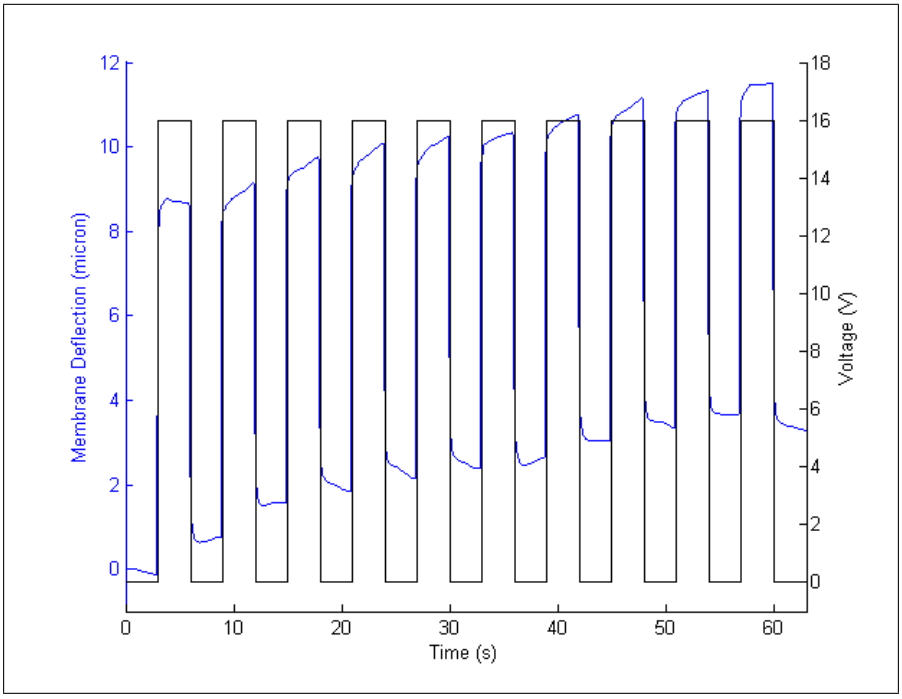

Figure H.6: Test F-SAS with $h = 106$ µm – $t_m = 40$ µm – $r_m = 442$ µm.

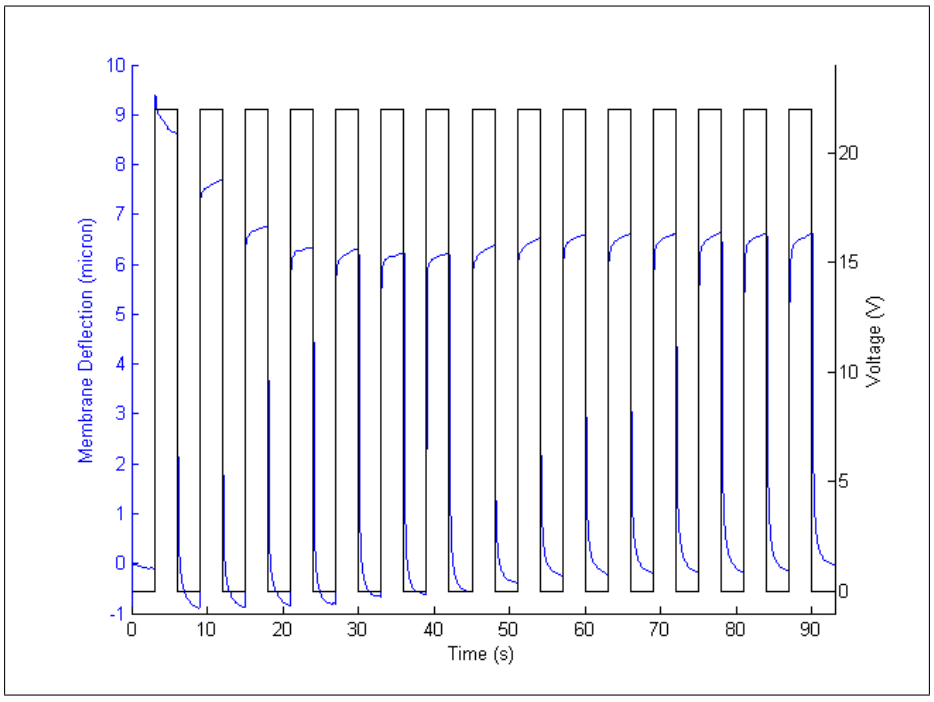

Figure H.7: Test G-SAS with $h = 95$ µm – $t_m = 41$ µm – $r_m = 438$ µm.

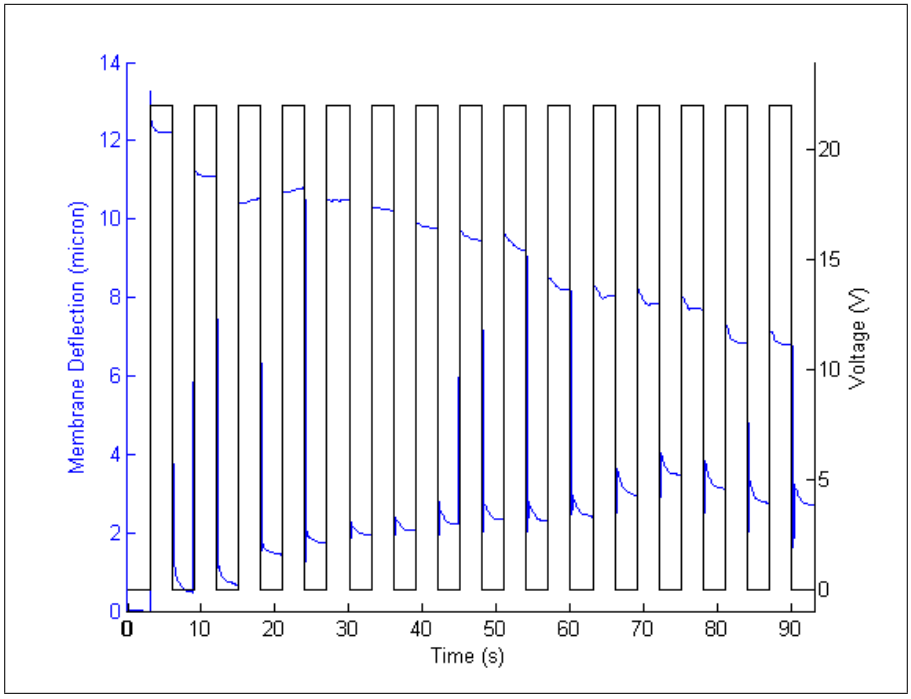

Figure H.8: Test H-SAS with $h = 95$ µm – $t_m = 24$ µm – $r_m = 442$ µm.

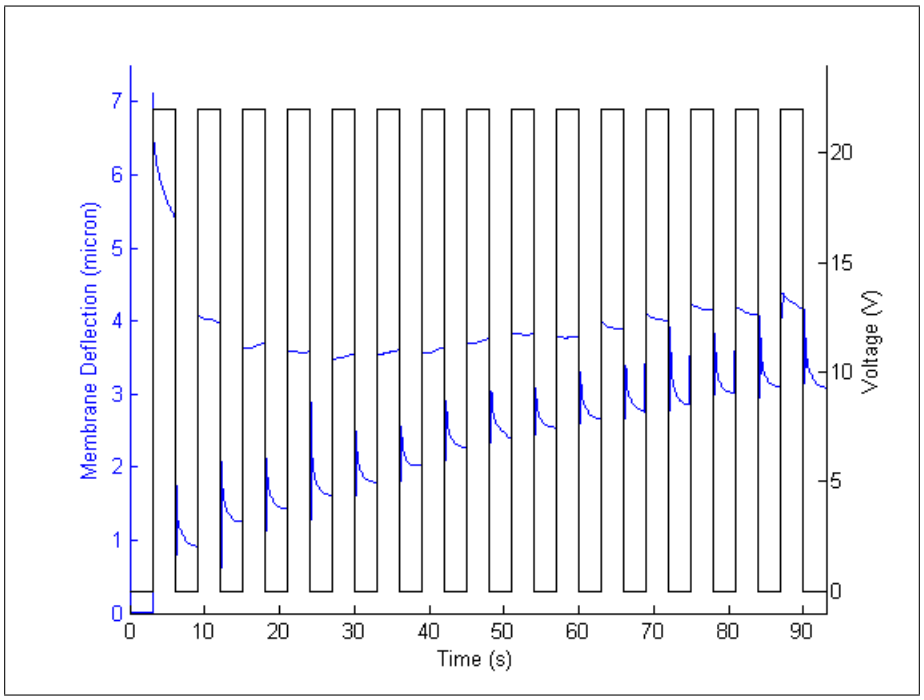

Figure H.9: Test I-SAS with $h = 117$ µm – $t_m = 39$ µm – $r_m = 438$ µm.

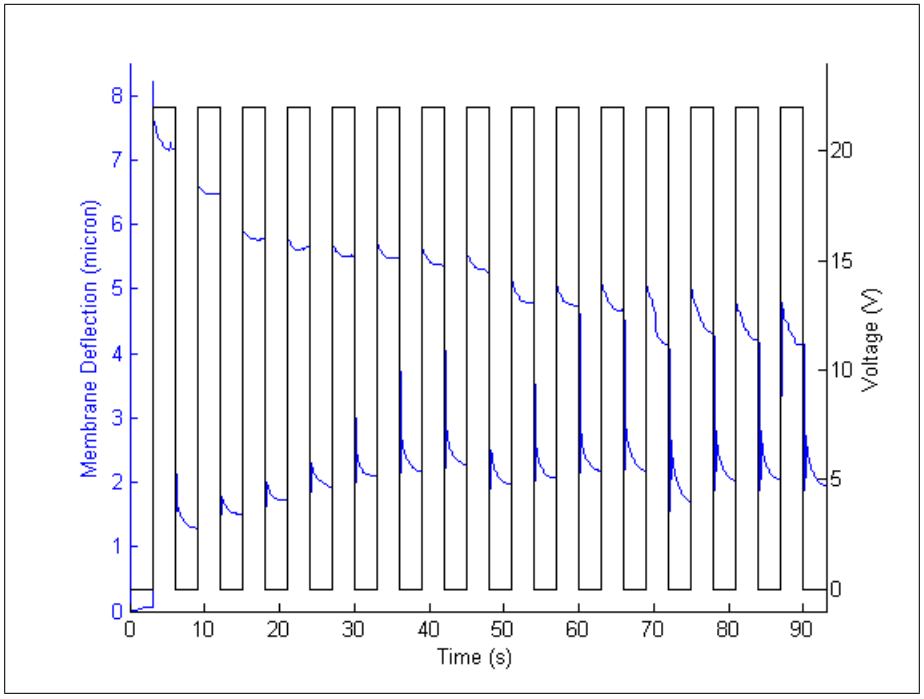

Figure H.10: Test J-SAS with $h = 93$ µm – $t_m = 39$ µm – $r_m = 438$ µm.

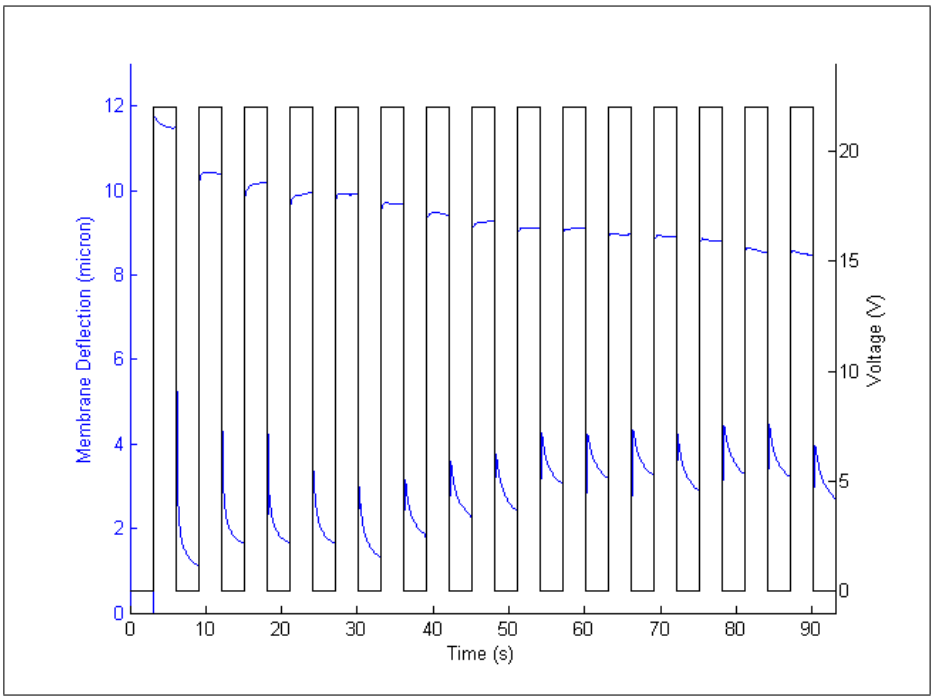

Figure H.11: Test K-SAS with $h = 93$ µm – $t_m = 41$ µm – $r_m = 438$ µm.

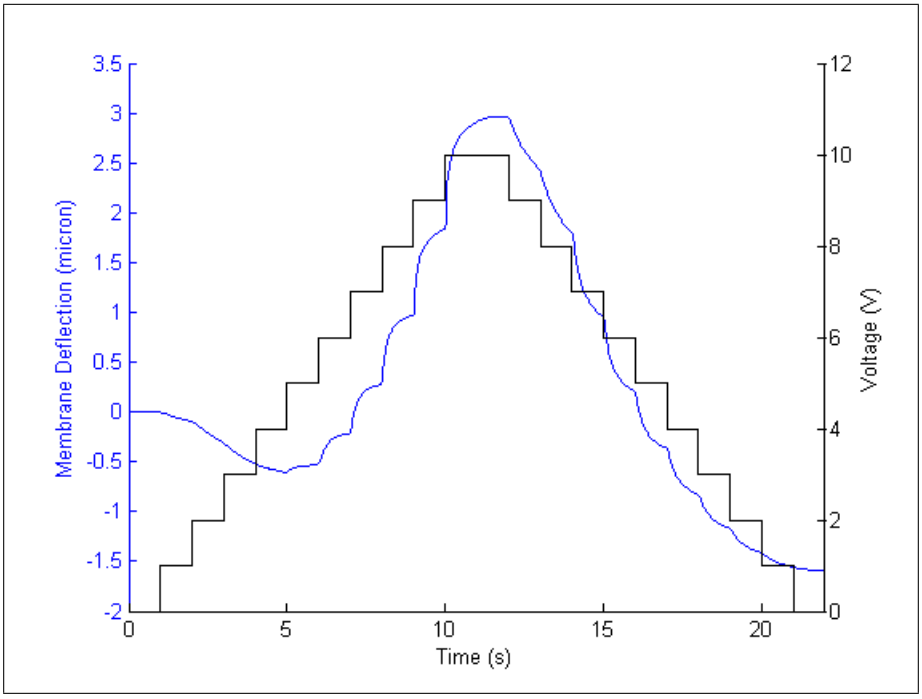

Figure H.12: Test L-SAS with $h = 91$ µm – $t_m = 39$ µm – $r_m = 510$ µm.

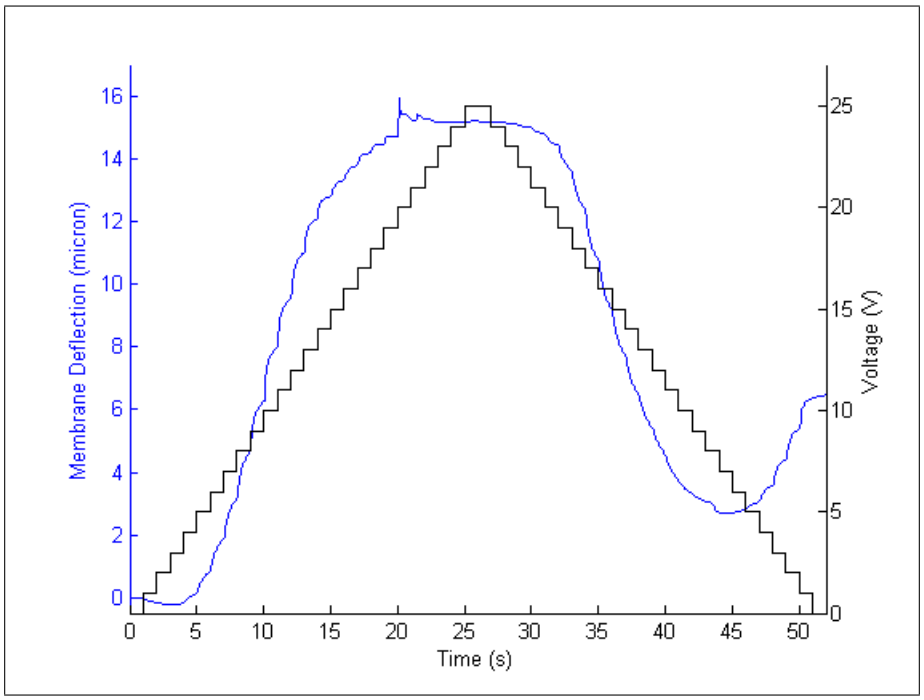

Figure H.13: Test M-SAS with $h = 93$ µm – $t_m = 39$ µm – $r_m = 510$ µm.

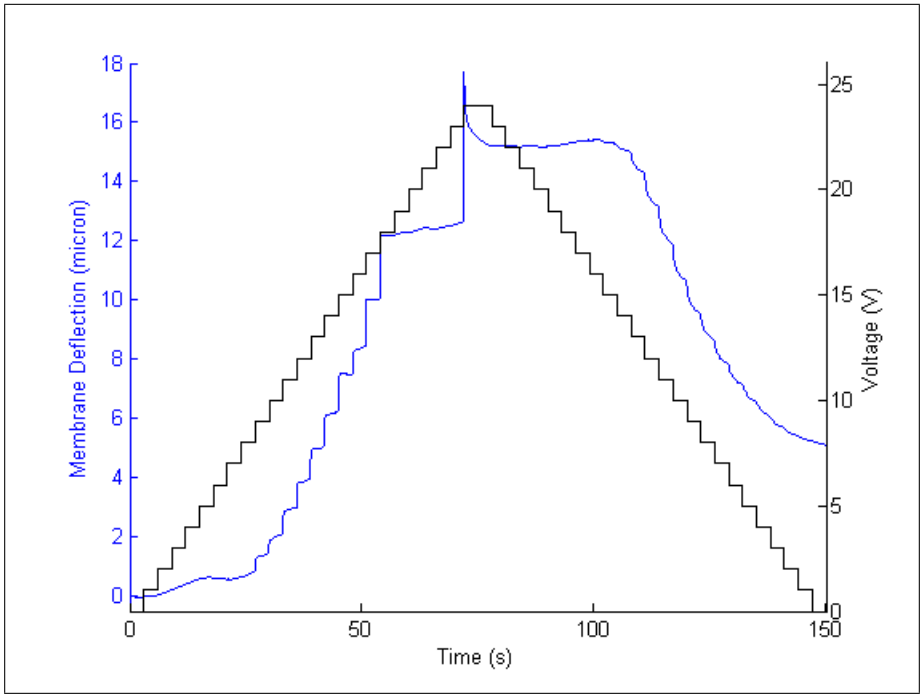

Figure H.14: Test N-SAS with $h = 123$ µm – $t_m = 39$ µm – $r_m = 439$ µm.

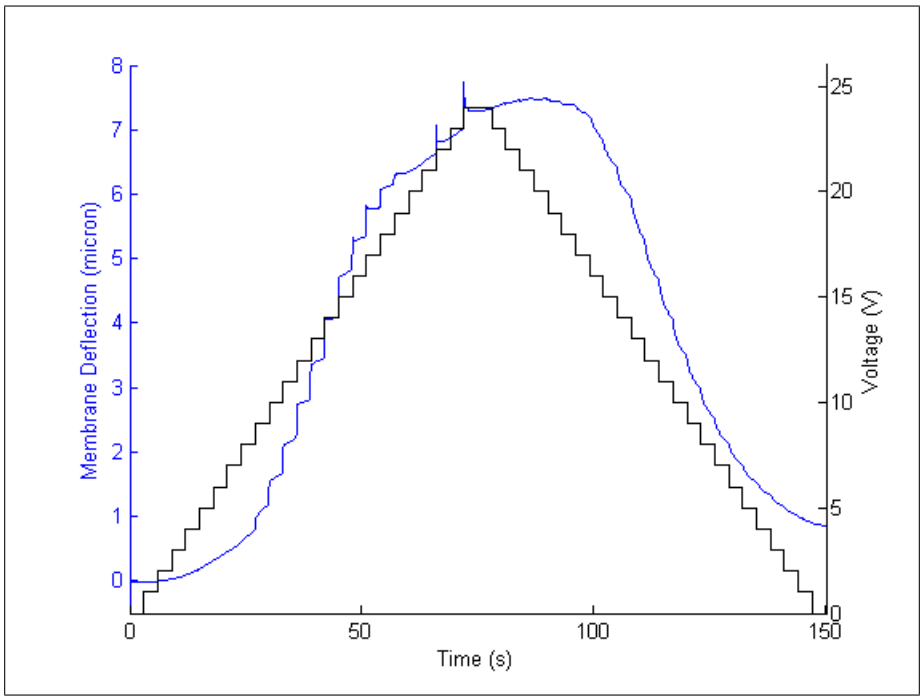

Figure H.15: Test O-SAS with $h = 94$ µm – $t_m = 39$ µm – $r_m = 439$ µm.

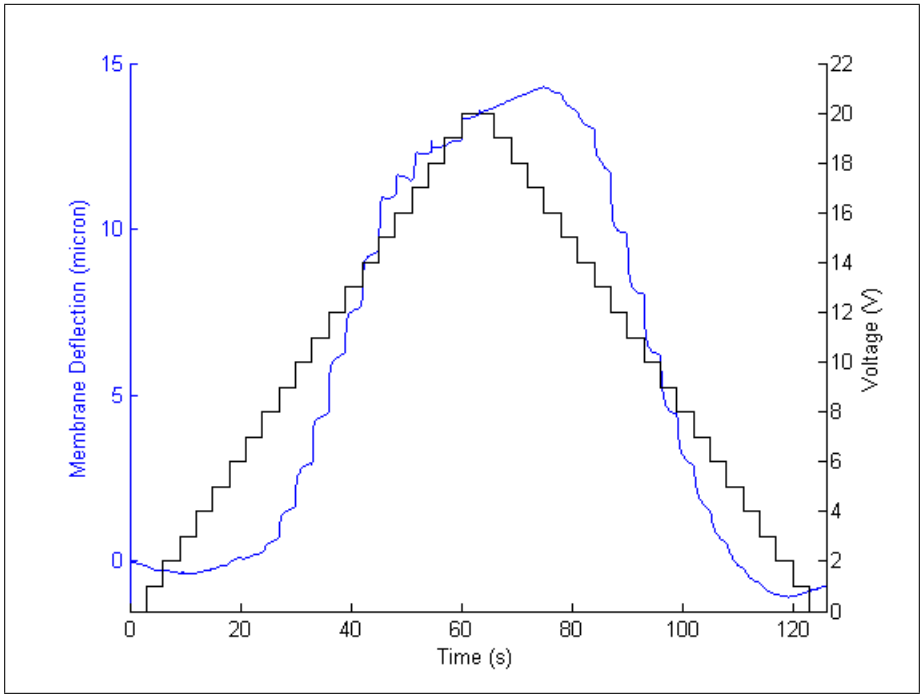

Figure H.16: Test P-SAS with $h = 111$ µm – $t_m = 40$ µm – $r_m = 441$ µm.

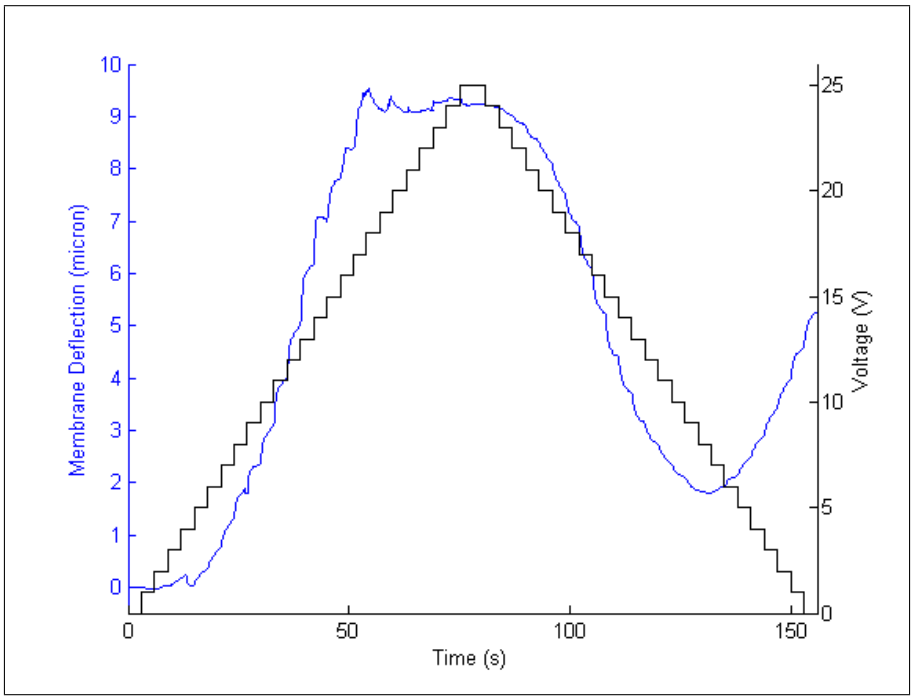

Figure H.17: Test Q-SAS with $h = 96$ µm – $t_m = 50$ µm – $r_m = 510$ µm.

Bibliography

[1] Carl Knospe and Christina Barth. Actuation of elastomeric micro devices via capillary forces. In Dan Zhang, editor, *Advanced Mechatronics and MEMS Devices - II*. Springer.

[2] Stephen R Quake and Axel Scherer. From micro-to nanofabrication with soft materials. *Science*, 290(5496):1536–1540, 2000.

[3] Benoit Roman and José Bico. Elasto-capillarity: deforming an elastic structure with a liquid droplet. *Journal of Physics: Condensed Matter*, 22(49):493101, 2010.

[4] Dominik J Bell, TJ Lu, Norman A Fleck, and Simon M Spearing. Mems actuators and sensors: observations on their performance and selection for purpose. *Journal of Micromechanics and Microengineering*, 15(7):S153, 2005.

[5] Felix Beyeler, Adrian Neild, Stefano Oberti, Dominik J Bell, Yu Sun, Jrg Dual, and Bradley J Nelson. Monolithically fabricated microgripper with integrated force sensor for manipulating microobjects and biological cells aligned in an ultrasonic field. *Journal of microelectromechanical systems*, 16(1):7–15, 2007.

[6] Evgueni V Bordatchev, Marco Zeman, and George K Knopf. Electro-thermo-dynamic performance of a microgripping system. In *IEEE International Conference Mechatronics and Automation, 2005*, volume 4, pages 1848–1853. IEEE, 2005.

[7] Ernst Thielicke and Ernst Obermeier. Microactuators and their technologies. *Mechatronics*, 10(4):431–455, 2000.

[8] Amit V Desai, Joshua D Tice, Christopher A Apblett, and Paul JA Kenis. Design considerations for electrostatic microvalves with applications in poly (dimethylsiloxane)-based microfluidics. *Lab on a Chip*, 12(6):1078–1088, 2012.

[9] Joshua Tice. *Electrostatically Actuated Microvalves Fabricated with Soft-Lithographic Techniques for Integrated Microfluidics*. PhD thesis, University of Illinois at Urbana-Champaign, 2009.

[10] Gregory A Ten Eyck, Eric D Branson, Paul JA Kenis, Amit Desai, Ben Schudel, Richard C Givler, Josh Tice, Andrew Collord, Christopher Alan Apblett, and Adam W Cook. Electrostatic microvalves utilizing conductive nanoparticles for improved speed, lower power, and higher force actuation. Technical report, Sandia National Laboratories, 2009.

[11] Joshua D Tice, Thomas A Bassett, Amit V Desai, Christopher A Apblett, and Paul JA Kenis. A monolithic poly (dimethylsiloxane) electrostatic actuator for controlling integrated pneumatic microsystems. *Sensors and Actuators A: Physical*, 196:22–29, 2013.

[12] Joshua D Tice, John B Rosheck, Christopher D Hamlin, Christopher A Apblett, and Paul JA Kenis. Normally-closed electrostatic microvalve fabricated using exclusively soft-lithographic techniques and operated with portable electronics. *Journal of microelectromechanical systems*, 22(6):1251–1253, 2013.

[13] Joshua D Tice, Amit V Desai, Thomas A Bassett, Christopher A Apblett, and Paul JA Kenis. Control of pressure-driven components in integrated microfluidic devices using an on-chip electrostatic microvalve. *RSC Advances*, 4(93):51593–51602, 2014.

[14] Ender Yıldırım, Haluk Külah, and MA Sahir Arıkan. An electrostatically actuated parylene microvalve for lab-on-a-chip applications. In *2011 16th International Solid-State Sensors, Actuators and Microsystems Conference*, pages 250–253. IEEE, 2011.

[15] Qing Zhang, Nikola Pekas, and David Juncker. Design and fabrication of novel compliant electrostatically actuated microvalves. In *Advanced Materials Research*, volume 74, pages 179–182. Trans Tech Publ, 2009.

[16] Meng-Ping Chang and Michel M Maharbiz. Electrostatically-driven elastomer components for user-reconfigurable high density microfluidics. *Lab on a Chip*, 9(9):1274–1281, 2009.

[17] Yanju Wang, Wei-Yu Lin, Kan Liu, Rachel J Lin, Matthias Selke, Hartmuth C Kolb, Nangang Zhang, Xing-Zhong Zhao, Michael E Phelps, Clifton KF Shen, et al. An integrated microfluidic device for large-scale in situ click chemistry screening. *Lab on a Chip*, 9(16):2281–2285, 2009.

[18] Yoseph Bar-Cohen. Electroactive polymers for refreshable braille displays. *SPIE Newsroom*, 11, 2009.

[19] Woonggyu Jung, Suo Tang, Daniel T McCormic, Tiquiang Xie, Yeh-Chan Ahn, Jianping Su, Ivan V Tomov, Tatiana B Krasieva, Bruce J Tromberg, and Zhongping Chen. Miniaturized probe based on a microelectromechanical system mirror for multiphoton microscopy. *Optics letters*, 33(12):1324–1326, 2008.

[20] JF Domke, CH Rhee, Z Liu, TD Wang, and KR Oldham. Amplifying transmission and compact suspension for a low-profile, large-displacement piezoelectric actuator. *Journal of Micromechanics and Microengineering*, 21(6):067004, 2011.

[21] Rosamund Daw and Joshua Finkelstein. Lab on a chip. *Nature*, 442(7101):367–367, 2006.

[22] Martina Hitzbleck and Emmanuel Delamarche. Reagents in microfluidics: an 'in'and 'out'challenge. *Chemical Society Reviews*, 42(21):8494–8516, 2013.

[23] T. Thorsen A. Scherer M. A. Unger, H. P. Chou and S. R. Quake. Monolithic microfabricated valves and pumps by multilayer soft lithography. *Science*, 288:113–116, 2000.

[24] Kwang W Oh and Chong H Ahn. A review of microvalves. *Journal of micromechanics and microengineering*, 16(5):R13, 2006.

[25] Daniel J Laser and Juan G Santiago. A review of micropumps. *Journal of micromechanics and microengineering*, 14(6):R35, 2004.

[26] Roger Angel, Rich Dekany, Bob Fugate, Ed Kibblewhite, Claire Max, Jerry Nelson, Scot Olivier, Andreas Quirrenbach, Mike Shao, and Laird Thompson. A roadmap for the development of astronomical adaptive optics, 2000.

[27] Bruce Macintosh, James Graham, Ben Oppenheimer, Lisa Poyneer, Anand Sivaramakrishnan, and Jean-Pierre Veran. Mems-based extreme adaptive optics for planet detection. In *MOEMS-MEMS 2006 Micro and Nanofabrication*, pages 611308–611308. International Society for Optics and Photonics, 2006.

[28] T Bifano, S Cornelissen, and P Bierden. Mems deformable mirrors in astronomical adaptive optics. In *1st AO4ELT conference-Adaptive Optics for Extremely Large Telescopes*, page 06003. EDP Sciences, 2010.

[29] Xingtao Wu, Hong Li, Li Yao, Haijiang Ou, and Chaoyang Pang. Large stroke actuators and mirror devices for ocular adaptive optics. In *SPIE MOEMS-MEMS*, pages 825308–825308. International Society for Optics and Photonics, 2012.

[30] Bautista R Fernández, Mohamed Amine Bouchti, and Joel Kubby. High-stroke, high-order mems deformable mirrors. *Journal of Micro/Nanolithography, MEMS, and MOEMS*, 12(3):033012–033012, 2013.

[31] Seyed Ali Nezamoddini. *Design, Microfabrication and Characterization of Capillary Force Actuators*. PhD thesis, University of Virginia, 2008.

[32] Carl R Knospe. Capillary force actuation: a mechatronic perspective. In *Control Technologies for Emerging Micro and Nanoscale Systems*, pages 201–218. Springer, 2011.

[33] Carl R Knospe and Hossein Haj-Hariri. Capillary force actuators: Modeling, dynamics, and equilibria. *Mechatronics*, 22(3):251–256, 2012.

[34] Huihui Wang, John T Gaskins, Carl R Knospe, and Michael L Reed. The capillary force actuator: Design, fabrication and characterization. In *Micro Electro Mechanical Systems (MEMS), 2012 IEEE 25th International Conference on*, pages 1185–1188. IEEE, 2012.

[35] Huihui Wang. *Design, Microfabrication and Characterization of Capillary Force Actuators*. PhD thesis, University of Virginia, 2012.

[36] Ronald F Probstein. *Physicochemical hydrodynamics: an introduction*. John Wiley & Sons, 2005.

[37] Gabriel Lippmann. *Relations entre les phénomènes électriques et capillaires*. PhD thesis, Gauthier-Villars, 1875.

[38] Frieder Mugele and Jean-Christophe Baret. Electrowetting: from basics to applications. *Journal of Physics: Condensed Matter*, 17(28):R705, 2005.

[39] X Hu, M Mibus, CR Knospe, G Zangari, and ML Reed. Impedance spectroscopy and electrical modeling of electrowetting on dielectric devices. *Journal of Micromechanics and Microengineering*, 25(4):045020, 2015.

[40] Stéphanie Chevalliot, Stein Kuiper, and Jason Heikenfeld. Experimental validation of the invariance of electrowetting contact angle saturation. *Journal of Adhesion Science and Technology*, 26(12-17):1909–1930, 2012.

[41] Frieder Mugele. Fundamental challenges in electrowetting: from equilibrium shapes to contact angle saturation and drop dynamics. *Soft Matter*, 5(18):3377–3384, 2009.

[42] F Mugele and J Buehrle. Equilibrium drop surface profiles in electric fields. *Journal of Physics: Condensed Matter*, 19(37):375112, 2007.

[43] HJJ Verheijen and MWJ Prins. Reversible electrowetting and trapping of charge: model and experiments. *Langmuir*, 15(20):6616–6620, 1999.

[44] Magali Vallet, Marcel Vallade, and Bruno Berge. Limiting phenomena for the spreading of water on polymer films by electrowetting. *The European Physical Journal B-Condensed Matter and Complex Systems*, 11(4):583–591, 1999.

[45] Jun Zeng and Tom Korsmeyer. Principles of droplet electrohydrodynamics for lab-on-a-chip. *Lab on a Chip*, 4(4):265–277, 2004.

[46] JR Melcher and GI Taylor. Electrohydrodynamics: a review of the role of interfacial shear stresses. *Annual Review of Fluid Mechanics*, 1(1):111–146, 1969.

[47] Junghoon Lee, Hyejin Moon, Jesse Fowler, Thomas Schoellhammer, and Chang-Jin Kim. Electrowetting and electrowetting-on-dielectric for microscale liquid handling. *Sensors and Actuators A: Physical*, 95(2):259–268, 2002.

[48] Richard B Fair. Digital microfluidics: is a true lab-on-a-chip possible? *Microfluidics and Nanofluidics*, 3(3):245–281, 2007.

[49] Sung Kwon Cho, Hyejin Moon, and Chang-Jin Kim. Creating, transporting, cutting, and merging liquid droplets by electrowetting-based actuation for digital microfluidic circuits. *Journal of microelectromechanical systems*, 12(1):70–80, 2003.

[50] Weiwei Cui, Menglun Zhang, Daihua Zhang, Wei Pang, and Hao Zhang. Island-ground single-plate electro-wetting on dielectric device for digital microfluidic systems. *Applied Physics Letters*, 105(1):013509, 2014.

[51] Menglun Zhang, Weiwei Cui, Xuejiao Chen, Chao Wang, Wei Pang, Xuexin Duan, Daihua Zhang, and Hao Zhang. Monolithic integrated system with an electrowetting-on-dielectric actuator and a film-bulk-acoustic-resonator sensor. *Journal of Micromechanics and Microengineering*, 25(2):025002, 2015.

[52] Bnmo Berge. Liquid lens technology: principle of electrowetting based lenses and applications to imaging. In *18th IEEE International Conference on Micro Electro Mechanical Systems, 2005. MEMS 2005.*, pages 227–230. IEEE, 2005.

[53] G Beni and S Hackwood. Electro-wetting displays. *Applied Physics Letters*, 38(4):207–209, 1981.

[54] J Heikenfeld, K Zhou, E Kreit, B Raj, S Yang, B Sun, A Milarcik, L Clapp, and R Schwartz. Electrofluidic displays using young–laplace transposition of brilliant pigment dispersions. *Nature Photonics*, 3(5):292–296, 2009.

[55] H You and AJ Steckl. Three-color electrowetting display device for electronic paper. *Applied physics letters*, 97(2):023514, 2010.

[56] A Schultz, J Heikenfeld, HS Kang, and W Cheng. 1000: 1 contrast ratio transmissive electrowetting displays. *Journal of Display Technology*, 7(11):583–585, 2011.

[57] Atsushi Takei, Kiyoshi Matsumoto, and Isao Shomoyama. Capillary motor driven by electrowetting. *Lab on a Chip*, 10(14):1781–1786, 2010.

[58] Prosenjit Sen and Chang-Jin Kim. A fast liquid-metal droplet microswitch using ewod-driven contact-line sliding. *Journal of Microelectromechanical Systems*, 18(1):174–185, 2009.

[59] Hong Ren, Richard B Fair, and Micheal G Pollack. Automated on-chip droplet dispensing with volume control by electro-wetting actuation and capacitance metering. *Sensors and Actuators B: Chemical*, 98(2):319–327, 2004.

[60] Ping An, Jing Chen, and Yilong Hao. Modeling and simulation of a novel vertical actuator based on electrowetting on dielectric. *Acta Mechanica Sinica*, 25(5):669–675, 2009.

[61] Sami Hage-Ali, Nicolas Tiercelin, Florian Lapierre, Yovan Orlic, Maxime Harnois, Vincent Thomy, Vladimir Preobrazhensky, Philippe Pernod, and Philippe Coquet. An ewod driven millimeter-wave phase shifter using a movable ultrasoft metalized pdms ground plane. In *2011 16th International Solid-State Sensors, Actuators and Microsystems Conference*, 2011.

[62] William P Eaton, Fernando Bitsie, James H Smith, and David W Plummer. A new analytical solution for diaphragm deflection and its application to a surface-micromachined pressure sensor. In *Technical Proceedings of the International Conference on Modeling and Simulation*, pages 640–643, 1999.

[63] S_ Timoshenko. Theory of plates and shells,(1940). *M cGraw-Hill*.

[64] Miao Liu, Jianren Sun, Ying Sun, Christopher Bock, and Quanfang Chen. Thickness-dependent mechanical properties of polydimethylsiloxane membranes. *Journal of micromechanics and microengineering*, 19(3):035028, 2009.

[65] Miao Liu, Jianren Sun, and Quanfang Chen. Influences of heating temperature on mechanical properties of polydimethylsiloxane. *Sensors and Actuators A: Physical*, 151(1):42–45, 2009.

[66] ID Johnston, DK McCluskey, CKL Tan, and MC Tracey. Mechanical characterization of bulk sylgard 184 for microfluidics and microengineering. *Journal of Micromechanics and Microengineering*, 24(3):035017, 2014.

[67] Hwa Seng Khoo, Kuo-Kang Liu, and Fan-Gang Tseng. Characterization of the mechanical properties of microscale elastomeric membranes. *Measurement science and technology*, 16(3):653, 2005.

[68] Tae Kyung Kim, Jeong Koo Kim, and Ok Chan Jeong. Measurement of nonlinear mechanical properties of pdms elastomer. *Microelectronic Engineering*, 88(8):1982–1985, 2011.

[69] M Mibus, C Jensen, X Hu, C Knospe, ML Reed, and G Zangari. Dielectric breakdown and failure of anodic aluminum oxide films for electrowetting systems. *Journal of Applied Physics*, 114(1):014901, 2013.

[70] Brandon L Thompson, Yiwen Ouyang, Gabriela RM Duarte, Emanuel Carrilho, Shannon T Krauss, and James P Landers. Inexpensive, rapid prototyping of microfluidic devices using overhead transparencies and a laser print, cut and laminate fabrication method. *Nature protocols*, 10(6):875–886, 2015.

[71] Jessamine Ng Lee, Cheolmin Park, and George M Whitesides. Solvent compatibility of poly (dimethylsiloxane)-based microfluidic devices. *Analytical chemistry*, 75(23):6544–6554, 2003.